

Multiphase Modelling of Engineered Tissue and Tumour Growth

Jacob Marcus Jepson

Thesis submitted to the University of Nottingham for the degree of Doctor of Philosophy

Abstract

In this thesis, we develop and analyse two multiphase, moving boundary models representing the evolution of biological tissue. The first model considers a description of engineered tissue growth, whereas the second describes solid tumour growth. The objective of this work is to characterise the effects of tissue mechanics, cell growth and nutrient limitation on various tissue structures. Additionally, we aim to derive novel mathematical results that can be applied to a wider class of mathematical models.

In the first part of this thesis, we derive a multiphase model representing the development of tissue *in vitro* in a porous scaffold. We consider a cell, extra-cellular liquid and a rigid scaffold phase, and adopt Darcy's law to relate the velocity of the cell and liquid phases with their respective pressures. We reduce the model to a nonlinear reaction—diffusion equation for the cell phase, coupled to a moving boundary condition for the tissue edge. Numerical simulations reveal that the reduced model admits various regimes for the evolution of the tissue. Employing travelling-wave and asymptotic analysis, we characterise these regimes in terms of parameters related to cellular growth and motion.

The second part of this thesis provides some novel numerical and asymptotic analyses of the multiphase tumour growth model developed in Byrne et al. (2002). We first employ the model of Byrne et al. (2002) to investigate the initial development of a suspension of nutrient-rich in vitro tumour cells. Numerical simulations indicate that both travelling-wave and patterned solutions can be obtained, the latter corresponding to multiple regions of high cell density separated by regions of low cell density. A stability analysis of these travelling-wave solutions provides us with criteria for the occurrence of patterned solutions. After this, the model of Byrne et al. (2002) is revisited, and is employed to investigate the effects of nutrient limitation and tissue mechanics on a solid tumour in the avascular stage of growth.

Acknowledgements

First and foremost, my sincerest gratitude goes to John Billingham, Reuben O'Dea and Nabil Fadai for their advice, continuous support and patience over the duration of this work. John, this work owes much of its success to your dedication to teaching, wisdom and expertise in asymptotic analysis! Reuben, your mathematical-meticulousness, humour and unparalleled aptitude for Scientific communication will never cease to amaze me. Nabil, your professionalism, tutelage and guidance throughout my studies have allowed me to strive toward my potential and encouraged me to pursue an academic career. In addition to my supervisors, I would like to thank Professor John King for inspiration for the work in chapter one and for guidance in its development. I would also like to acknowledge funding provided by the Engineering and Physical Sciences Research Council.

I am also extremely grateful to my friends and family, who have shown unwavering support and encouragement throughout the duration of this work. Specifically, I owe an immense debt of gratitude to my remarkable mother – your endless belief in my abilities, and teachings on the importance of pursuing your passions, have paved the way for this journey. I'd also like to express a deep appreciation to my father and stepmother, Ruth, for their unfaltering and loving guidance, as well as a roof over my head for the last three years. Special thanks go to Chris, for making everyday feel like summer.

List of Publications

- 1. Travelling-wave and asymptotic analysis of a multiphase moving boundary model for engineered tissue growth. Bulletin of Mathematical Biology, 84:87 (2022). This publication contains work presented in Chapter 2.
- 2. Pattern formation and travelling waves in a multiphase moving boundary model of tumour growth. Biorxiv. DOI: https://doi.org/10.1101/2022.11.23.517688 (2022). This pre-print contains work presented in Chapter 3 and is currently under author-revision for publication in Mathematical Medicine and Biology: A journal of the IMA.

Contents

A	bstra	ct		i
A	cknowledgements			
Li	st of	Public	cations	iii
1	\mathbf{Intr}	oducti	ion	1
	1.1	An ove	erview of tissue engineering	1
		1.1.1	In vitro tissue engineering	4
	1.2	An ove	erview of tumour growth	6
		1.2.1	The in vivo tumour growth process	7
		1.2.2	in vitro tumour modelling	9
	1.3	Mathe	ematical background of tissue growth models	10
		1.3.1	Microscopic modelling	10
		1.3.2	Ordinary differential equation modelling	11
		1.3.3	Continuum partial differential equation modelling	12
		1.3.4	Multiphase modelling	13
	1 4	Averag	ged mass transfer equations for two-phase flow	15

<u>CONTENTS</u> vi

		1.4.1	Definitions and identities	6
		1.4.2	Averaged conservation of mass equation	8
	1.5	Thesis	objectives and structure	8
2		_	-Wave and Asymptotic Analysis of a Multiphase Moving model of Engineered Tissue Growth 22	1
	2.1	Introd	uction	1
	2.2	Model	development	2
		2.2.1	Governing equations	3
		2.2.2	Initial and boundary conditions	4
		2.2.3	Model reduction	4
		2.2.4	Constitutive assumptions	5
		2.2.5	Non-dimensionalisation	6
		2.2.6	Linear stability analysis and parameter values	7
	2.3	Numer	rical results	8
		2.3.1	Numerical methods	8
		2.3.2	Results	9
	2.4	Travel	ling-wave analysis for $\kappa > 0$	0
		2.4.1	Formulation	0
		2.4.2	Shooting method	2
		2.4.3	Results	3
	2.5	Asymp	ptotic analysis for $ \kappa \ll 1 \ldots 3$	4

<u>CONTENTS</u> vii

		2.5.1	Implicit solutions for $N(x, T)$ and $L(T)$	7
		2.5.2	Large-time behaviour of $N(x, T)$ and $L(T)$	8
		2.5.3	Large-time behaviour of $n(x, t)$ and $L(t)$	8
		2.5.4	Convergence of asymptotic solutions	0
	2.6	Conclu	nsions	2
3			ormation and Travelling Waves in a Multiphase Moving Model of Tumour Growth 46	6
	3.1	Introd	uction	6
	3.2	Model	development	8
		3.2.1	Governing equations	8
		3.2.2	Constitutive assumptions	9
		3.2.3	Initial and boundary conditions	1
		3.2.4	Model reduction	1
		3.2.5	Non-dimensionalisation	2
	3.3	Numer	rical results	3
		3.3.1	Numerical methods	3
		3.3.2	Results	5
	3.4	Travel	ling-wave solutions and stability analysis	8
		3.4.1	Formulation	8
		3.4.2	Determining the stability of travelling waves	9

<u>CONTENTS</u> viii

		3.4.3	Numerical methods for the travelling-wave ODEs, equations	
			(3.44)-(3.46)	60
		3.4.4	Numerical methods for the eigenvalue problem, equations (3.51)—	-
			$(3.53) \ldots \ldots \ldots \ldots \ldots \ldots \ldots$	63
		3.4.5	Results	68
	3.5	The st	sability of a spatially-uniform steady state	70
	3.6	Qualit	ative analysis of pattern formation	73
		3.6.1	Mathematical formulation	73
		3.6.2	Results	76
	3.7	A pai	rameter case study: the $\kappa \to 0$ limit	78
		3.7.1	Formulation of the leading order problem for $t = \mathcal{O}(1)$	79
		3.7.2	Results	81
	3.8	Conclu	asion	84
4	A n	nultiph	ase model for nutrient limited tumour growth	88
	4.1	Introd	uction	88
	4.2	Model	development	89
		4.2.1	Constitutive assumptions	91
		4.2.2	Non-dimensionalisation	92
	4.3	Nume	rical results	93
		4.3.1	Numerical methods	93
		4.3.2	Travelling-wave, steady-state and extinction-type solutions $\ .$.	99

	4.4	Travel	lling-wave analysis	. 101
		4.4.1	Formulation	. 102
		4.4.2	Numerical Methods	. 103
		4.4.3	Numerical results	. 105
		4.4.4	Asymptotic analysis for $\beta \ll 1$. 108
		4.4.5	Asymptotic analysis for $\beta \gg 1$. 111
	4.5	Criter	ia for extinction-type solutions	. 115
		4.5.1	Asymptotic analysis of the steady-state ODEs as $L_\infty \to 0$. 116
		4.5.2	Results	. 119
	4.6	Concl	usions	. 121
5	Cor	nclusio	ns and Future Work	124
	5.1	Thesis	s Overview	. 124
	5.2	Summ	nary of Results	. 125
		5.2.1	Chapter 2	. 125
		5.2.2	Chapter 3	. 126
		5.2.3	Chapter 4	. 128
		5.2.4	Future Work	. 129
Bi	ihlios	ranhv		131

List of Figures

1.1	Scan of a poly-l-lactic acid scaffold taken from Ma (2004)	•
1.2	Cross-section of a stained tumour spheroid from Monazzam et al. (2005).	{
2.1	Numerical solutions of the system of PDEs from (2.18)–(2.20). The green lines in (a,c,e) represent the initial conditions $n_0(x)$ from (2.23), whereas the black lines represent n for different values of t . The black arrows point in the direction of increasing time. The dashed red line in (d) is given by $\ln(t)/\sqrt{2}-1$ and highlights the logarithmic growth of L at large time. Parameter values: $L_0=\mu=\eta=1,\omega=0.03$ and $s=0.2$	31
2.2	Numerical solutions for the wave speeds $c(\kappa)$ and $c(s)$. The solid black and dashed green lines represent approximations sought by numerically solving (2.37) and (2.38) using a shooting method and the system from (2.18)–(2.20), respectively. Parameter values for (a): $\mu = \eta = L_0 = 1$, $s = 0.2$ and $\omega = 0.03$. Parameter values for (b): $\mu = \eta = L_0 = 1$, $r_a/r_m = 0.2$ and $\omega = 0.03$	34
2.3	Numerical solutions for the wave speeds $c(\mu, \eta)$ for $\kappa = 0.3$ and $\kappa = 0.7$ sought by numerically solving (2.37) and (2.38) using a shooting method. $s = 0.2$ was used for both sub-figures. We note that the colour axes are different in each sub-figure.	3!

LIST OF FIGURES xii

2.4	Numerical solution (solid black line) of the PDE system from (2.18) – (2.20) vs	
	asymptotic solution (dashed green line) from (2.72) and (2.70) for n (a) and L	
	(b) for $\kappa=0.001$. Solutions for n are presented on $t\in[6000,10000]$ at intervals of	
	1000. Initial conditions for the numerical simulations were chosen to satisfy (2.53)	
	and (2.54). Parameter values: $\mu=\eta=1,s=0.2,A_0=0.05$ and $B_0=0.01$	40
2.5	Numerical solution (solid black line) of the PDE system from (2.18) – (2.20) vs	
	asymptotic solution (dashed green line) from (2.73) and (2.70) for n (a) and L	
	(b) for $\kappa = -0.001$. Solutions for n are presented on $t \in [8000, 10000]$ at intervals	
	of 500. Initial conditions for the numerical simulations were chosen to satisfy (2.53)	
	and (2.54). Parameter values: $\mu=\eta=1,s=0.2,A_0=0.05$ and $B_0=0.01$	41
2.6	Numerical solution (solid black line) of the PDE system from (2.51) and (2.44)	
	vs asymptotic solution (dashed red line) from (2.79) and (2.80) for n and L for	
	different initial conditions $N(x, 0)$ and $L_0 = 1$. Solutions for n are presented on	
	$T \in [6000,10000]$ at intervals of 1000. The values of m in (a) and (b) are selected	
	to provide a good agreement between the asymptotic and numerical solutions. $$.	42
3.1	Numerical solutions of the PDE system from (3.20) – (3.23) for three values of	
	ϕ . The black lines in (a, c, e) represent $n(x, t)$ at indicated fixed times, while	
	the colour maps in (b, d, f) represent $n(x, t)$ across a temporal interval. The pink	
	arrows point in the direction of increasing time. Parameter values: $r_m = 0.3, r_a =$	
	0.2, $\kappa = 100$ and $\phi = 0.2$ (a, b), $\phi = 0.5$ (c, d) and $\phi = 0.85$ (e, f)	57
3.2	The discrete spectrum obtained from (3.76) illustrating the eigenvalues λ with	
	the largest real part for $\phi=0.7$ (a), $\phi=0.8$ (b) and $\phi=0.9$ (c). Parameter	
	values: $r_m = 0.4$, $r_a = 0.2$, $K = 1500$ and $Z = 15$	67
3.3	An illustration of the convergence of the three eigenvalues obtained from (3.76)	
	with the largest real-part for $K \in [400, 2000]$. Parameter values: $r_m = 0.4, r_a =$	
	$0.2,\phi=0.9$ and $Z=15.$	68

LIST OF FIGURES xiii

3.4	An analysis of travelling-wave solutions and their stability. In (a), the black solid	
	line is the curve $\Lambda=0$ obtained numerically from (3.51)–(3.53). The black dashed	
	line is the curve $c=0$. The colour map shows c , obtained numerically from (3.44)—	
	(3.46). Parameter values for (a) are $0 < \phi < 1, 0.2 < r_m \le 1$ and $r_a = 0.2$.	
	In (b, c), we plot $n(x, t)$ from the PDE system (3.20)– (3.23) for $\phi = 0.87$ (pink	
	dot) and $\phi=0.91$ (green dot) when $t=0,3,6,9.$ Parameter values for (b,c) are	
	$r_m = 0.6, r_a = 0.2, \kappa = 50.$ For both (b, c), we use $n_i(x) = N(x) + 0.05\sin(15\pi x)$,	
	where $N(x)$ is the travelling-wave solution when $t=0.$	69
3.5	A stability analysis of the spatially-uniform steady state $(n, v_n) = (\alpha, 0)$. In (a),	
	the solid black line is the function $\rho(\gamma)$ from (3.86) for $r_m=0.3,r_a=0.2$ and	
	$\phi = 0.7$, whilst the dashed black line is $\rho(\gamma)$ for $r_m = 0.5$, $r_a = 0.2$ and $\phi = 0.7$.	
	In (b), the solid black line is the curve $\Lambda=0$ obtained numerically from (3.51)–	
	(3.53), whilst the dashed pink line in is the curve $\rho_{\infty} = 0$, both with $r_a = 0.2$.	
		72
3.6	A quantification of patterned solution features. In (a), we present a numerical	
	solution $n(x, t)$ from the PDE system (3.20)– (3.23) at $t = 40$ for $r_m = 0.4$, $r_a =$	
	$0.2, \phi = 0.75, \kappa = 25 \text{ and } n_i(x) = \alpha + 0.05\sin(15\pi x).$ The green line segments	
	between the green crosses indicate the elements in $X(t)$ from (3.89). In (b), we	
	present the metrics $\beta(t)$ and $\omega(t)$ for $\zeta=0.03$ and $\zeta=0.09$. We use $r_m=0.05$	
	0.3, $r_a = 0.2$, $\phi = 0.85$, $\kappa = 100$ and $n_i(x)$ defined as in (a)	74
3.7	The variation of B,M and W from (3.91) with $\kappa,$ computed from numerical	
	solutions of the PDE system (3.20) – (3.23) , together with exemplar numerical	
	solutions of $n(x, t)$ at $\kappa = 5$ (orange dot), $\kappa = 200$ (pink dot) and $\kappa = 500$ (green	
	dot). Remaining parameter values: $r_m=0.3,r_a=0.2,\phi=0.65,\nu=15.$	75
3.8	The variation of B,M and W from (3.91) with $\phi,$ computed from numerical	
	solutions of the PDE system (3.20) – (3.23) , together with exemplar numerical	
	solutions of $n(x, t)$ at $\phi = 0.6$ (orange dot), $\phi = 0.75$ (pink dot) and $\phi = 0.9$	
	(green dot). Remaining parameter values: $r_m=0.3,r_a=0.2,\kappa=25,\nu=15.$	76

<u>LIST OF FIGURES</u> xiv

3.9	The variation of B,M and W from (3.91) with $\nu,$ computed from numerical	
	solutions of the PDE system (3.20) – (3.23) , together with exemplar numerical	
	solutions of $n(x, t)$ at $\nu = 15$ (orange dot), $\nu = 30$ (pink dot) and $\nu = 60$ (green	
	dot). Remaining parameter values: $r_m=0.3,r_a=0.2,\phi=0.65$ and $\kappa=25.$	77
3.10	Numerical solution (solid black line) of the PDE system from (3.20) – (3.23) when	
	$\kappa=0.001$ against asymptotic solution (dashed green line) obtained from (3.97) for	
	$n_0=0.2$ and two different values of ϕ . Parameter values: $r_m=0.8$ and $r_a=0.3$.	82
3.11	The quantity $n_a(t)$ (solid black line) obtained from numerical solution of the	
	PDE system from (3.20)–(3.23) when $\kappa=0.001$ against $n_a(t)$ asymptotic solution	
	(dashed green line) obtained from (3.97) for $n_0=0.2$ and four different values of	
	ϕ . Parameter values: $r_m = 0.8$ and $r_a = 0.3$	83
4.1	The function ξ from (4.27) for $\theta=2,4,6,8$ and $K=1000.$	94
4.2	Numerical solutions of the PDE system from (4.12)–(4.17) for $\phi=0.3$. The	
	black lines represent variable solutions at fixed times $t=0,10,\ldots,120$ and	
	the arrows point in the direction of increasing time. The dashed line in (b)	
	represents $v_n(L, t)$ and highlights the linear growth of $L(t)$ observed in (d). The	
	functions $\Gamma(n, c)$ and $\Sigma(n)$ are plotted in (e) and (f), respectively. Parameter	
	values: $r_m = 1, r_a = 0.3, \kappa = 1, \rho = 1, \sigma = 2 \text{ and } n_0 = 0.6. \dots \dots \dots \dots$	98
4.3	Numerical solutions of the PDE system from (4.12)–(4.17) for $\phi=0.55$. The black	
	lines represent variable solutions at fixed times $t=0,10,\ldots,60$ and the arrows	
	point in the direction of increasing time. The dashed lines in (a–c) represent the	
	variables n , v_n and c for $t = 300$, at which time $L(t)$ is approximately constant.	
	The functions $\Gamma(n, c)$ and $\Sigma(n)$ are plotted in (e) and (f), respectively. The inset	
	in (d) represents $L'(t)$ and highlights the steady-state nature of $L(t)$. Parameter	
	values: $r_m = 1, r_a = 0.3, \kappa = 1, \rho = 1, \sigma = 2 \text{ and } n_0 = 0.6. \dots \dots \dots \dots$	100

<u>LIST OF FIGURES</u> xv

4.4	Numerical solutions of the PDE system from (4.12)–(4.17) for $\phi = 0.8$. The black
	lines represent variable solutions at fixed times $t=0,2,\ldots,14$ and the arrows
	point in the direction of increasing time. The dashed lines in (a-c) represent
	the variables n , v_n and c for $t = 100$, at which time $L(t)$ is approximately zero.
	The inset in (d) represents $\log(L)$ and highlights the exponential decay of $L(t)$.
	Parameter values: $r_m = 1, r_a = 0.3, \kappa = 1, \rho = 1, \sigma = 2 \text{ and } n_0 = 0.6.$ 102
4.5	Numerical solutions for $n(z), v(z)$ and $c(z)$ from the travelling-wave ODE sys-
	tem (4.46)–(4.49) for various values of ϕ spaced uniformly over the interval
	$\phi = [0.1, 0.5]$. The arrows point in the increasing direction of ϕ . The regions
	(i) and (ii) in (a,b) indicate where $n(z)$ increase and decrease with ϕ , respec-
	tively. Parameter values: $r_m=1,\ r_a=0.1,\ \sigma=2,\ \beta=5$ and $M=20.$ 100
4.6	Numerical solutions of $n(z),v(z)$ and $c(z)$ from the travelling-wave ODE system
	(4.46)–(4.49) for various values of β spaced uniformly over the interval $\beta = [1, 5]$,
	respectively. The arrows point in the increasing direction of β . Parameter values:
	$r_m = 1, \ r_a = 0.1, \ \sigma = 2, \ \phi = 0.1 \text{ and } M = 20. \dots \dots$
4.7	Numerical solution of the wave speed $U(\beta, \phi)$ (a) and the quantity $Y(\beta, \phi)$ (b)
	from (4.62) computed from numerical solutions of $n(z)$. Parameter values: $\phi =$
	0.1, $r_a = 0.1$, $\sigma = 2$ and $M = 20$
4.8	Numerical solution (solid black line) of the PDE system from (4.12) – (4.17) and
	asymptotic solution (dashed green line) from (4.72) and (4.73) for (a) n and (b)
	c for $\beta = 0.001$. Parameter values: $r_m = 1, r_a = 0.2, \sigma = 1.5, \phi = 0.2$ and $n_0 = 0.6.112$
4.9	Numerical solution of the PDE system from (4.12) – (4.17) and asymptotic solu-
	tions from (4.76)–(4.80) for $\beta=50$. Parameter values: $r_m=2,r_a=0.5,\sigma=$
	1.1, $\phi = 0.4$, $n_0 = 0.6$ and $M = -50$

- - (a) correspond to the coordinates $(r_m, \phi) = (0.4, 0.51)$, $(r_m, \phi) = (1, 0.81)$ and $(r_m, \phi) = (1.7, 0.89)$, respectively. In (b), the green, orange and pink lines represent $\log(L)$ obtained from the PDE system from (4.12)–(4.17), with parameter values corresponding to the respective coloured dots in (a). Parameter values:

Chapter 1

Introduction

Understanding the complex mechanisms that underpin tissue growth is fundamental to the development of regenerative medicine and treatment for diseases such as cancer. In this thesis, we develop and analyse two multiphase models representing the evolution of biological tissue. The first considers a description of engineered tissue growth, whereas the second describes tumour growth. Before this, we provide an overview of engineered tissue and tumour growth and highlight various mathematical models which have been used to investigate these processes. Additionally, we outline a derivation of the conservation of mass equations which are used throughout this work. We conclude this chapter by highlighting our key objectives and providing a framework for the remainder of this thesis.

1.1 An overview of tissue engineering

In vitro tissue engineering is a form of regenerative medicine which often involves seeding cells into a porous bio-engineered scaffold to allow for nutrient transport, structural support and a means for cell signalling activity (Chan and Leong, 2008a). Subject to the correct environment and growth factors, the cells will develop into a functional biological tissue (termed construct) that can be used to restore and regenerate damaged tissues. Employing contributions from an assortment of scientific fields, tissue engineering is considered an interdisciplinary practice that has the

potential to benefit a substantial proportion of the global population suffering from devastating soft tissue, bone and whole organ diseases (Dzobo et al., 2018). Whilst the field of tissue engineering is rich in both theoretical and experimental knowledge, numerous limitations including a lack of understanding regarding the processes by which cells assemble into tissues means that viable replacement constructs are only available in a minority of cases.

Tissue engineering, broadly speaking, consists of two main practices: in vitro (within the glass) and in vivo (within the living). In vitro tissue engineering, which is the biological focus in chapter two of this thesis, often involves cultivating a sample of healthy cells until a viable tissue construct is developed. These cells can be implanted into a porous tissue engineering scaffold (see figure 1.1) and cultured in a bio-reactor, which mimic the relevant in vivo environment and promote cell differentiation by providing a means for nutrient transport and chemical and physical stimuli (Plunkett and O'Brien, 2018). We will examine in vitro tissue engineering in more depth in subsection 1.1.1. On the other hand, in vivo tissue engineering often involves seeding a degradable scaffold with cells and then implanting it within the recipient in place of the damaged tissue. This procedure necessitates that the host colonise, vascularise, and integrate the implanted scaffold with the surrounding tissue. If the scaffold cannot be initially implanted in situ of the damaged tissue, it is implanted in some other location, where it is colonised by cells, harvested and re-implanted in situ. See McCullen et al. (2011) for examples of this process relating to musculo-skeletal tissue engineering.

The first successful generation of a skin substitute using tissue engineering techniques was produced in the 1970s, as a result of a partnership between the Massachusetts Institute of Technology and the Massachusetts general hospital Vacanti (2006). Approximately thirty years later, a group of surgeons replaced a patient's windpipe with one that was cultured from their own cells, becoming the first tissue engineered whole organ to be transplanted (Fletcher, 2008). More recently, the field of tissue engineering has enjoyed many other successes; for example, the generation,

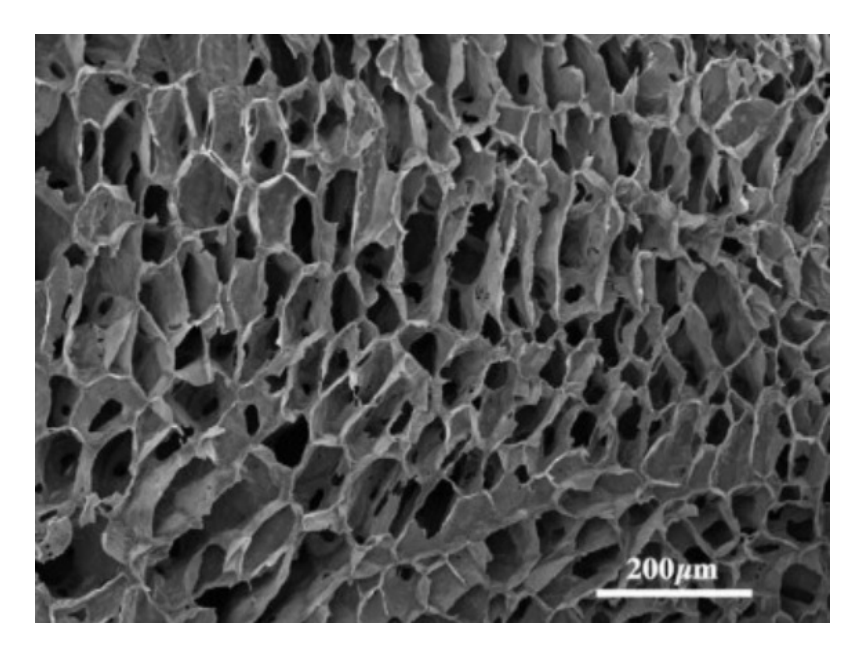


Figure 1.1: Scan of a poly-l-lactic acid scaffold taken from Ma (2004)

replacement and longevity of engineered bones and bronchial tubes derived from the recipients' cells (Sato et al., 2008; Petite et al., 2000; Schimming and Schmelzeisen, 2010). However, a shortage in the supply of donor tissue creates a demand on the field to make engineered tissue routinely clinically available (Levitt, 2015).

Tissue constructs cultured via tissue engineering techniques can also be used to improve concepts in pharmaceutical research such as experimental drug therapy (Jensen et al., 2018b). For instance, neural cells can be cultured *in vitro* to examine the efficacy of different drugs used to treat neurodegenerative diseases such as traumatic brain injury and Alzheimer's disease; see Jensen et al. (2018a) for a review. Tissue constructs can also be used to study human disease progression and monitor the way in which these tissues respond to medical treatment.

In vitro tissue engineering employs a wide range of methods to culture a small population of cells into a tissue construct. For example, multi-cellular spheroids, used as experimental models of tumours, are often cultured using scaffold-free methods, whereby cells are suspended in a nutrient rich fluid and self-assemble into spheroids. Cells can also be cultured within a porous bio-scaffold, which aims to replicate the *in vivo* environment by providing structural support for cell attachment and proliferation, for example (Chan and Leong, 2008b). To promote these

biological processes, porous bio-scaffolds must adhere to an array of essential attributes, some of which we now briefly outline, based on the reviews by Chan and Leong (2008b) and O'Brien (2011).

To encourage cell growth in a scaffold, its architecture should be porous and well-interconnected, allowing the transport of nutrient and waste, as well as cell signalling and migration. Furthermore, the scaffold porosity must be large enough to allow cell migration within the scaffold, but small enough both to promote optimal cell-scaffold attachment and to enable the scaffold to possess mechanical properties such as tensile strength. Without sufficient mechanical integrity, cell types which exert traction forces, such as muscle cells, can display deficient proliferation and morphological tendencies (Discher et al., 2005). The bio-materials used to fabricate the scaffold must also be compatible with cellular components. Especially in the case of *in vivo* tissue engineering, the scaffold must elicit a minimal immune response from the host to prevent, for example, an inflammatory response (O'Brien, 2011). In view of these arguments, it is not surprising that a range of scaffold pore sizes has been suggested which depend on cell type; for example, Murphy et al. (2010) indicates that a mean pore size of $325 \,\mu\text{m}$ is optimal for bone tissue engineering.

1.1.1 In vitro tissue engineering

We now provide a brief overview of how *in vitro* tissue engineering seeks to cultivate a small population of donor cells into a tissue construct.

The initial acquisition of donor cells required to cultivate a tissue construct can be made using a diverse range of techniques (Zakrzewski et al., 2019). In some cases, pertaining to stem cell acquisition for example, a donor must undergo surgery in which cells are harvested from bone marrow. This is an invasive and painful procedure and has led researchers to consider alternative sources. For example, stem cells can also be isolated from adipose tissue, which is a plentiful and readily available source, and the procedures involved in their acquisition are not associated with

patient discomfort (Rad et al., 2017). Another non-invasive method of obtaining stem cells is via the donor bloodstream. One limitation associated with donor cell acquisition occurs when attempting to acquire a sufficiently large and healthy population of cells to implant within a scaffold. This can be especially challenging if the tissue from which they are obtained is aged or diseased; for example, it is difficult to acquire cardiac cells from a patient who has recently suffered from a heart attack (Ikada, 2006). This limitation can be overcome by expanding a small population of healthy cells via a culture to an appropriate size for transplantation; however, this can be time-consuming and expensive (Ikada, 2006).

After this initial population of cells have been acquired, they are seeded into a porous bio-scaffold. There are numerous methods for accomplishing this, and we now briefly discuss the salient features of passive and dynamic seeding, based on the review in Villasante and Vunjak-Novakovic (2015). Passive seeding is a straightforward approach which involves the placement of cells onto the scaffold exterior, whereby gravitational force subsequently enables their penetration into the scaffold interior. One limitation of this approach arises when cells are unable to fully penetrate the scaffold, which can result in a non-uniform distribution of tissue; however, this can sometimes be overcome by coating the scaffold with a biological glue such as fibrin which enhances cell motility (Park and Woo, 2018). Dynamic seeding is a more intricate approach than static seeding. One type of dynamic seeding is rotational seeding, where a suspension of cells are implanted in the center of a scaffold which is then rotated, so that further cell penetration is achieved via centrifugal force. Although dynamic seeding via rotation can improve the cell distribution within a scaffold in comparison to passive seeding, it can have an adverse effect cell structure and can be time-consuming.

When an initial population of cells have been adequately distributed throughout a scaffold, a bioreactor can be used to provide them with chemical and mechanical regulatory signals required for cell differentiation, proliferation and other processes (Zhao et al., 2016). A commonly used bioreactor is the stirred-tank, within which

a seeded scaffold is suspended in a mixture that is stirred using mechanical blades. Fresh mixture containing bio-chemicals and growth factors is supplied at the top of the stirred-tank reactor, and spent nutrient and waste is filtered through the bottom. One limitation of these bioreactors arises when the fresh medium is not well-stirred throughout the tank. This can be resolved by increasing the speed at which the the mixture is stirred; however, this can generate excessive shear forces that can have an adverse effect on cell morphology and proliferation. Perfusion bioreactors are also frequently employed and involve continuously passing nutrient through a chamber containing a scaffold at its centre.

1.2 An overview of tumour growth

Cancer is a term used to describe a group of diseases occurring when abnormal cells divide uncontrollably, often spreading to other parts of the body. As the second leading cause of death worldwide, cancer has a significant impact on the health of individuals and their families. Cancer also has a significant financial impact on society and families, particularly in developing nations where access to cancer treatment and prevention is limited and expensive (Shah et al., 2019).

A tumour is characterised by an abnormal mass of tissue that develops when cells divide more frequently or die less frequently than they should (Patel, 2020). Benign tumours are non-invasive, remain local to the site at which they first developed and often asymptomatic. Although benign tumours are not typically life threatening, they may need to be surgically or cosmetically removed if they interfere with bodily functions or cause discomfort. Some examples of benign tumours include warts and lipomas, which are characterised by a soft fatty lump that can form between skin and muscle. Malignant (cancerous) tumours possess uncontrollably dividing cells. Unlike benign tumours, malignant tumours can rapidly grow and have the potential to spread throughout the body (Patel, 2020). Carcinomas, the most prevalent type of malignancies (McDaniel et al., 2020), account for approximately

85% of all diagnoses and results from the growth of mutated epithelial tissue cells, found on the outer lining of organs like the skin or kidneys. Sarcomas, on the other hand, are less common and develop from cells in connective tissue like muscle or tendons.

Medical intervention can often decrease the invasive potential of a malignant tumour or entirely eradicate it, whilst minimising damage to surrounding healthy tissue. In many cases, different types of treatment are used in conjunction to improve their overall effectiveness (Mokhtari et al., 2017). The most common treatment for solid tumours is surgery, whose aim is to remove a large volume of tumour. Radiotherapy is another widely used treatment option, involving the localised use of high-energy radiation to destroy or slow the growth of cancer cells. Radiation can either be directed at a tumour via external beams, or by internal radiation which involves placing a radioactive source inside the body near the tumour (Wang et al., 2019). Another treatment is chemotherapy, whereby drugs provided orally or intravenously kill cancer cells. Unlike surgery or radiotherapy, chemotherapy is systemic and travels throughout the body before localising toward cancerous cells. This can elicit a number of prolonged side effects including hair loss, nausea and a weakened immune system. As well as intervention, prevention also plays a pivotal part of cancer management in a population.

1.2.1 The *in vivo* tumour growth process

The formation of a solid, cancerous tumour is a complex and multi-step process, and we now highlight the salient features of its development.

The initiation of tumour development describes the stage whereby the DNA of cells are irreversibly damaged or mutated. This can arise by exposure to external factors such as radiation, bacterial infection and carcinogens, or naturally, via an incorrect DNA replication or hereditary predispositions (Teimouri et al., 2019). These abnormalities can affect genes responsible for regulating processes such as cell

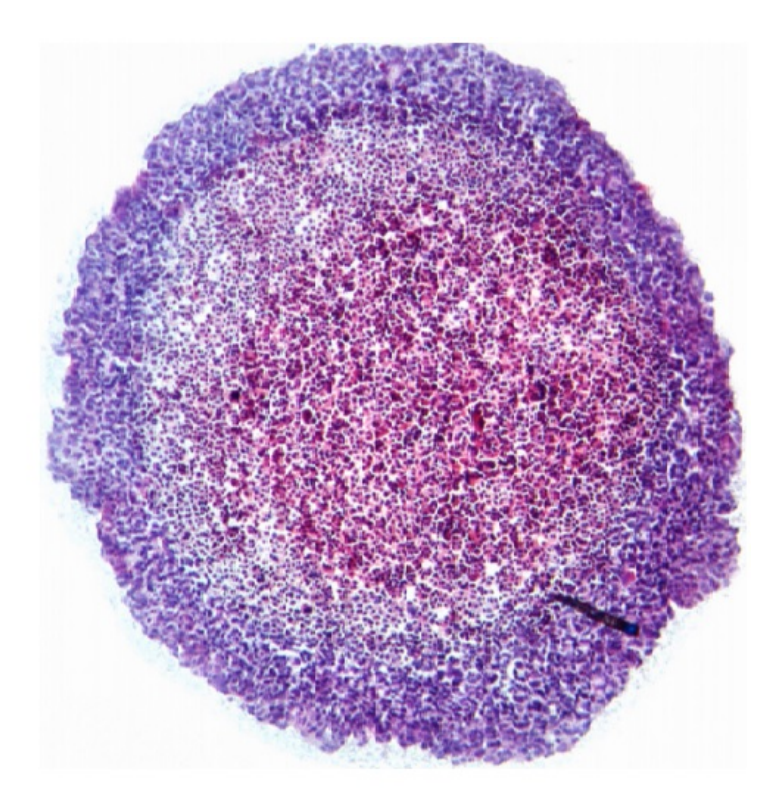


Figure 1.2: Cross-section of a stained tumour spheroid from Monazzam et al. (2005).

division and motility, resulting in behaviours such as sustained proliferation or a resistance to apoptosis (programmed cell death). Consequently, damaged or mutated cells can initiate the formation of a solid tumour mass.

In the earliest stages of growth, the tumour is sufficiently small that all cells are adequately nourished by nutrient obtained from the surrounding tissue by diffusion. As the tumour grows, a limited amount of nutrient enters the core due to its consumption by cells in the tumour rim. As such, the tumour interior contains dormant cells which are in a reversible state of growth arrest (Ruksha, 2019), surrounded by a layer of proliferating cells. A prolonged absence of nutrients from the core elicits cell death and consequently a necrotic core, this surrounded by a layer of dormant and then proliferating cells. Tumours in this stage of development are classified as avascular and their growth saturates toward a size not typically exceeding 2 mm³ (Folkman, 1990). In figure 1.2, a cross-section of a tumour spheroid is provided, which highlights the three-layer structure of an avascular tumour.

Although avascular tumours can remain benign, complications can arise when

their malnourished cells release agents stimulating the development of blood vessels into the tumour, a process known as angiogensis or vascularisation (Fam et al., 2003). These blood vessels provide a new supply of nutrient to tumour cells, promoting tumour expansion beyond the typical avascular saturation size of 2 mm³. These new blood vessels formed by angiogensis also provide a means for metastasis, whereby tumour cells enter the blood stream, spread through the body and initiate the formation of secondary tumours.

1.2.2 in vitro tumour modelling

The effect that cancer has on the global population encourages vigorous scientific research into its treatment and prevention. One such treatment method described above are chemotherapy medications, which undergo evaluation on *in vitro* tumour cultures to assess their toxicity and effectiveness prior to *in vivo* screening. In addition to pharmaceutical research, scientists use *in vitro* tumour models to obtain a more comprehensive understanding of the *in vivo* tumour micro-environment and the complex mechanisms involved in cancer growth (Katt et al., 2016).

In vitro tumour growth can be achieved using a number of cell culturing methods, each with varying levels of complexity. Monolayer cultures are considered to be a straightforward and inexpensive approach, which involves the growth of a shallow layer of cells on an artificial substrate. This monolayer environment provides a homogeneous nutrient distribution and thus mainly consists of proliferating cells (Edmondson et al., 2014). Another cell culture are multicellular tumour spheroids, which often closely resemble the three-layer structure of an in vivo avascular tumour (see figure 1.2 and the prior subsection). As such, multicellular spheroids can better replicate in vivo responses to therapeutic agents than monolayer cultures (Shield et al., 2014). However, both of these models lack a vascular network, which limits their ability to provide any significant insight into the mechanisms giving rise to angiogenesis.

1.3 Mathematical background of tissue growth models

Extensive scientific research has been undertaken to understand the complex mechanisms underlying tissue growth. In this section, we examine various mathematical models which have been used to investigate aspects of tissue engineering and tumour growth.

1.3.1 Microscopic modelling

Some authors adopt a microscale approach toward tissue modeling, which can take the form of cellular automaton systems that seek to model interactions between a large number of individual cells (Vitvitsky, 2014; Lehotzky and Zupanc, 2019; Youssef, 2015). These systems are most often represented by a two- or three-dimensional grid partitioned into discrete elements, where each element represents a different tissue constituent; for example, extra-cellular liquid or a tissue cell. From an initial state, each element evolves based on a set of rules and the occupation of its neighbouring elements. For example, if the element is occupied by a cell then it can divide via mitosis, but not if all of the neighbouring elements are also occupied by cells. Whilst automaton systems can track the behaviour of individual cells, they can become computationally infeasible for tissue-scale simulations (Ermentrout and Edelstein-Keshet, 1993).

Of particular relevance to *in vitro* tissue engineering, Chung et al. (2010) developed an automaton model representing cellular motility within a porous scaffold, and shows that increased motility enhances cell proliferation. In this model, cells migrate via a random walk; when two cell elements collide, a rule is imposed requiring they remain stationary for a period of time. This mechanism represents the contact behaviour observed in colliding connective tissue cells (Lackie, 1986) and was responsible for localised cellular aggregation in the model. This model also considers the effects of a nutrient via a continuum reaction-diffusion equation, which is

represented on a lattice.

The effects of an avascular tumour receiving chemotherapy treatment at different intervention times and concentrations is considered via a probabilistic cellular automaton model in Pourhasanzade and Sabzpoushan (2019), In this model, the discrete elements are distinguished between six different cell types which capture the salient structure of avascular tumour growth. The chemotherapeutic effects on tumour cells are modelled via three mechanisms: cell death, reduced probability of cell proliferation and a reduced tumour carrying capacity. The relative importance of an early intervention time over drug concentration is highlighted in Pourhasanzade and Sabzpoushan (2019) by including the development of untreatable immune cells. A review of microscale approaches to model tumour growth via cellular automata is provided in Boonderick et al. (2010) and Macnamara (2021).

1.3.2 Ordinary differential equation modelling

In contrast to discrete systems, some authors adopt ordinary differential equation (ODE) models to understand how various biological tissues develops.

Some of the earliest ODE models of tissue and tumour growth employ a single equation to model a population of cells; see Murphy et al. (2016) for a review. One such model is given by

$$\frac{\mathrm{d}y}{\mathrm{d}t} = \lambda y,\tag{1.1}$$

where y(t) represents the number of cells and λ is the growth rate. Solving this ODE indicates exponential growth of a population for positive λ . This characterises the earliest stages of tumour growth, where all cells are adequently provided with nutrient via diffusion from the surrounding vasculature. Whilst single ODE models can capture salient features of tissue growth with a small number of parameters, they can be considered over-simplified in comparison to other mathematical models (Sachs et al., 2001). Additionally, Murphy et al. (2016) notes that, although single ODE models of tumour growth can exhibit a good agreement with experimental

data, they often provide an inaccurate prediction of any large-time behaviour.

A more complicated system of ODEs are developed in de Pillis et al. (2006), which model the evolution of a tumour cell population in response to concentrations of a chemo- and immuno-therapeutic drug. By identifying the stability properties of the model equilibria, conditions for tumour growth or extinction are identified in terms of parameters related to drug therapy. Additionally, the equilibrium representing tumour growth is shown to be unconditionally stable in the presence of one drug-treatment, a combination of both treatments being required for tumour extinction. This highlights the need for simultaneous use of immuno- and chemo-therapies to prevent a relapse in tumour growth post-treatment.

In Lemon et al. (2009), a system of ODEs are developed which describe the vascularisation of a porous tissue engineering scaffold. A number of variables are considered, two of which represent the density of healthy cells and capillaries. Analogous to de Pillis et al. (2006), Lemon et al. (2009) employs a stability analysis to determine the extent to which the tissue structure will vascularise. It is shown that cell death arising from inefficient vascularisation can be overcome by seeding the scaffold with an appropriate density of vascular cells.

1.3.3 Continuum partial differential equation modelling

In contrast to ODE models, continuum models of tissue growth can track the spatial evolution of tissue constituents by employing systems of partial differential equations. Whilst continuum models cannot track individual cells, they can be derived by imposing up-scaling techniques, such as volume averaging or homogenisation, on equations that govern cellular behaviour at a microscopic level (see section 1.4). These continuum models may be exploited via relevant mathematical techniques to determine relationships between parameters and model behaviours.

Some of the earliest continuum mathematics models of tissue growth examine

the diffusive nature of substances moving through cells in order to investigate how physiological processes such as oxygen transport and waste disposal affect tumour growth (Hill, 1928; Thomlinson and Gray, 1955; Burton, 1966). For example, the study by Greenspan (1972) models the principal structure of an avascular tumour by incorporating the effects of a diffusive nutrient and a growth inhibitor. More recent studies analyse how cells migrate within a tumour in response to various stimuli (McElwain and Pettet, 1993; Thompson and Byrne, 1999). For example, Pettet et al. (2001) determines how the concentration of nutrient present at the tumour edge affects the migration of cancer cells in different regions of the tumour.

In Ward and King (1997), a system of partial differential equations are derived to track the behaviour of living and dead cells in a tumour spheroid, whereby the volume exchange between the two cell species drives the velocity field within the tumour. In contrast to Greenspan (1972), Ward and King (1997) captures the initial exponential and then linear growth phases of the spheroid edge without making a priori assumptions about the spheroid structure. Expressions for these growth phases are obtained analytically via an asymptotic analysis motivated by consideration of experimental parameter values. One limitation of the model developed in Ward and King (1997) is the absence of eventual stalling of the spheroid edge, which is subsequently addressed in Ward and King (1999) by incorporating mechanisms representing the leakage and consumption of cellular material.

1.3.4 Multiphase modelling

Some authors adopt a multiphase approach to model the growth of a solid tumour or a tissue construct (O'Dea et al., 2010; Tosin and Preziosi, 2010; Sciumè et al., 2013). In contrast to some continuum approaches which model tissue as a homogeneous mass, such as Greenspan (1972), multiphase models allow the interaction of different tissue constituents, and have been proposed to be a more natural modelling framework for studying solid tumour and tissue growth than existing theories

(Byrne et al., 2002).

For example, Byrne et al. (2002) developed a multiphase model which describes the interaction between a motile cell and a inviscid liquid phase in an avascular tumour; a detailed analysis of this model is provided in Breward et al. (2002), and the cell phase in this model exhibits either travelling waves which propagate with constant speed or a steady state, both of which are in agreement with experimental observations. By neglecting viscous effects, the model of Byrne et al. (2002) reduces to a system of reaction-diffusion equations, where the diffusivity arises from a mechanism representing cell motility. This provides a physical interpretation of the diffusivity, which contrasts many other reaction-diffusion models of tumour growth (Gattenby and Gawlinski, 1996), where ad hoc assumptions regarding cellular diffusion are made. We note that a novel analysis of the model developed in Byrne et al. (2002) is presented in chapters 3 and 4 of this thesis.

In Lemon et al. (2006), a multiphase moving boundary model of *in vitro* tissue growth is developed and considers an arbitrary number of tissue constituents, i.e. phases, each of which is governed by a mass and momentum balance equation. Constitutive assumptions are defined representing cell growth and pressures arising from cell-cell and cell-scaffold interactions. Attention of this model is then restricted to an application of *in vitro* tissue engineering by considering the evolution of three phases representing motile cells, an extra-cellular liquid and a porous scaffold. This reduced model is used to investigate how mechanical pressures within growing tissue influence the aggregation or dispersion of cells in a scaffold, and the existence of these regimes are expressed in terms of the governing parameters. Lemon and King (2007a) examine travelling-wave solutions of the three-phase model formulated in Lemon et al. (2006), and find that in certain limits, the tissue propagates through the scaffold at a constant speed as either a forward or backward travelling wave, dependent on parameter values.

The three-phase model formulated in Lemon et al. (2006) is extended in Lemon

and King (2007b) to investigate the effects of nutrient limitation on *in vitro* engineered tissue. This was achieved by incorporating a concentration of nutrient at the tissue edge which diffuses inward toward the scaffold core. Solutions of this model indicate that net cell growth occurs only in a thin proliferating rim at the tissue edge. Further into the scaffold interior, an inadequate concentration of nutrient results in a necrotic core. In Lemon and King (2007b), it was shown that reducing the value of the cell-liquid drag increased cell motility, and hence mitigated the effects of nutrient depletion.

In Green et al. (2009a), a multiphase description representing the *in vitro* aggregation of liver cells is considered, comprising a cell phase and an extra-cellular liquid phase. The density and displacement of an extra-cellular matrix on which the cells were initially seeded is also considered. In contrast to Lemon et al. (2006) and Lemon and King (2007a), the effects of cell mitosis and apoptosis were neglected in Green et al. (2009a), due to the time-scale of cell aggregation being much shorter than that of cell proliferation. Solutions of the model developed in Green et al. (2009a) exhibit patterned solutions representing localised cell aggregates, whereby cells form distinct regions of high-cell density that are separated by regions of zero cell density. The results in Green et al. (2009a) suggest that the cell-matrix adhesion strength should be reduced to promote the formation of larger aggregates.

1.4 Averaged mass transfer equations for two-phase flow

Although microscopic modelling approaches can track the behaviour of cells, they contain microscale detail and can become computationally infeasible for tissue-scale simulations. In order to obtain equations that do not contain the precise details of the flow, an averaging process is exploited to relate microscopic equations to their continuum-based counterparts. In this section, we outline the method by which equations that govern the flow of two microscopic phases can be spatially averaged

so that each phase is well-defined everywhere in the material. In particular, we derive the continuum conservation of mass equation from its microscopic counterpart, which will be used to describe the transfer of mass between different constituents in the following chapters.

1.4.1 Definitions and identities

We assume that each microscopic phase can be treated as a continuum, so that the conservation of mass equation adequately describes its motion. This equation is

$$\frac{\partial \rho_k}{\partial t} + \nabla \cdot (\rho_k \mathbf{v}_k) = 0, \tag{1.2}$$

where $\rho_k(\boldsymbol{x}, t)$ is the density of the microscopic phase $k \in \{1, 2\}$ and $\boldsymbol{v}_k(\boldsymbol{x}, t)$ is the corresponding velocity field. The interface between the two phases is denoted by ∂V .

Before averaging (1.2), we state some definitions and results which are important for the averaging procedure. Given a microscopic variable $f(\boldsymbol{x}, t)$, we define its volume average as

$$\langle f \rangle = \frac{1}{V} \int_{V} f \, dV \tag{1.3}$$

where V is a closed and continuous control volume. This volume averaging operator has the properties

$$\left\langle \frac{\partial f}{\partial t} \right\rangle = \frac{\partial}{\partial t} \langle f \rangle, \qquad \langle \nabla f \rangle = \nabla \langle f \rangle.$$
 (1.4)

These relations are known as Leibniz's and Gauss's rule respectively, and are rigorously derived in Drew and Passman (1998) with respect to the volume averaging operator from (1.3).

It is instructive to isolate each phase from the whole material, V. To do this, we define the indicator function

$$I_k(\boldsymbol{x}, t) = \begin{cases} 1 & \text{if } \boldsymbol{x} \text{ is in phase } k \text{ at time } t, \\ 0 & \text{otherwise.} \end{cases}$$
 (1.5)

The proportion of the volume occupied by phase k within V is defined as $\alpha_k = \langle I_k \rangle$ and shall be referred to as the volume fraction of phase k.

The quantities ∇I_k and $\partial I_k/\partial t$ will feature in the averaging of (1.2), and satisfy the identities (Drew and Passman, 1998; Drew, 1983),

$$\nabla I_k = \boldsymbol{n}_k \delta(\boldsymbol{x} - \boldsymbol{x}_i, t), \tag{1.6}$$

$$\frac{\partial I_k}{\partial t} = -\boldsymbol{v_i} \cdot \nabla I_k,\tag{1.7}$$

where n_k is the unit normal pointing into the region within V occupied by phase k, δ is the Dirac delta function and x_i , $v_i \in \partial V$. Following Drew and Passman (1998) and Drew (1983), we now describe an approach to derive the first identity.

Since the quantity ∇I_k does not exist in a classical sense, we first multiply it by a sufficiently smooth test function $\phi(\boldsymbol{x}, t)$ which has compact support over space and time, and then integrate by parts to obtain

$$\int_{V \times \mathbb{R}_0^+} \phi \nabla I_k \, dV \, dt = \int_{\mathbb{R}_0^+} \left[I_k \phi \bigg|_V - \int_V I_k \nabla \phi \, dV \right] dt$$
 (1.8)

$$= -\int_{V_k \times \mathbb{R}_0^+} \nabla \phi \, dV \, dt, \qquad (1.9)$$

where V_k is the domain occupied by phase k, $\mathbb{R}_0^+ = [0, \infty)$ and the first term on the right hand-side of (1.8) is zero by definition of ϕ . By applying the divergence theorem to (1.9), we find that

$$\int_{V_k \times \mathbb{R}_0^+} \nabla \phi \, dV \, dt = \int_{\partial V \times \mathbb{R}_0^+} \boldsymbol{n}_k \phi \, \partial V \, dt$$
 (1.10)

$$= \int_{V \times \mathbb{R}_0^+} \boldsymbol{n}_k \delta(\boldsymbol{x} - \boldsymbol{x}_i, t) \phi \, dV \, dt, \qquad (1.11)$$

Finally, equating (1.11) with the left hand-side of (1.8), we obtain

$$\nabla I_k = \boldsymbol{n}_k \delta(\boldsymbol{x} - \boldsymbol{x}_i, t). \tag{1.12}$$

1.4.2 Averaged conservation of mass equation

Using the definitions and identities stated in the prior subsection, we now average (1.2). Multiplying (1.2) by I_k and exploiting the product rule, we obtain

$$\frac{\partial}{\partial t}(\rho_k I_k) + \nabla \cdot (\rho_k \boldsymbol{v}_k I_k) = \rho_k \left(\frac{\partial I_k}{\partial t} + \boldsymbol{v}_k \cdot \nabla I_k \right). \tag{1.13}$$

Averaging this equation via (1.3) and appealing to the identities from (1.6) and (1.7) we obtain

$$\frac{\partial}{\partial t} \langle \rho_k I_k \rangle + \nabla \cdot \langle \rho_k \boldsymbol{v}_k I_k \rangle = \langle \rho_k \boldsymbol{n}_k (\boldsymbol{v}_k - \boldsymbol{v}_i) \delta(\boldsymbol{x} - \boldsymbol{x}_i, t) \rangle. \tag{1.14}$$

The term on the right hand-side of (1.14) represents the inter-facial mass transfer between each phase, i.e., when the velocity on the interface is non-zero, $(\boldsymbol{v}_k - \boldsymbol{v}_i) \neq \mathbf{0}$, then mass is transferred into the other phase via $\boldsymbol{n}_k \delta(\boldsymbol{x} - \boldsymbol{x}_i, t)$. Following Drew (1983), we define the phasic and mass-weighted average for the quantity $f(\boldsymbol{x}, t)$ as

$$\tilde{f} = \frac{\langle I_k f \rangle}{\alpha_k}, \qquad \hat{f} = \frac{\langle I_k \rho_k f \rangle}{\alpha_k \tilde{\rho}_k}.$$
 (1.15)

Combining these with (1.14), we obtain the macroscopic averaged conservation of mass equation:

$$\frac{\partial}{\partial t}(\alpha_k \tilde{\rho}_k) + \nabla \cdot (\alpha_k \tilde{\rho}_k \hat{\boldsymbol{v}}_k) = \Gamma_k, \tag{1.16}$$

where Γ_k is equal to the right-hand side of (1.14).

1.5 Thesis objectives and structure

In this thesis, we present and analyse multiphase, moving boundary models of tissue growth. We aim to analyse the effects of tissue mechanics, cell growth and nutrient limitation on various tissue structures, and obtain novel mathematical results that can be applied to a wide class of mathematical models.

In chapter 2, we derive a multiphase, moving boundary model to represent the development of tissue in vitro in a porous tissue engineering scaffold. We consider a

cell, extra-cellular liquid and a rigid scaffold phase, and adopt Darcy's law to relate the velocity of the cell and liquid phases to their respective pressures. Cell-cell and cell-scaffold interactions which can drive cellular motion are accounted for by utilising relevant constitutive assumptions for the pressure in the cell phase. We reduce the model to a nonlinear reaction-diffusion equation for the cell phase, coupled to a moving boundary condition for the tissue edge, the diffusivity being dependent on the cell and scaffold volume fractions, cell and liquid viscosities and parameters that relate to cellular motion. Numerical simulations reveal that the reduced model admits three regimes for the evolution of the tissue edge at large time: linear, logarithmic and stationary. Employing travelling-wave and asymptotic analysis, we characterise these regimes in terms of parameters related to cellular production and motion. The results of our investigation allow us to suggest optimal values for the governing parameters, so as to stimulate tissue growth in an engineering scaffold.

Following this, in chapter 3, we analyse the multiphase, moving boundary model of tumour growth developed in Byrne et al. (2002). We consider the evolution of a motile, viscous cell phase and an inviscid extracellular liquid phase. We assume that nutrient is abundantly distributed throughout the tumour, which is physically relevant when considering the initial growth of a suspension of in vitro tumour cells (Byrne et al., 2002). In contrast to the work presented in chapter 2, the velocity of the cell and liquid phases are related to their respective pressures via momentum balance equations. As such, the reduced mathematical model complexity increases and comprises two partial differential equations that govern the cell volume fraction and the cell velocity, together with a moving boundary condition for the tumour edge. Numerical simulations of the model indicate that patterned solutions can be obtained, which correspond to multiple regions of high cell density separated by regions of low cell density. In other parameter regimes, solutions of the model can develop into a forward- or backward-moving travelling wave, corresponding to tumour growth or extinction, respectively. A travelling-wave analysis allows us to find the corresponding wave speed, as well as criteria for the growth or extinction

of the tumour. Furthermore, a stability analysis of these travelling-wave solutions provides us with criteria for the occurrence of patterned solutions. We also discuss how the initial cell distribution, as well as parameters related to cellular motion and cell-liquid drag, control the qualitative features of patterned solutions.

In chapter 4 we revisit the multiphase model of tumour growth developed in Byrne et al. (2002); however, in contrast to chapter 3, we now assume the presence of a single diffusive concentration of nutrient within the tumour. As such, the model consists of three partial differential equations governing the cell volume fraction, cell velocity and nutrient concentration, in addition to a moving boundary condition for the tumour edge. Via numerical simulations, we observe the emergence of forward-moving travelling-wave solutions that agree with the qualitative structure of the *in vitro* tumour spheroid presented in figure 1.2. A numerical and asymptotic analysis of the travelling-wave ordinary differential equations allow us to quantify the tumour structure in terms of parameters related to nutrient distribution and tissue mechanics. In other parameter regimes, the position of the tumour boundary decays exponentially toward zero, which corresponds to tumour extinction. A bifurcation analysis allows us to establish conditions for which these extinction-type solutions are observed.

We conclude and discuss the work presented in this thesis in chapter 5, and highlight a number of possible extensions.

Chapter 2

Travelling-Wave and Asymptotic Analysis of a Multiphase Moving Boundary model of Engineered Tissue Growth

2.1 Introduction

In this chapter, we develop and analyse a continuum multiphase model that represents the development of tissue in vitro in an artificial scaffold. In our model, we aim to capture key features of tissue growth and extinction whilst developing a tractable formulation. In particular, we consider a porous flow description comprising a tissue cell phase, extra-cellular liquid phase and a scaffold phase, the former two being modelled as incompressible fluids and the latter as an inert solid. The velocity of the cell and liquid phases are related to their respective pressures via Darcy's law. Tissue mechanics are accounted for by considering relevant constitutive assumptions in a similar fashion to those presented in Lemon et al. (2006) and Lemon and King (2007a). The model is reduced to a reaction-diffusion equation for the cell phase and a moving boundary condition for the tissue edge, after which travelling-wave, asymptotic and numerical methods are employed to deduce the resulting solution behaviour.

This chapter is constructed as follows. In Section 2.2, we formulate and subse-

quently reduce and non-dimensionalise the model. In Section 2.3, we present numerical solutions to the reduced model, which reveal three regimes for the evolution of the tissue edge at large time: linear, logarithmic and stationary. These numerical solutions motivate the travelling-wave and asymptotic analyses conducted in Sections 2.4 and 2.5. In Section 2.6, we draw some conclusions regarding the behaviour of the model and interpret the mathematical results in terms of the biological application.

2.2 Model development

We construct a multiphase model to describe the growth of a nutrient rich tissue within a porous tissue engineering scaffold. For simplicity, we formulate the model in a one-dimensional Cartesian geometry. The model consists of three phases: two of which are fluid phases denoted by n(x, t) and w(x, t), and represent the volume fraction of cells and extra-cellular liquid, respectively. A rigid, non-degradable scaffold with uniform volume fraction s is the third phase and remains constant, the porosity of the scaffold hence being given by 1-s. Cell growth and death occur via mass transfer between n and w. The phases satisfy the no voids volume constraint:

$$n + w + s = 1. (2.1)$$

The velocity fields $v_n(x, t)$ and $v_w(x, t)$, and pressures $p_n(x, t)$ and $p_w(x, t)$, are associated with the phases n and w accordingly. The spatial domain of the tissue evolves over time due to cellular motion, so we track it with a moving boundary, x = L(t). In the subsections that follow, we state equations that govern mass transfer between n and w, as well as provide constitutive assumptions for v_n , v_w , p_n and p_w suitable to describe tissue growth in a scaffold. We state necessary initial and boundary conditions for the variables and the moving boundary L(t), and simplify and non-dimensionalise the model.

2.2.1 Governing equations

We assume that cells proliferate and assemble daughter cells from the available liquid, and that when cells die, they decompose and dissolve into the liquid phase. In view of these processes, it is reasonable to follow Lemon et al. (2006), Byrne et al. (2002), Breward et al. (2002) and Preziosi and Tosin (2003) (and many others) and assume the densities of n and w to be equal. Following these assumptions, the mass transfer equations can be represented as

$$\frac{\partial n}{\partial t} + \frac{\partial}{\partial x}(nv_n) = \Gamma(n, w)$$
 and $\frac{\partial w}{\partial t} + \frac{\partial}{\partial x}(wv_w) = -\Gamma(n, w),$ (2.2)

where Γ is the net rate of cell proliferation. Adding the equations from (2.2) results in the overall conservation of mass condition

$$\frac{\partial}{\partial x}[nv_n + (1 - n - s)v_w] = 0, \tag{2.3}$$

where (2.1) has been used to eliminate the time derivative and to replace w with 1 - n - s.

Noting that n and w are modelled as fluids and s as a porous scaffold, we take the interphase drags to be dominated by those with the scaffold and neglect that between the tissue and liquid. In view of this, we apply Darcy's law to relate the velocity of the cell and liquid phases to their respective pressures. Following King and Franks (2004) and Eyles et al. (2019), we take

$$v_n = -\frac{K}{\mu_n(n,w)} \frac{\partial p_n}{\partial x}$$
 and $v_w = -\frac{K}{\mu_w(n,w)} \frac{\partial p_w}{\partial x}$, (2.4)

where μ_n and μ_w represent the viscosity of the cell and liquid phases and K is the permeability of the scaffold.

Remaining consistent with Lemon et al. (2006) and Lemon and King (2007a,b), we relate the cellular and extra-cellular liquid pressures via

$$p_n = p_w + \Sigma(n, s), \tag{2.5}$$

where Σ represents extra pressures that arise due to cell-cell and cell-scaffold interactions. Since the scaffold is assumed to be inert and of uniform porosity, we suppress the dependence Σ has on s from hereon for brevity. We note that combining (2.5) with the relations from (2.4) allows the elimination of p_n and p_w and provides

$$v_n = \frac{\mu_w}{\mu_n} v_w - \frac{K}{\mu_n} \frac{\partial \Sigma}{\partial x}.$$
 (2.6)

2.2.2 Initial and boundary conditions

Assuming the tissue to be symmetric about its centre (x = 0), we take

$$v_n(x, t) = v_w(x, t) = 0$$
 at $x = 0$. (2.7)

Naturally, the cell volume fraction is identically zero at the edge of the tissue:

$$n(x, t) = 0$$
 at $x = L(t)$. (2.8)

The moving boundary L(t) moves with the cell velocity, hence

$$\frac{\mathrm{d}L(t)}{\mathrm{d}t} = v_n(L(t), t). \tag{2.9}$$

The initial distribution of n and tissue boundary position respectively are denoted by

$$n(x, 0) = n_0(x)$$
 and $L(0) = L_0$. (2.10)

2.2.3 Model reduction

We reduce the model to a reaction-diffusion equation and a moving boundary condition. Integrating (2.3) and applying the boundary conditions from (2.7) provides

$$v_n = -\Phi(n)\frac{\partial n}{\partial x}, \quad \text{where} \quad \Phi = \frac{K(1-n-s)}{\mu_n(1-n-s) + \mu_w n} \frac{\mathrm{d}\Sigma}{\mathrm{d}n}.$$
 (2.11)

Here, we note μ_n and μ_w are assumed to be independent of n for simplicity. Substituting (2.11) into the first of (2.2) provides the reaction-diffusion equation:

$$\frac{\partial n}{\partial t} = \frac{\partial}{\partial x} \left(n\Phi(n) \frac{\partial n}{\partial x} \right) + \Gamma(n, w). \tag{2.12}$$

Combining (2.9) with (2.11) provides the moving boundary condition:

$$\frac{\mathrm{d}L}{\mathrm{d}t} = -\Phi(0)\frac{\partial n}{\partial x}(L(t), t), \tag{2.13}$$

where the boundary condition from (2.8) provides $\Phi(n) = \Phi(0)$ at x = L(t). Finally, (2.11) implies the boundary condition on v_n from (2.7) becomes

$$\Phi(n)\frac{\partial n}{\partial x} = 0$$
 at $x = 0$. (2.14)

2.2.4 Constitutive assumptions

We now define constitutive assumptions for Γ and Σ that are suitable to describe tissue growth in a rigid scaffold. We assume that daughter cells are constructed via mitosis using the available liquid, and that when cells die via apoptosis they dissolve into the liquid. Thus, we take

$$\Gamma(n) = r_m n(1 - n - s) - r_a n,$$
(2.15)

where r_m and r_a are the positive constant rates of cell mitosis and apoptosis, and (2.1) is used to replace w with 1 - n - s.

Following Lemon et al. (2006) and Lemon and King (2007a,b), an appropriate expression for $\Sigma(n)$ is

$$\Sigma(n) = \underbrace{\frac{\delta_n n^2}{(1 - n - s)} + \nu n}_{\text{cell-cell interactions}} + \underbrace{\frac{\delta_s s n}{(1 - n - s)} - \chi s}_{\text{cell-scaffold interactions}},$$
(2.16)

for $\nu \in \mathbb{R}$ and positive constants δ_n , δ_s and χ . The first term in (2.16) represents repulsive forces exerted between the cells at high volume fractions, as characterised by the singularity at n = 1 - s. The second term represents the propensity for cells

to disperse or aggregate, with ν taking a positive or negative value accordingly. The third term represents repulsive forces that occur due to cell-scaffold interactions, whilst the fourth describes attractive forces between the cells and scaffold. For simplicity, we take $\delta := \delta_n = \delta_s$. We note that $\Phi(n)$ must be strictly positive to prevent negative diffusion in (2.12) and nonlinear degeneracy in (2.13). This is achieved when $\nu > 0$, which is henceforth assumed. Physically, this corresponds to a tendency for cells to spread through the scaffold (Lemon et al., 2006).

2.2.5 Non-dimensionalisation

We non-dimensionalise (2.12), (2.13) and the initial and boundary conditions from (2.8), (2.10) and (2.14). By introducing the dimensionless variables

$$\hat{t} = r_m t,$$
 $\hat{x} = \sqrt{\frac{r_m}{\Phi(0)}} x,$ $\hat{L} = \sqrt{\frac{r_m}{\Phi(0)}} L,$ (2.17)

the following dimensionless model results:

$$\frac{\partial n}{\partial \hat{t}} = \frac{\partial}{\partial \hat{x}} \left(n\phi(n) \frac{\partial n}{\partial \hat{x}} \right) + n(\kappa - n), \qquad 0 < \hat{x} < \hat{L}, \tag{2.18}$$

$$\frac{\mathrm{d}\hat{L}}{\mathrm{d}\hat{t}} = -\frac{\partial n}{\partial \hat{x}}(\hat{L}, \,\hat{t}\,),\tag{2.19}$$

$$\phi(n)\frac{\partial n}{\partial \hat{x}}\Big|_{\hat{x}=0} = 0, \qquad n(\hat{L}, \hat{t}) = 0, \qquad \hat{L}(0) = \hat{L}_0, \qquad n(\hat{x}, 0) = n_0(\hat{x}), \qquad (2.20)$$

where $\kappa = 1 - s - r_a/r_m$ and $\hat{L}_0 = L_0 \sqrt{r_m/\Phi(0)}$. We also have

$$\phi(n) = \frac{\Phi(n)}{\Phi(0)} = \frac{(1-s)(1-n-s)}{(\eta(1-s)+s)(1+(\mu-1)n-s)} \left[\frac{(1-s)}{(1-n-s)^2} + \eta - 1 \right]$$
(2.21)

where $\eta = \nu/\delta$ and $\mu = \mu_w/\mu_n$. In the following, we dispense with the hat notation for clarity.

The parameter κ is shown in subsequent sections to be of crucial importance to the qualitative features of the model solutions. Physically, κ represents the difference between the scaffold porosity and the ratio between the cell death and growth rates.

We note that the scaffold permeability parameter K, as seen in (2.11), is not present in the non-dimensional model (2.18)–(2.20). However, the scalings selected in (2.17) imply that the dimensional tissue boundary position increases with the scaffold permeability.

2.2.6 Linear stability analysis and parameter values

A linear stability analysis around the spatially-uniform steady states of (2.18), $n_{\infty} = 0$, κ , provides insight into the dependence of the model behaviour on κ and $\phi(n)$. Neglecting the influence of the moving boundary condition on the stability of (2.18), we linearise on a semi-infinite domain. We substitute $n = n_{\infty} + \varepsilon \exp(i\gamma x + \lambda t)$ into (2.18) for a perturbation wave number γ and growth rate λ where $\varepsilon \ll 1$. Considering terms of $\mathcal{O}(\varepsilon)$ only, the growth rate for perturbations of wave length $2\pi/\gamma$ is

$$\lambda = -n_{\infty} \left[\gamma^2 \phi(n_{\infty}) + 2 \right] + \kappa. \tag{2.22}$$

Since $\phi(n)$ is assumed to be positive for any n, the steady state $n_{\infty} = \kappa$ is stable for all $\kappa > 0$. For $n_{\infty} = 0$, we have $\lambda = \kappa$ which indicates stability when $\kappa < 0$. In view of this, we are primarily motivated to investigate (2.18)–(2.20) for different values of κ , though variations in s, μ , and η will also be considered in part so as to deduce their optimal values for the stimulation of tissue growth.

Unless otherwise stated, we take $\mu = \eta = 1$ and we adopt the initial conditions

$$n_0(x) = \omega(1 - x^2)$$
 and $L_0 = 1$, (2.23)

so that ω denotes the cell volume fraction at x=0. Following Lemon and King (2007a,b), and unless otherwise stated, we set s=0.2 and $\omega=0.03$, the former corresponding to a scaffold with a porosity of 0.8 and is consistent with the experimental study presented in Malda et al. (2004).

2.3 Numerical results

We present and discuss the numerical solutions for n(x, t) and L(t) from the PDE system (2.18)–(2.20), paying separate attention to the cases $\kappa > 0$, $\kappa < 0$ and $\kappa = 0$.

2.3.1 Numerical methods

For numerical convenience, we fix the moving boundary by introducing the variable transform $\xi = x/L(t)$ so that $\xi \in [0, 1]$. By the chain rule we have,

$$\frac{\partial}{\partial t} \mapsto \frac{\partial}{\partial t} - \frac{\xi}{L} \frac{\mathrm{d}L}{\mathrm{d}t} \frac{\partial}{\partial \xi} \quad \text{and} \quad \frac{\partial}{\partial x} \mapsto \frac{1}{L} \frac{\partial}{\partial \xi},$$
 (2.24)

which means (2.18)-(2.20) become

$$\frac{\partial n}{\partial t} = \frac{\xi}{L} \frac{\mathrm{d}L}{\mathrm{d}t} \frac{\partial n}{\partial \xi} + \frac{1}{L^2} \frac{\partial}{\partial \xi} \left(n\phi(n) \frac{\partial n}{\partial \xi} \right) + n(\kappa - n), \qquad 0 < \xi < 1, \tag{2.25}$$

$$\frac{\mathrm{d}L}{\mathrm{d}t} = -\frac{1}{L}\frac{\partial n}{\partial \xi}(1, t),\tag{2.26}$$

$$\frac{\partial n}{\partial \xi}(0, t) = 0, \qquad n(1, t) = 0, \qquad L(0) = L_0, \qquad n(\xi, 0) = n_0(\xi).$$
 (2.27)

We numerically integrate (2.25) and (2.26) by discretising first and second order spatial derivatives using second order finite differences. Upwind finite differences were used for the second term of (2.25). Temporal derivatives are numerically integrated by utilising ode23s in MATLAB. Specifically, we partition $\xi \in [0, 1]$ uniformly so that $\xi_i = i\Delta \xi$ for i = 0, ..., N, where $\Delta \xi = 1/N$ and N+1 is the number of spatial nodes and denote $n_i = n(\xi_i, t)$. The finite difference scheme corresponding

to (2.25)-(2.27) is given by

$$\frac{\partial n}{\partial t} = \frac{\xi_i}{L} \frac{\mathrm{d}L}{\mathrm{d}t} \cdot \frac{n_{i+1} - n_i}{\Delta \xi} + \frac{n_i \phi(n_i)}{(L)^2} \cdot \frac{n_{i+1} - 2n_i + n_{i-1}}{(\Delta \xi)^2}$$
(2.28)

$$+ \frac{n_i \phi'(n_i) + \phi(n_i)}{(L)^2} \cdot \left(\frac{n_{i+1} - n_{i-1}}{2\Delta \xi}\right)^2 + n_i (\kappa - n_i), \tag{2.29}$$

$$\frac{\mathrm{d}L}{\mathrm{d}t} = -\frac{1}{L} \cdot \frac{3n_N - 4n_{N-1} + n_{N-2}}{2\Delta\xi},\tag{2.30}$$

$$n_0 = -\frac{4n_1}{3} + \frac{n_2}{3}, \qquad n_N = 0, \qquad L(0) = L_0, \qquad n(\xi_i, 0) = n_0(\xi_i), \qquad (2.31)$$

where $' \equiv d/dn$.

2.3.2 Results

For $\kappa=0.3$, as seen in Figure 2.1(a, b), we observe semi-infinite travelling waves in n and linear growth in L after a period of transient growth from their initial states. For $\kappa=0$, as seen in Figure 2.1(c), we observe n decaying from the initial data. Figure 2.1(d) shows unbounded growth in L. The inset shows L(t) and the function $\ln(t)/\sqrt{2}-1$ plotted against $\ln(t)$, from which we conclude that L grows logarithmically at large time. For $\kappa=-0.3$, as seen in Figure 2.1(e), we observe that n decays from the initial data more quickly than for $\kappa=0$. The initial growth of L shown in Figure 2.1(f) occurs due to the diffusion of n from the initial state; however, we observe the eventual formation of a steady state. Numerical simulations that are not included here suggest that travelling-wave and steady-state behaviour is exhibited by (2.18)-(2.20) for all $\kappa>0$ and $\kappa<0$, respectively.

Clearly, the case in which $\kappa > 0$ corresponds to effective tissue growth. This motivates a travelling-wave analysis of (2.18)–(2.20) for $\kappa > 0$ which is presented in Section 2.4 where we express the speed of the tissue edge in terms of the governing parameters. In Section 2.5, asymptotic solutions for n and L are found when $0 < \kappa \ll 1$, so that the cell distribution and tissue speed are explicitly available. Whilst the case $\kappa < 0$ results in tissue decay, an asymptotic analysis of (2.18)–(2.20) for this

case is presented in Section 2.5. Overall, the results in this section suggest that $\kappa > 0$ must hold for tissue growth to occur, thus suggesting that tissue engineers should ensure that the porosity of the scaffold is at least larger than the ratio between the rate of cell death and growth.

2.4 Travelling-wave analysis for $\kappa > 0$

Figures 2.1(a,b) indicate the emergence of semi-infinite travelling waves of constant speed for $\kappa > 0$. In light of this, we assume that for sufficiently large time, $L \sim ct$ where c is the constant wave speed at which the tissue edge moves. In this section, we employ travelling-wave analysis to obtain the wave speed c in terms of the governing parameters when $\kappa > 0$.

2.4.1 Formulation

We transform (2.18)–(2.20) via the travelling-wave coordinates $z = x - L \sim x - ct$ where $z \in (-\infty, 0]$. Setting n(x - ct) = n(z), we obtain

$$-c\frac{\mathrm{d}n}{\mathrm{d}z} = \frac{\mathrm{d}}{\mathrm{d}z} \left(n\phi(n) \frac{\mathrm{d}n}{\mathrm{d}z} \right) + n(\kappa - n), \tag{2.32}$$

$$n(0) = 0,$$
 $c = -\frac{\mathrm{d}n}{\mathrm{d}z}\Big|_{z=0},$ $\lim_{z \to -\infty} n(z) = \kappa,$ $\lim_{z \to -\infty} \phi(n) \frac{\mathrm{d}n}{\mathrm{d}z} = 0.$ (2.33)

Following Fadai and Simpson (2020) and Fadai (2021), we define

$$q(z) = \phi(n) \frac{\mathrm{d}n}{\mathrm{d}z}.$$
 (2.34)

Multiplying (2.32) by $\phi(n)$ and re-writing the conditions from (2.33) in terms of q(z), we obtain

$$n\phi(n)\frac{\mathrm{d}q}{\mathrm{d}z} = -q(c+q) - \phi(n)n(\kappa - n), \qquad (2.35)$$

$$n(0) = 0,$$
 $q(0) = -c,$ $\lim_{z \to -\infty} n(z) = \kappa,$ $\lim_{z \to -\infty} q(z) = 0.$ (2.36)

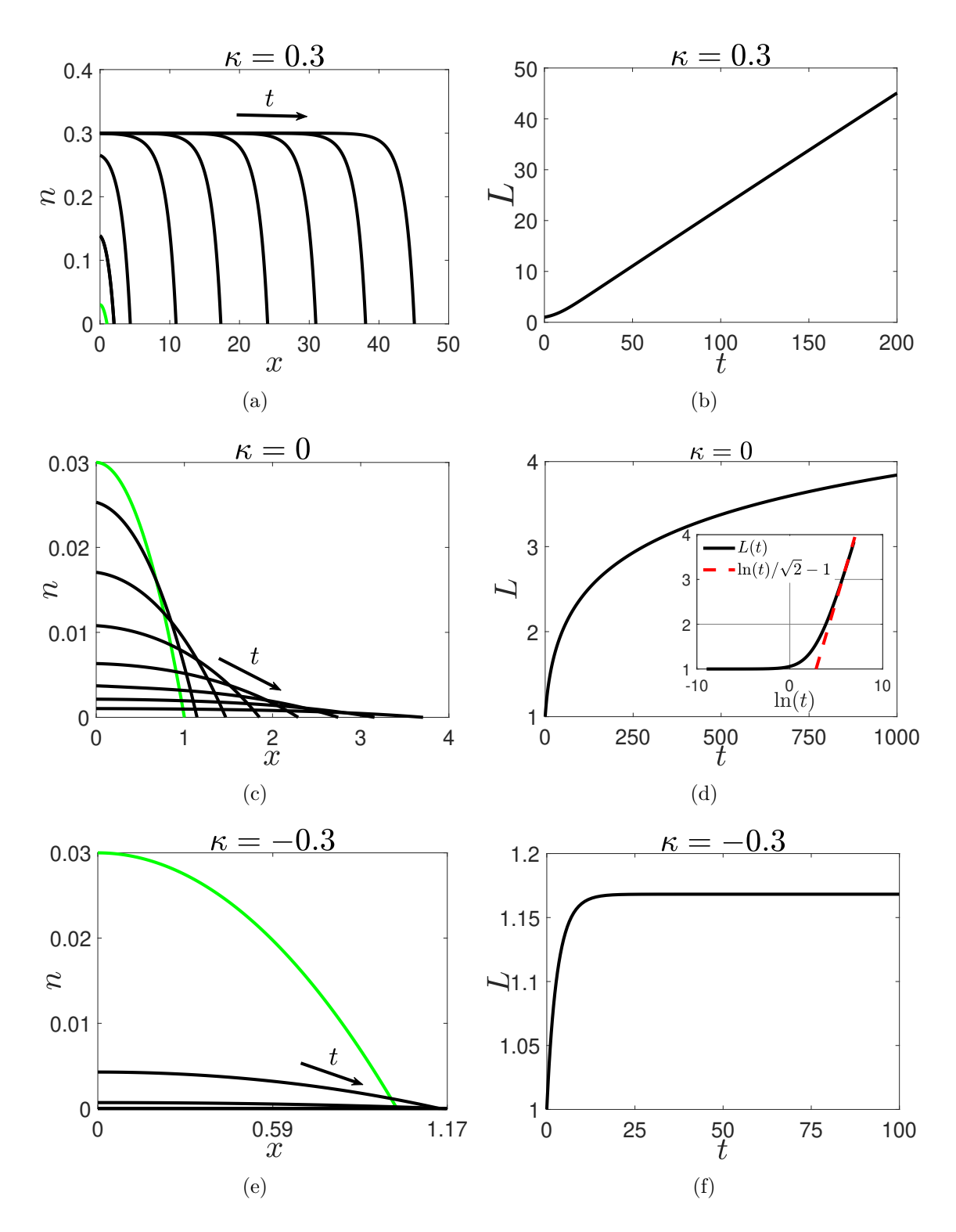


Figure 2.1: Numerical solutions of the system of PDEs from (2.18)–(2.20). The green lines in (a, c, e) represent the initial conditions $n_0(x)$ from (2.23), whereas the black lines represent n for different values of t. The black arrows point in the direction of increasing time. The dashed red line in (d) is given by $\ln(t)/\sqrt{2}-1$ and highlights the logarithmic growth of L at large time. Parameter values: $L_0 = \mu = \eta = 1$, $\omega = 0.03$ and s = 0.2

Here, we note the second boundary condition from (2.33) transforms into the second of (2.36) because $\phi(0) = 1$. Dividing (2.35) by (2.34) we have

$$\frac{\mathrm{d}q}{\mathrm{d}n} = -\frac{q(c+q) + n(\kappa - n)\phi(n)}{qn},\tag{2.37}$$

$$q(\kappa) = 0, \qquad q(0) = -c. \tag{2.38}$$

Using the shooting method to find the heteroclinic connection q(n) that connects $(n, q) = (\kappa, 0)$ to (0, -c), we can determine a numerical approximation of the wave speed in terms of the governing parameters κ , s, μ and η .

2.4.2 Shooting method

We now formulate a numerical shooting method to find the wave speed c, as stated in Section 2.4. To do this, we send trajectories of q(n) from $(\kappa, 0)$ to find a trajectory that connects to (0, -c). Computationally, it is more straightforward to shoot trajectories forwards as opposed to backwards, and we hence introduce the change of variable $X = \kappa - n$ and obtain

$$\frac{\mathrm{d}q}{\mathrm{d}X} = \frac{q(c+q) + X(\kappa - X)\phi(\kappa - X)}{q(\kappa - X)},\tag{2.39}$$

$$q(0) = 0, q(\kappa) = -c.$$
 (2.40)

Noting that the end points are computationally singular, we use $q(\zeta) = -\zeta$ and $q(\kappa - \zeta) = -c$ where $0 < \zeta \ll 1$ is some user-defined tolerance. We employ the discrepancy function

$$E(\bar{c}) = q_{\bar{c}}(\kappa - \zeta) + \bar{c}, \tag{2.41}$$

where $q_{\overline{c}}(\kappa - \zeta)$ is the solution to (2.39) evaluated at $X = \kappa - \zeta$ for a trial wave speed \overline{c} . Equation (2.39) is numerically integrated with ode23s in MATLAB with the initial condition $q(\zeta) = -\zeta$. Using fzero in MATLAB to find the zero of $E(\overline{c})$, the wave speed c and the corresponding heteroclinic trajectory q(X) is determined.

In the formulation above, the initial condition $q(\zeta) = -\zeta$ is used for simplicity; however, a more appropriate initial condition at $X = \zeta$ representing q(0) = 0 is found via an asymptotic analysis of (2.39) for $q, X \ll 1$. In these limits, (2.39) provides

$$\kappa q \frac{\mathrm{d}q}{\mathrm{d}X} \sim cq + \kappa X \phi(\kappa).$$
 (2.42)

The asymptotic solution of this equation at $X = \zeta$, and hence appropriate initial condition representing q(0) = 0 is therefore given by

$$q(\zeta) \sim \frac{c + \sqrt{c^2 + 4\kappa\phi(\kappa)}}{2\kappa}\zeta,$$
 (2.43)

for $\zeta \ll 1$. In the following subsection, we present results using the initial condition $q(\zeta) = -\zeta$ for simplicity, given that the error in q(X) and corresponding wave speed c obtained is insignificant compared to using the initial condition from (2.43).

2.4.3 Results

In Figure 2.2(a,b), the solid black line represents the relationships $c(\kappa)$ and c(s) respectively when (2.37) and (2.38) is approximated by the shooting method. The dashed green line represents these wave speeds when obtained by numerically solving (2.18)–(2.20), and computing c by evaluating dL/dt at large time. In view of the close agreement between these two approaches to computing c, we henceforth concentrate on solutions provided by (2.37) and (2.38) for simplicity.

The results presented in Figure 2.2 suggest that larger κ and smaller s increase the speed at which the tissue front grows, and since $\kappa = 1 - s - r_a/r_m$, this further corresponds to minimising r_a and maximising r_m and the porosity of the scaffold. In Figure 2.3(a, b) we present the wave speeds $c(\mu, \eta)$ for $\kappa = 0.3$ and $\kappa = 0.7$, respectively. These results suggest that, for a fixed value of κ , the wave speed is maximised when μ , $\eta \to 0$. Physically, this corresponds to the case where the viscosity of the cells is much greater than the viscosity of the liquid, and where repulsive forces exerted due to cell-cell and cell-scaffold interactions at high cell volume fractions dominate inter-cellular forces that give rise to cell dispersal. Furthermore, Figure 2.3(a, b) indicates that the dependence c has on μ is weaker for $\kappa = 0.3$ than

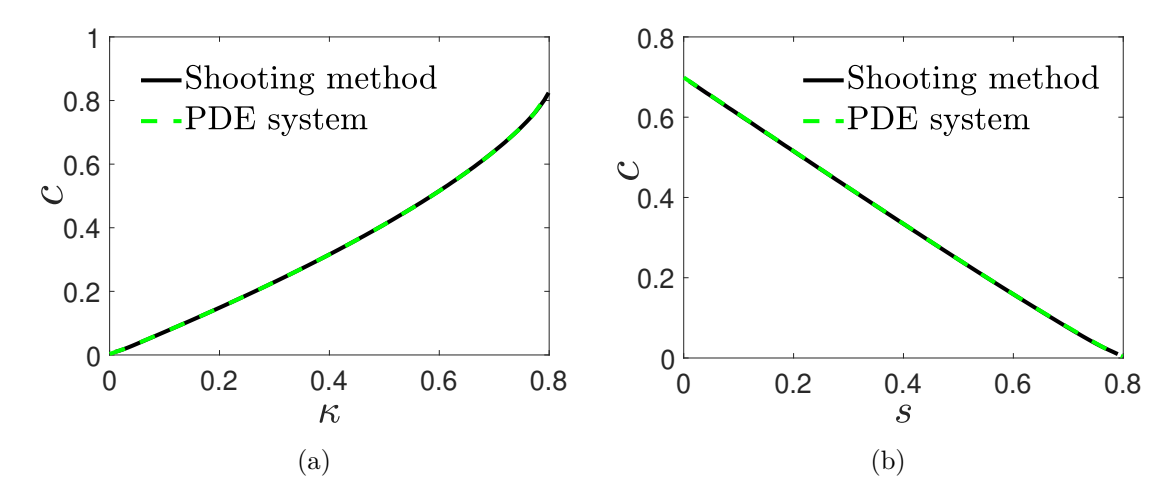


Figure 2.2: Numerical solutions for the wave speeds $c(\kappa)$ and c(s). The solid black and dashed green lines represent approximations sought by numerically solving (2.37) and (2.38) using a shooting method and the system from (2.18)–(2.20), respectively. Parameter values for (a): $\mu = \eta = L_0 = 1$, s = 0.2 and $\omega = 0.03$. Parameter values for (b): $\mu = \eta = L_0 = 1$, $r_a/r_m = 0.2$ and $\omega = 0.03$

 $\kappa=0.7$. This suggests that for smaller κ , cell-cell and cell-scaffold interactions which can drive cellular motion are more prominent in controlling the wave speed than the cell and liquid viscosities. Additionally, and in agreement with Figure 2.2(a), Figure 2.3 indicates that the wave speed increases as κ increases.

2.5 Asymptotic analysis for $|\kappa| \ll 1$

In this section, we construct asymptotic solutions for n(x, t) and L(t) for $|\kappa| \ll 1$ when $t \gg 1$. Since scaffold porosity is an experimentally readily-controllable parameter (in contrast to cell growth and death), the analysis in this section when $\kappa = 1 - s - r_a/r_m > 0$ can be associated to the case in which the scaffold porosity is low and tissue growth is successful, so that $0 < \kappa \ll 1$.

The numerical results in Figures 2.1(c, e) indicate that $n \ll 1$ holds for $\kappa < 0$ when $t \gg 1$. Furthermore, given that $\max\{n\} = \kappa$ when $\kappa > 0$, $n \ll 1$ is also expected when $0 < \kappa \ll 1$ for sufficiently large time. We therefore have $\phi(n) \sim \phi(0) = 1$ when $|\kappa| \ll 1$, so that (2.18) becomes

$$\frac{\partial n}{\partial t} = \frac{\partial}{\partial x} \left(n \frac{\partial n}{\partial x} \right) + n(\kappa - n), \qquad 0 < x < L(t), \tag{2.44}$$

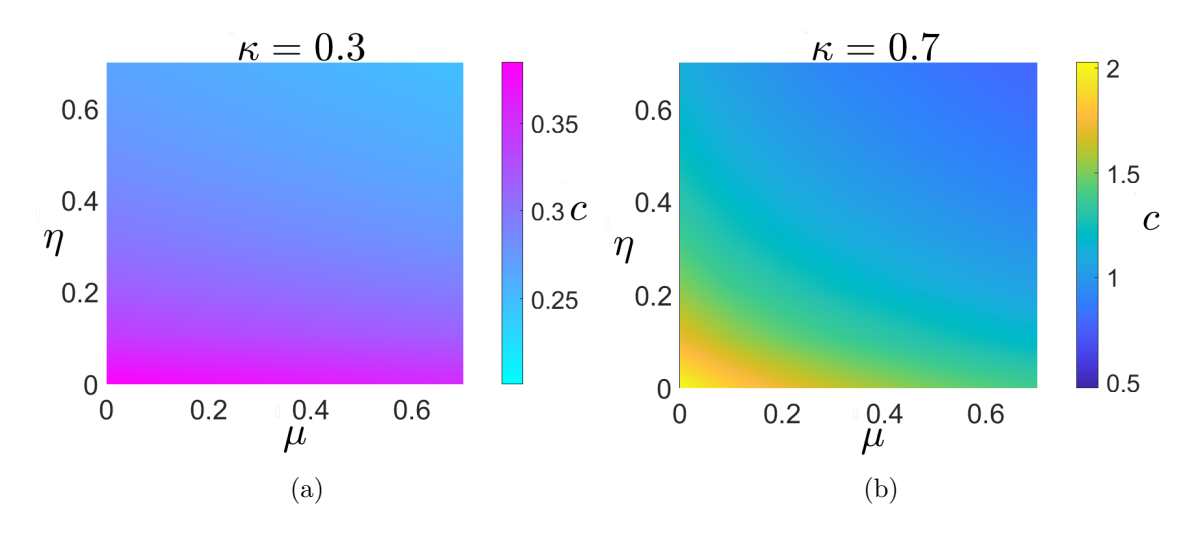


Figure 2.3: Numerical solutions for the wave speeds $c(\mu, \eta)$ for $\kappa = 0.3$ and $\kappa = 0.7$ sought by numerically solving (2.37) and (2.38) using a shooting method. s = 0.2 was used for both sub-figures. We note that the colour axes are different in each sub-figure.

for $\kappa = 0$ and $|\kappa| \ll 1$.

To aid the subsequent asymptotic analysis, we seek equations related to (2.44) and the moving boundary condition from (2.19) which are independent of κ , via the similarity reductions

$$T = f(t), \qquad n = g(T)N(x, T).$$
 (2.45)

By the chain and product rule of differentiation, (2.45) provides

$$\frac{\partial}{\partial t} \mapsto \frac{\partial}{\partial T} \frac{\mathrm{d}f}{\mathrm{d}t}, \qquad \frac{\partial n}{\partial t} = \frac{\mathrm{d}f}{\mathrm{d}t} \left[g(T) \frac{\partial N}{\partial T} + N \frac{\mathrm{d}g}{\mathrm{d}T} \right].$$
 (2.46)

In view of this, (2.44) and (2.19) provide, upon grouping like terms,

$$\frac{\mathrm{d}f}{\mathrm{d}t}g(T)\frac{\partial N}{\partial T} + \left[\frac{\mathrm{d}f}{\mathrm{d}t}\frac{\mathrm{d}g}{\mathrm{d}T} - \kappa g(T)\right]N = g^2(T)\frac{\partial}{\partial x}\left(N\frac{\partial N}{\partial x}\right) - g^2(T)N^2,\tag{2.47}$$

$$\frac{\mathrm{d}f}{\mathrm{d}t}\frac{\mathrm{d}L}{\mathrm{d}T} = -g(T)\frac{\partial N}{\partial x}(L, T). \tag{2.48}$$

We eliminate the term in the square brackets from (2.47), and then subsequently eliminate f'(t) and g(T) from (2.47) and (2.48), by enforcing that

$$\frac{\mathrm{d}f}{\mathrm{d}t}\frac{\mathrm{d}g}{\mathrm{d}T} - \kappa g(T) = 0, \qquad \frac{\mathrm{d}f}{\mathrm{d}t} = g(T), \tag{2.49}$$

the solution of which is given by

$$g(T) = \kappa T + C_1, \qquad f(t) = C_2 e^{\kappa t} - \frac{C_1}{\kappa}.$$
 (2.50)

We enforce the desirable properties that T=0 and N=n when t=0 by satisfying f(0)=0 and g(0)=1, the solution of which provides $C_1=1$ and $C_2=1/\kappa$. In summary, by noting that $g(t)=e^{\kappa t}$, and introducing the variables $n=e^{\kappa t}N(x,T)$ and $T=(e^{\kappa t}-1)/\kappa$, (2.44) and (2.19) are simplified to

$$\frac{\partial N}{\partial T} = \frac{\partial}{\partial x} \left(N \frac{\partial N}{\partial x} \right) - N^2, \qquad 0 < x < L(T), \tag{2.51}$$

$$\frac{\mathrm{d}L}{\mathrm{d}T} = -\frac{\partial N}{\partial x}(L, T),\tag{2.52}$$

which are independent of κ , as desired.

To analyse the behaviour of (2.51), we follow Newman (1980) and adopt the ansatz

$$N = A(T) - B(T)\cosh(\lambda x), \tag{2.53}$$

for some constant λ , wherein $0 < B < A \ll 1$. Imposing N(L, T) = 0 on (2.53), we obtain

$$L(T) = \lambda^{-1} \cosh^{-1} \left(\frac{A}{B} \right). \tag{2.54}$$

Substituting (2.53) into (2.51), we obtain

$$\frac{\mathrm{d}A}{\mathrm{d}T} - \frac{\mathrm{d}B}{\mathrm{d}T}\cosh(\lambda x) = -A^2 - \lambda^2 B^2 + 3AB\lambda^2 \cosh(\lambda x) + \left(\lambda^2 - \frac{1}{2}\right)\cosh^2(\lambda x), \quad (2.55)$$

whereby choosing $\lambda = 1/\sqrt{2}$ and equating like terms yields

$$\frac{dA}{dT} = -A^2 - \frac{B^2}{2}, \qquad \frac{dB}{dT} = -\frac{3AB}{2}.$$
 (2.56)

In this section, initial conditions for N and L are chosen to satisfy (2.53) and (2.54) when T = 0 – i.e.,

$$N(x, 0) = A_0 - B_0 \cosh\left(\frac{x}{\sqrt{2}}\right), \qquad L(0) = L_0$$
 (2.57)

where $A(0) = A_0$, $B(0) = B_0$ and hence $L_0 = \sqrt{2} \cosh^{-1}(A_0/B_0)$.

2.5.1 Implicit solutions for N(x, T) and L(T)

Implicit solutions for N and L are found by using the system of ODEs from (2.56) and expressing (2.54) as

$$\frac{A}{B} = \cosh\left(\frac{x}{\sqrt{2}}\right),\tag{2.58}$$

from which the large-time solutions for N and L can be deduced. First, we compute A(B) by dividing the first from (2.56) by the second to obtain

$$\frac{\mathrm{d}A}{\mathrm{d}B} = \frac{2A^2 + B^2}{3AB},\tag{2.59}$$

the solution of which is

$$A(B) = B\sqrt{1 + C_3 B^{-2/3}}, \qquad C_3 = \frac{A_0^2 - B_0^2}{B_0^{4/3}}.$$
 (2.60)

Then, substituting this into the second from (2.56) and solving for B(T), we obtain

$$K\sqrt{K^2+1} - \sinh^{-1}(K) = C_3^{3/2}T + C_4, \qquad K(T) = \frac{\sqrt{C_3}}{B^{1/3}},$$
 (2.61)

where C_4 is a constant of integration. Combining the second of (2.61) with (2.60), we obtain

$$K(T) = \sqrt{\left(\frac{A}{B}\right)^2 - 1}. (2.62)$$

Combining (2.62) with (2.61), and exploiting (2.58) we obtain an implicit solution for L(T)

$$\sinh(\sqrt{2}L) - \sqrt{2}L = \alpha T + \beta, \tag{2.63}$$

where $\alpha = 2B_0^{-2}(A_0^2 - B_0^2)^{3/2}$ and $\beta = \sinh(\sqrt{2}L_0) - \sqrt{2}L_0$. An implicit solution for N can be found by first writing (2.53) as

$$N(x,T) = B\left[\frac{A}{B} - \cosh\left(\frac{x}{\sqrt{2}}\right)\right] = B\left[\cosh\left(\frac{L}{\sqrt{2}}\right) - \cosh\left(\frac{x}{\sqrt{2}}\right)\right]$$
(2.64)

where (2.58) has been used to re-write the A/B term. A result for B(T) is found by equating the second from (2.61) with (2.62) and using (2.58). We find that

$$B(T) = \frac{\alpha}{2} \operatorname{csch}^3 \left(\frac{L}{\sqrt{2}} \right), \tag{2.65}$$

so that (2.64) becomes

$$N(x,T) = \frac{\alpha}{2} \operatorname{csch}^{3} \left(\frac{L}{\sqrt{2}} \right) \left[\cosh \left(\frac{L}{\sqrt{2}} \right) - \cosh \left(\frac{x}{\sqrt{2}} \right) \right]. \tag{2.66}$$

2.5.2 Large-time behaviour of N(x, T) and L(T)

We now deduce the large-T behaviour of N(x, T) and L(T), from which the largetime behaviour of n(x, t) and L(t) when $|\kappa| \ll 1$ can subsequently be determined. Guided by the numerical results from Figure 2.1(d), the evolution of L satisfies $L \gg L_0$ for sufficiently large T, so we have from (2.63) that

$$\frac{e^{\sqrt{2}L}}{2} - \sqrt{2}L = \alpha T + \mathcal{O}(1), \qquad (2.67)$$

which is then inverted to give

$$L(T) \sim \frac{\ln(2\alpha T)}{\sqrt{2}} \left(1 + \frac{1}{\alpha T} \right) \tag{2.68}$$

for $T \gg 1$. Equation (2.66) and the leading-order term in the above expansion are used to find the following large-T approximation for N:

$$N(x, T) \sim T^{-1} - \sqrt{\frac{2}{\alpha}} \cosh\left(\frac{x}{\sqrt{2}}\right) T^{-3/2}.$$
 (2.69)

We now exploit (2.69) and (2.68) to deduce the large-time behaviour of n(x, t) and L(t) when $|\kappa| \ll 1$.

2.5.3 Large-time behaviour of n(x, t) and L(t)

When $0 < \kappa \ll 1$, then n(x, t) takes the form of a travelling wave of constant speed and $L \gg L_0$ for $t \gg 1$. In contrast, when $\kappa < 0$, the numerical results in Figure 2.1(f) suggest that $L \to L_\infty$ as $t \to \infty$ for some finite constant L_∞ . In general, a large-time solution for L is unavailable given that $L_\infty \gg L_0$ does not necessarily hold when $t \gg 1$; however, when $|\kappa| \ll 1$, then t = T to leading order at $t = \mathcal{O}(1)$, and L evolves according to (2.68) until $t = \mathcal{O}(1/|\kappa|)$. Therefore, since $L \gg L_0$ when $|\kappa| \ll 1$ and $t \gg 1$, (2.68) becomes

$$L \sim \frac{1}{\sqrt{2}} \ln \left(\frac{2\alpha (e^{\kappa t} - 1)}{\kappa} \right) \left(1 + \frac{\kappa}{\alpha (e^{\kappa t} - 1)} \right)$$
 (2.70)

for $|\kappa| \ll 1$ and $t \gg 1$. Equation (2.70) implies that $L \sim \kappa t/\sqrt{2}$ when $0 < \kappa \ll 1$ and $t \gg 1$. Therefore, travelling waves propagate with speed $c \sim \kappa/\sqrt{2}$ when $0 < \kappa \ll 1$, this being in agreement with the numerical results from Figure 2.2(a). For $0 < \kappa \ll 1$, (2.70) also indicates that the growth of the tissue edge is logarithmic until $t = \mathcal{O}(1/\kappa)$ and linear thereafter. If tissue growth is successful, this suggests the formation of travelling waves with constant speed is delayed when the scaffold porosity is low. When $\kappa < 0$, the exponential terms from (2.70) are negligible as $t \to \infty$ and we obtain

$$L_{\infty} \sim \frac{1}{\sqrt{2}} \ln \left(\frac{2\alpha}{|\kappa|} \right) \left(1 + \frac{|\kappa|}{\alpha} \right)$$
 (2.71)

when $\kappa < 0$ and $|\kappa| \ll 1$.

The leading order logarithmic terms in (2.70) and (2.66) are used to find the following large-time approximations for n when $|\kappa| \ll 1$:

$$n \sim \kappa - \sqrt{\frac{2\kappa^3}{\alpha}} \cosh\left(\frac{x}{\sqrt{2}}\right) e^{-\kappa t/2} \quad \text{for} \quad 0 < \kappa \ll 1,$$
 (2.72)

$$n \sim \frac{|\kappa|e^{-|\kappa|t}}{1 - e^{-|\kappa|t}} \left[1 - \sqrt{\frac{2|\kappa|}{\alpha(1 - e^{-|\kappa|t})}} \cosh\left(\frac{x}{\sqrt{2}}\right) \right] \quad \text{for} \quad \kappa < 0 \quad \& \quad |\kappa| \ll 1.$$

$$(2.73)$$

We note that (2.70) and (2.72) hold for $\kappa = \mathcal{O}(1)$ if $\mu \ll 1$ and $\eta \gg 1$ because $L \gg L_0$ and $\phi(n) \sim 1$ in this case. Furthermore, for $\kappa < 0$ and $|\kappa| = \mathcal{O}(1)$, then (2.66) suggests that $n = \mathcal{O}(e^{\kappa t})$ at large time since $L_{\infty} = \mathcal{O}(L_0)$. In Figures 2.4 and 2.5, we compare the numerical solution for n and L when obtained by numerically solving the PDE system from (2.18)–(2.20) for $\kappa = 0.001$ and $\kappa = -0.001$ against their respective asymptotic solutions from (2.72), (2.73) and (2.70). Overall, an excellent agreement between the numerical and asymptotic solutions is observed. The large-T behaviour for N and L characterised by (2.68) and (2.69), and hence the asymptotic approximations from this sub-section, are only valid for initial conditions

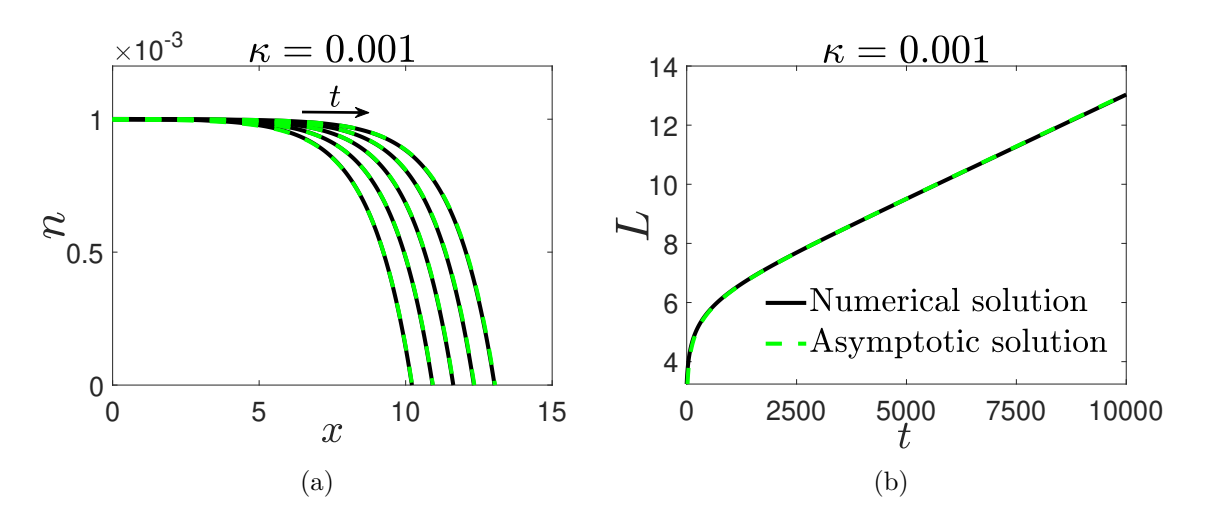


Figure 2.4: Numerical solution (solid black line) of the PDE system from (2.18)–(2.20) vs asymptotic solution (dashed green line) from (2.72) and (2.70) for n (a) and L (b) for $\kappa=0.001$. Solutions for n are presented on $t\in[6000,\,10000]$ at intervals of 1000. Initial conditions for the numerical simulations were chosen to satisfy (2.53) and (2.54). Parameter values: $\mu=\eta=1,\,s=0.2,\,A_0=0.05$ and $B_0=0.01$

that satisfy (2.53) and (2.54). We now show that solutions of (2.51) and (2.44) converge to solutions similar to that of (2.68) and (2.69) for a wider class of initial data.

2.5.4 Convergence of asymptotic solutions

Since the choice of initial cell distribution within the scaffold is likely to vary substantially in practice, it is important to determine the large-T behaviour of N and L for a wider class of initial data, such as those from (2.23). The asymptotic behaviour of (2.51) as $T \to \infty$ comprises an interior layer near the interface within which the similarity reduction $N \sim T^{-1}f(\theta)$ holds where $\theta = x - L$ and $L = b \ln(T)$, so that $f(\theta)$ satisfies

$$-b\frac{\mathrm{d}f}{\mathrm{d}\theta} = \frac{\mathrm{d}}{\mathrm{d}\theta} \left(f\frac{\mathrm{d}f}{\mathrm{d}\theta} \right) + f(1-f). \tag{2.74}$$

Following familiar arguments to that of the Porous Fisher Equation (Aaronson, 1980; Murray, 2002), although we emphasise that N is not a travelling wave of the usual form, the solution to (2.74) is given by

$$f = 1 - e^{\theta/\sqrt{2}}, \qquad b = \frac{1}{\sqrt{2}}.$$
 (2.75)

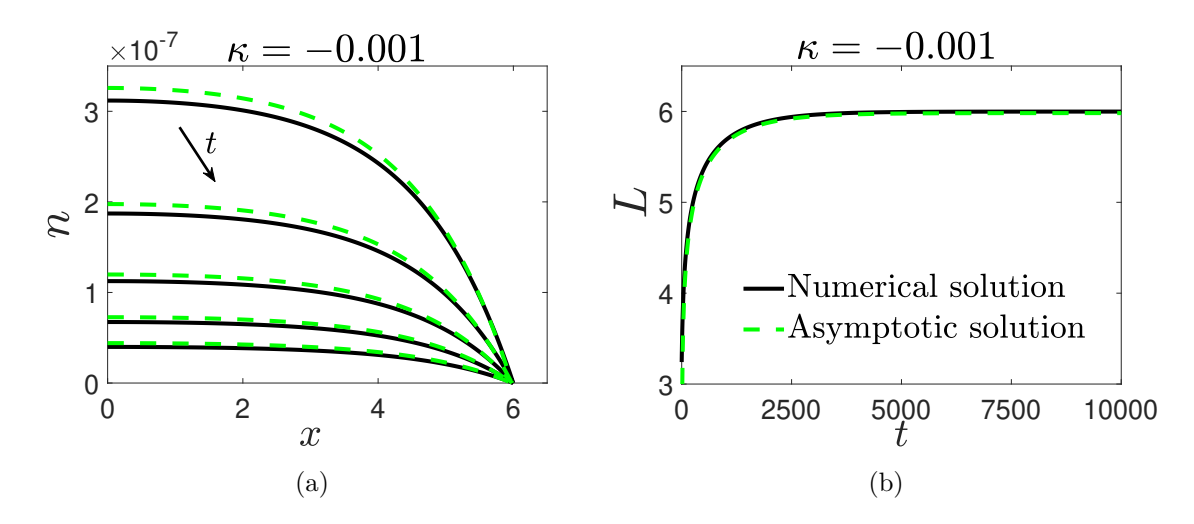


Figure 2.5: Numerical solution (solid black line) of the PDE system from (2.18)–(2.20) vs asymptotic solution (dashed green line) from (2.73) and (2.70) for n (a) and L (b) for $\kappa = -0.001$. Solutions for n are presented on $t \in [8000, 10000]$ at intervals of 500. Initial conditions for the numerical simulations were chosen to satisfy (2.53) and (2.54). Parameter values: $\mu = \eta = 1$, s = 0.2, $A_0 = 0.05$ and $B_0 = 0.01$

For $x = \mathcal{O}(1)$, setting

$$N = T^{-1} + G(x, T) (2.76)$$

implies that

$$\frac{\partial G}{\partial T} = T^{-1} \frac{\partial^2 G}{\partial x^2} - 2T^{-1} G, \tag{2.77}$$

the solution to which that matches into the exponential terms in (2.75), and hence the corresponding term in the interior layer, is given by

$$G = -m \cosh\left(\frac{x}{\sqrt{2}}\right) T^{-3/2} \tag{2.78}$$

for some unknown constant m, and this dominates the asymptotic behaviour of (2.77) as $T \to \infty$. Therefore, (2.76) becomes

$$N \sim T^{-1} - m \cosh\left(\frac{x}{\sqrt{2}}\right) T^{-3/2}$$
 (2.79)

where m depends on the initial data. Since N(L, t) = 0, (2.79) implies that

$$L \sim \sqrt{2} \cosh^{-1} \left(\frac{\sqrt{T}}{m} \right) \sim \frac{1}{\sqrt{2}} \ln \left(\frac{4T}{m^2} \right)$$
 (2.80)

for $T \gg 1$. By comparing (2.79) and (2.69), we see that the asymptotic structure is retained despite the initial cell distribution for large T. In addition, (2.80) suggests that the choice of initial cell distribution does not affect the speed at which the tissue

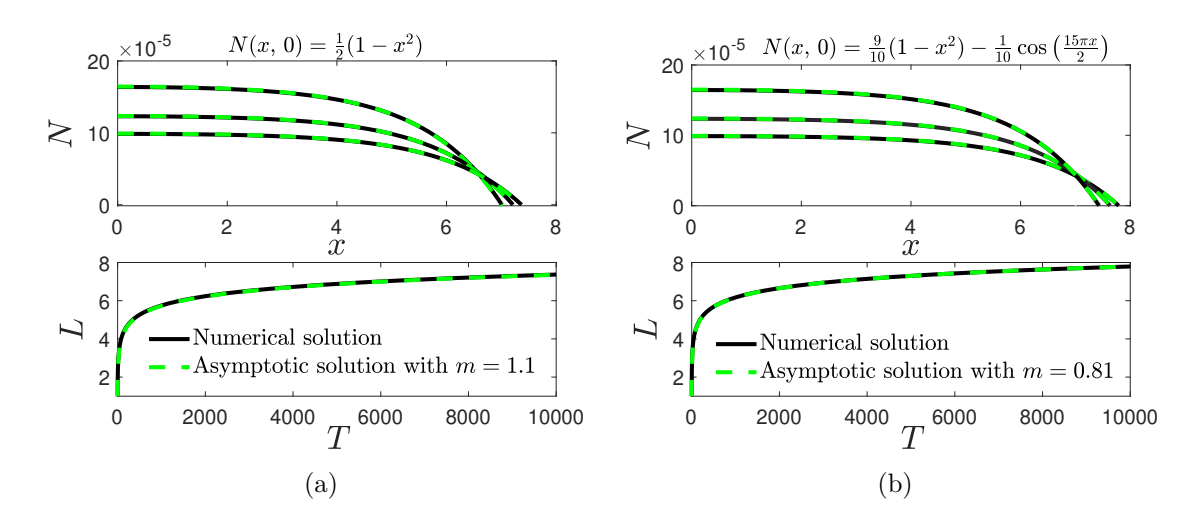


Figure 2.6: Numerical solution (solid black line) of the PDE system from (2.51) and (2.44) vs asymptotic solution (dashed red line) from (2.79) and (2.80) for n and L for different initial conditions N(x, 0) and $L_0 = 1$. Solutions for n are presented on $T \in [6000, 10000]$ at intervals of 1000. The values of m in (a) and (b) are selected to provide a good agreement between the asymptotic and numerical solutions.

edge moves for large T, but does affect the position of the tissue boundary. We note that if N(x, 0) is chosen to satisfy (2.53), then (2.69) indicates that $m = \sqrt{2/\alpha}$.

In Figure 2.6, we compare the numerical solutions for N and L when obtain by numerically solving the PDE system from (2.51) and (2.44) against the asymptotic solutions from (2.79) and (2.80) for two choices of N(x, 0) and $L_0 = 1$. The value of L_0 was found by solving $N(L_0, 0) = 0$. For both N(x, 0), we are able to choose an m that provides excellent agreement between the numerical and asymptotic solutions. We note that the large-time behaviour for n(x, t) and L(t) when $\kappa = 0$ can be extracted directly from (2.79) and (2.80) given that N = n when $\kappa = 0$ and $\lim_{\kappa \to 0} T = t$. This justifies the numerical results observed Figure 1(c, d).

2.6 Conclusions

In this chapter, we present a multiphase model to represent the development of tissue *in vitro* within a porous tissue engineering scaffold. We consider a tissue cell phase, extra-cellular liquid phase and a scaffold phase, and adopt Darcy's law to relate the velocity of the cell and liquid phases to their respective pressures. The

43

model includes mechanisms to represent cell growth and death, and pressures that arise from cell-cell and cell-scaffold interactions. We employ a moving boundary, x = L(t), to track the speed at which the tissue edge propagates through the scaffold. We reduce the model to a nonlinear reaction-diffusion equation for the cell volume fraction, n(x, t), and a moving boundary condition for the tissue edge. The diffusivity of the reaction-diffusion equation is dependent on the cell and scaffold volume fractions; cell and liquid viscosities, and pressures that arise from cell-cell and cell-scaffold interactions. Non-dimensionalisation of the model shows that the tissue boundary position increases with the scaffold permeability, and exposes important dimensionless groupings. One such grouping, κ , that describes the difference between the scaffold porosity and the ratio between the cell death and growth rates is of crucial importance to the qualitative features of the cell phase evolution. The model admits three regimes for the evolution of the cell volume fraction and the moving boundary, based on the sign of κ . Employing travelling-wave and asymptotic analysis, we characterise these regimes in terms of κ and parameters related to cellular motion.

The case in which $\kappa > 0$ corresponds to the successful growth of tissue, which suggests that tissue engineers should ensure that the porosity of the scaffold is at least larger than the ratio between the rate of cell death and growth. For $\kappa > 0$, we show that the cell volume fraction, n(x, t), spreads through the scaffold as a semi-infinite travelling wave with constant speed, emerging from the steady state $n = \kappa$. Employing travelling-wave analysis, we accurately compute the wave speed (i.e., the speed at which the tissue edge moves through the scaffold) as a function of the governing parameters. We find that the wave speed is greatest when the rate of apoptosis is negligible in comparison to that of mitosis and when repulsive forces exerted due to cell-cell and cell-scaffold interactions at high cell volume fractions dominate inter-cellular forces that give rise to cell dispersal. We also find that the wave speed increases as the scaffold porosity increases; however, we note that the cells will require a sufficient amount of scaffold on which to attach, so an upper bound

on the porosity is to be expected. Furthermore, we deduce that for smaller values of κ , and hence scaffolds with small porosities, cell-cell and cell-scaffold interactions which can drive cellular motion are more prominent in controlling the wave speed than the cell and liquid viscosities.

For $|\kappa| \ll 1$, we employ asymptotic analysis to find explicit solutions for n and L. Since scaffold porosity is a readily-controllable parameter (in contrast to cell growth and death), the analysis in this section when $\kappa = 1 - s - r_a/r_m > 0$ can be associated to the case in which the scaffold porosity is low and tissue growth is successful, so that $0 < \kappa \ll 1$. When $|\kappa| \ll 1$, the growth of the tissue edge is logarithmic until $t = \mathcal{O}(1/\kappa)$ and linear thereafter, thus suggesting the formation of travelling waves with constant speed is delayed as $\kappa \to 0^+$, and hence when the scaffold porosity is low. For $\kappa < 0$, we deduce that the cell volume fraction decays exponentially with rate κ at large time, with the moving boundary tending towards a steady state. For $\kappa < 0$ and $|\kappa| \ll 1$, the evolution of the L is shown to be logarithmic until $t = \mathcal{O}(1/\kappa)$ and approaches a steady state thereafter, the value of which is found explicitly and related to κ and the initial conditions employed in the model. For $|\kappa| \ll 1$, we also demonstrated that the choice of initial cell distribution does not affect the eventual distribution of cells within the scaffold, nor the speed at which the tissue edge moves, but does affect the position of the tissue boundary.

The model developed in this chapter, while tractable and simplified, highlights some important results that may provide a basis for optimising in vitro growth and culture conditions. For instance, we find that tissue growth only occurs when the scaffold porosity is larger than the ratio between the rate of cell death and growth. Consequently, we advise that tissue engineers consider utilising scaffolds with the maximum available pore space, bearing in mind that there is an upper limit to allow for proper cell-scaffold attachment. Furthermore, our findings indicate that the growth rate of the tissue is quickest when the cellular viscosity is larger than that of the liquid. To optimize growth conditions, it is therefore advisable to minimize the viscosity of the growth medium. Moreover, if feasible, it is advantageous to

select a cell line with a higher viscosity.

For a functional tissue construct to develop within a scaffold, cells must be exposed to the correct environment and stimulated with growth factors such as oxygen. There must also be a sufficient amount of scaffold on which the cells can adhere. Whilst key features of tissue growth such as cell mitosis, apoptosis and motion are included in this chapter, concepts such as environmental pressures, cellular adhesion, and nutrient supply have not been considered. Therefore, following Lemon and King (2007a), a natural extension of this work would include examining the influence that nutrient limitation has on cell growth. We leave these extensions for future consideration.

Chapter 3

Pattern Formation and Travelling Waves in a Multiphase Moving Boundary Model of Tumour Growth

3.1 Introduction

In this chapter, we analyse patterned and travelling-wave solutions of the multiphase, moving boundary model developed in Byrne et al. (2002). This model describes solid tumour growth, and considers the evolution of a motile, viscous cell phase and an inviscid extra-cellular liquid phase, both of which are modelled as incompressible fluids. Tissue mechanics, cellular growth and a mechanism to represent cell-liquid drag are accounted for by considering relevant constitutive assumptions in a similar fashion to those in Byrne et al. (2002) and Breward et al. (2002).

The tumour growth model of Byrne et al. (2002) analysed in this and the subsequent chapter consists of mass and momentum balance equations, and are similar to those derived in Lemon et al. (2006) which describe tissue engineering. In contrast to the model of Byrne et al. (2002), the model of Lemon et al. (2006) has been analysed extensively in the context of travelling waves (Lemon and King, 2007a) and nutrient limitation (Lemon and King, 2007b) – this provides a motivation for switching application from tissue engineering (see chapter 2) to tumour growth.

Following King and Franks (2004), we assume that nutrient is abundantly distributed throughout the tumour. In the context of *in vivo* tumour growth, this assumption is physically relevant where the tumour is in the initial stage of growth and all cells are adequately nourished (Franks and King, 2003). This nutrient-rich assumption is also appropriate when considering the initial growth of a suspension of *in vitro* tumour cells (Byrne et al., 2002). Whilst the model developed in Byrne et al. (2002) pertains to both *in vivo* and *in vitro* tumour growth, we emphasise that the mathematical results obtained in its analysis can be applied to a wider class of multiphase tissue growth models, such as that in Lemon and King (2007a).

The chapter is constructed as follows. In section 3.2, the model from Byrne et al. (2002) is stated and subsequently simplified and non-dimensionalised. Following this, some exemplar numerical solutions of the model are presented in section 3.3, which exhibit patterned solutions and forward- and backward-moving travelling waves. In section 3.4, a travelling-wave analysis is presented. This allows us to find the speed of travelling waves, as well as criteria for the growth or extinction of the tumour. We also present a stability analysis of these travelling-wave solutions in section 3.4 and thereby obtain criteria for when patterned solutions can occur. In section 3.5, we neglect the effect of the moving tumour edge and determine the stability of a spatially-uniform steady state. A comparison between the results of the travelling-wave and spatially-uniform stability analysis allows us to suggest that the moving boundary does not contribute to the formation of spatial patterns. In section 3.6, we examine the qualitative features of patterned solutions. We find that the initial cell distribution and the value of the cell-liquid drag have a more significant effect on the features of patterns, in comparison to the strength of forces generated by cellular motion. In section 3.7, we briefly discuss and analyse a parameter regime substantiated by experimental data in which the model can be reduced to a system of nonlinear ordinary differential equations. Finally, in section 3.8, we discuss the behaviour of the model and highlight the mathematical and biological results obtained in its analysis.

3.2 Model development

In this section, we state the two-phase model developed in Byrne et al. (2002) which describes the growth of a solid tumour. Following King and Franks (2004), we assume that nutrient is abundantly distributed throughout the tumour; see section 3.1 for a discussion regarding the biological relevance of this assumption. For simplicity, we formulate the model in a one-dimensional Cartesian geometry.

The tumour model of Byrne et al. (2002) consists of two phases, denoted by n(x, t) and w(x, t), that represent the volume fraction of cells and extracellular liquid, respectively. These phases satisfy the no-voids volume constraint

$$n + w = 1. (3.1)$$

The velocity fields $v_n(x, t)$ and $v_w(x, t)$, pressures $p_n(x, t)$ and $p_w(x, t)$ and stress tensors $\sigma_n(x, t)$ and $\sigma_w(x, t)$ are associated with the phases n and w, accordingly. We model the cell and liquid phases as viscous and inviscid fluids, respectively. The spatial domain of the tumour evolves over time due to cellular motion, so the volume fractions n and w evolve on the moving domain $0 \le x \le L(t)$, where x = 0 and x = L(t) denote the tumour core and tumour edge, respectively. The model is developed by considering mass and momentum balances for each phase, assuming that the phases are incompressible with equal density, and by neglecting inertial effects.

3.2.1 Governing equations

As in section 2.2.1, we assume that cells assemble daughter cells from the available liquid, and that when cells die, they decompose and dissolve into the liquid phase. In view of these processes, we assume the densities of n and w to be equal, so that the mass transfer equations can be represented as

$$\frac{\partial n}{\partial t} + \frac{\partial}{\partial x}(nv_n) = \Gamma(n, w)$$
 and $\frac{\partial w}{\partial t} + \frac{\partial}{\partial x}(wv_w) = -\Gamma(n, w),$ (3.2)

where Γ is the net rate of cell proliferation. Adding the equations from (3.2) results in the overall conservation of mass condition

$$\frac{\partial}{\partial x}[nv_n + (1-n)v_w] = 0, \tag{3.3}$$

where (3.1) has been used to eliminate the time derivative and to replace w with 1-n.

To develop momentum balance equations, we follow Breward et al. (2002) and assume that the Reynolds number corresponding to the flow is $Re \approx 10^{-2}$, so that inertial effects may be neglected. Furthermore, we assume that momentum due to mass transfer is negligible and that no external forces act on the tumour. Following these assumptions, the momentum balance equations are merely force balance equations given by

$$\frac{\partial}{\partial x}(n\sigma_n) + F_{nw} = 0, \qquad \frac{\partial}{\partial x}(w\sigma_w) + F_{wn} = 0, \tag{3.4}$$

where F_{nw} describe the forces exerted on the cells by the liquid, and vice versa. By Newton's second law we have $F_{nw} = -F_{wn}$, which means the sum of the conditions from (3.4) provides

$$\frac{\partial}{\partial x}(n\sigma_n + (1-n)\sigma_w) = 0, \tag{3.5}$$

where (3.1) has been used to replace w with 1 - n. Remaining consistent with Breward et al. (2002) and Byrne et al. (2002), we relate the cellular and extracellular liquid pressures via

$$p_n = p_w + \Sigma(n), \tag{3.6}$$

where Σ represents extra pressures that arise due to cell-cell interactions.

3.2.2 Constitutive assumptions

We now define constitutive assumptions for σ_n , σ_w , F_{wn} , Σ and Γ that are suitable to describe tumour growth. As noted above, we assume that the cell and liquid phases are both incompressible, and are viscous and inviscid fluids, respectively. In

view of this, we set

$$\sigma_n = -p_n + \mu \frac{\partial v_n}{\partial x}, \qquad \sigma_w = -p_w,$$
(3.7)

where μ represents the viscosity of the cell phase. We assume that F_{wn} consists of contributions due to pressure and drag, so that

$$F_{wn} = p_w \frac{\partial w}{\partial x} + \chi n w (v_n - v_w), \tag{3.8}$$

where χ represents the value of the interphase drag between the cells and the liquid. We note that the first term of (3.8) describes forces exerted by phase n on phase w, the factor of $\frac{\partial w}{\partial x}$ is necessary to counter interfacial stress arising from the first term in the second equation from (3.7), i.e. the stress generated by the passive liquid phase w coming into contact with itself.

We assume that daughter cells are constructed via mitosis using the available liquid, and that when cells die via apoptosis they dissolve into the liquid. Thus, we take

$$\Gamma(n) = r_m n(1-n) - r_a n, \tag{3.9}$$

where r_m and r_a are the positive constant rates of cell mitosis and apoptosis, and (3.1) is used to replace w with 1 - n.

Following Byrne et al. (2002) and Green et al. (2009b), an appropriate expression for $\Sigma(n)$ is

$$\Sigma(n) = \tau \frac{n(n-\phi)}{(1-n)},\tag{3.10}$$

where $0 < \phi < 1$ is the natural packing density of the cells and τ represents the cells' affinity for the natural packing density Breward et al. (2002). When $n > \phi$, the cells' membranes experience stress, and the cells will repel each other to relieve it. This repulsion becomes large as the available space for the cells decreases, which is reflected in the singularity at n = 1. When $n < \phi$, the cells will attract one another, due to their filopodia coming into contact (Breward et al., 2002). Necessarily, we have $\Sigma(0) = 0$.

3.2.3 Initial and boundary conditions

Assuming the tissue to be symmetric about its centre (x = 0), we take

$$v_n(x, t) = v_w(x, t) = 0$$
 at $x = 0$. (3.11)

At the moving boundary, we follow Breward et al. (2002) and allow the free passage of the liquid, so that

$$p_w(x, t) = 0$$
 at $x = L(t)$. (3.12)

Furthermore, we assume that the tumour edge is stress free, so that $\sigma_n(L(t), t) = 0$. In view of this, a combination of (3.7), (3.6) and (3.12) provides

$$\mu \frac{\partial v_n}{\partial x} = \Sigma(n)$$
 at $x = L(t)$. (3.13)

The moving boundary L(t) moves with the cell velocity, hence

$$\frac{\mathrm{d}L(t)}{\mathrm{d}t} = v_n(L(t), t). \tag{3.14}$$

The initial distribution of n and tissue boundary position respectively are denoted by

$$n(x, 0) = n_i(x)$$
 and $L(0) = L_0$. (3.15)

Various choices for $n_i(x)$ are made throughout the chapter.

3.2.4 Model reduction

We now combine and simplify some of the equations discussed in this chapter. Integrating (3.3) with respect to x and then imposing the first two boundary conditions from (3.11) we obtain

$$v_n = -\frac{1-n}{n}v_w. (3.16)$$

Substituting the relations from (3.7) into (3.5), integrating with respect to x and using the boundary conditions from (3.12) and (3.13), we obtain

$$p_w = \mu n \frac{\partial v_n}{\partial x} - n\Sigma(n). \tag{3.17}$$

Now, substituting (3.8), (3.16) and (3.17) into the first of (3.4) provides

$$\mu \frac{\partial}{\partial x} \left(n \frac{\partial v_n}{\partial x} \right) - \frac{\partial}{\partial x} \left[n \Sigma(n) \right] - \chi \frac{n v_n}{1 - n} = 0. \tag{3.18}$$

3.2.5 Non-dimensionalisation

We non-dimensionalise the reduced model, namely the first from (3.2), (3.18), the first from (3.11), (3.13), (3.14) and (3.15). By introducing the dimensionless variables

$$\hat{t} = \frac{\tau}{\mu}t, \qquad \hat{x} = \frac{x}{L_0} \qquad \hat{v}_n = \frac{\mu}{\tau L_0}v_n, \qquad \hat{L} = \frac{L}{L_0},$$
 (3.19)

the following dimensionless model results:

$$\frac{\partial n}{\partial \hat{t}} + \frac{\partial}{\partial \hat{x}} (n\hat{v}_n) = \hat{\Gamma}(n), \qquad 0 < \hat{x} < \hat{L}, \qquad (3.20)$$

$$\frac{\partial}{\partial \hat{x}} \left(n \frac{\partial \hat{v}_n}{\partial \hat{x}} \right) - \frac{\partial}{\partial \hat{x}} \left[n \hat{\Sigma}(n) \right] - \kappa \frac{n \hat{v}_n}{1 - n} = 0, \qquad 0 < \hat{x} < \hat{L}, \tag{3.21}$$

$$\frac{\mathrm{d}\hat{L}}{\mathrm{d}\hat{t}} = \hat{v}_n(\hat{L}, \,\hat{t}),\tag{3.22}$$

$$\frac{\partial \hat{v}_n}{\partial \hat{x}}\Big|_{\hat{x}=\hat{L}} = \hat{\Sigma}(n)\Big|_{\hat{x}=\hat{L}}, \qquad \hat{v}_n(0,\,\hat{t}) = 0, \qquad n(\hat{x},\,0) = n_i(\hat{x}), \qquad \hat{L}(0) = 1, \quad (3.23)$$

where

$$\hat{\Gamma}(n) = \hat{r}_m n(1-n) - \hat{r}_a n, \qquad \hat{\Sigma}(n) = \frac{\Sigma(n)}{\tau}, \tag{3.24}$$

and $\hat{r}_m = r_m \mu / \tau$, $\hat{r}_a = r_a \mu / \tau$ and $\kappa = \chi L_0^2 / \mu$. In the proceeding, we dispense with the hat notation for clarity.

Throughout this chapter, we assume that $r_a < r_m$ so that there is net cell growth. As shown in Byrne et al. (2002) and Breward et al. (2002), combining (3.20), (3.22) and the first from (3.23) at x = L(t) provides the autonomous ordinary differential equation (ODE) for n along characteristic curves of x = L(t):

$$\frac{\mathrm{d}n_L}{\mathrm{d}t} = \Gamma(n_L) - n_L \Sigma(n_L),\tag{3.25}$$

where $n_L = n(L, t)$, so that if $r_m > r_a$, then $n_L \sim n_\infty$ for sufficiently large time,

where $\Gamma(n_{\infty}) - n_{\infty}\Sigma(n_{\infty}) = 0$. In subsequent large-time analysis, we may therefore replace the first boundary condition from (3.23) with

$$n = n_{\infty}$$
 or $\frac{\partial v_n}{\partial x} = \Sigma(n_{\infty})$ at $x = L(t)$. (3.26)

3.3 Numerical results

To illustrate the behaviour of the model from (3.20)–(3.23), we present and discuss some numerical solutions on the moving domain $0 \le x \le L(t)$.

3.3.1 Numerical methods

To obtain numerical solutions of (3.20)–(3.23), we fix the moving boundary by scaling x with L(t) as $\xi = x/L(t)$, so that $\xi \in [0, 1]$, and the model becomes

$$\frac{\partial n}{\partial t} = \frac{1}{L} \frac{\partial n}{\partial \xi} \left(\xi \frac{\mathrm{d}L}{\mathrm{d}t} - v_n \right) - \frac{n}{L} \frac{\partial v_n}{\partial \xi} + \Gamma(n), \tag{3.27}$$

$$\frac{1}{L^2} \frac{\partial}{\partial \xi} \left(n \frac{\partial v_n}{\partial \xi} \right) - \frac{1}{L} \frac{\partial}{\partial \xi} \left[n \Sigma(n) \right] - \kappa \frac{n v_n}{1 - n} = 0, \tag{3.28}$$

$$\frac{\mathrm{d}L(t)}{\mathrm{d}t} = v_n(1, t). \tag{3.29}$$

$$\frac{1}{L} \frac{\partial v_n}{\partial \xi} (1, t) = \Sigma(n) \Big|_{\xi = 1}, \quad v_n(0, t) = 0, \quad n(\xi, 0) = n_i(\xi), \quad L(0) = 1.$$
(3.30)

We spatially discretise (3.27) and (3.28) using finite differences. Upwind or downwind finite differences are used for the first term on the right-hand side of (3.27), the direction of which is determined by the sign of the quantity in the brackets. The equations from (3.27) and (3.29) are then numerically integrated in time using the function ode23s in MATLAB, which uses a third order Runge-Kutta method.

For spatial discretisation, we partition $\xi \in [0, 1]$ uniformly so that $\xi_i = i\Delta \xi$ for i = 0, ..., N, where $\Delta \xi = 1/N$ and N+1 is the number of spatial nodes. In

the discussion that follows, we denote $n_i(t) = n(\xi_i, t)$ and $v_i(t) = v_n(\xi_i, t)$ The finite difference scheme corresponding to (3.27), (3.29) and (3.30) for i = 0, ..., N are then given by

$$\frac{\partial n_{i}}{\partial t} = \left(\xi_{i}v_{N} - v_{i}\right) \cdot \frac{1}{L\Delta\xi} \begin{cases} n_{i+1} - n_{i} & \text{if } \xi_{i}v_{N} - v_{i} > 0 \text{ or } i = 0, \\ n_{i} - n_{i-1} & \text{if } \xi_{i}v_{N} - v_{i} < 0 \text{ or } i = N, \end{cases}$$

$$-\frac{n_{i}}{2L\Delta\xi} \cdot \begin{cases} 4v_{1} - v_{2} & \text{if } i = 0, \\ v_{i+1} - v_{i-1} & \text{if } i = 1, \dots, N - 1, \end{cases} + \Gamma(n_{i}),$$

$$v_{N-2} - 4v_{N-1} + 3v_{N} & \text{if } i = N,$$
(3.31)

$$\frac{\mathrm{d}L}{\mathrm{d}t} = v_N,\tag{3.32}$$

$$v_N = \frac{2\Delta \xi L \Sigma(n_N) + 4v_{N-1} - v_{N-2}}{3}, \qquad v_0 = 0.$$
(3.33)

The equations from (3.31) and (3.32) are then numerically integrated in time using the function ode23s in MATLAB, which uses a Runge-Kutta method.

Using central discretisations for both first- and second-order derivatives, the finite difference scheme corresponding to (3.28) for $i=2,\ldots,N-2$ is given by

$$\frac{n_i}{(L)^2} \cdot \frac{v_{i+1} - 2v_i + v_{i-1}}{(\Delta \xi)^2} + \frac{1}{(L)^2} \cdot \frac{n_{i+1} - n_{i-1}}{2\Delta \xi} \cdot \frac{v_{i+1} - v_{i-1}}{2\Delta \xi}
- \frac{1}{L} \cdot \frac{n_{i+1} - n_{i-1}}{2\Delta \xi} \cdot F(n_i) - \kappa \frac{n_i v_i}{(1 - n_i)} = 0.$$
(3.34)

This equation can be rearranged to give

$$A_i v_{i+1} + B_i v_i + C_i v_{i-1} + D_i = 0, (3.35)$$

where

$$A_{i} = \frac{4n_{i} + n_{i+1} - n_{i-1}}{4(L)^{2}(\Delta\xi)^{2}}, \qquad B_{i} = -\frac{2n_{i}}{(L)^{2}(\Delta\xi)^{2}} - \frac{\kappa n_{i}}{(1 - n_{i})},$$

$$C_{i} = \frac{4n_{i} - n_{i+1} + n_{i-1}}{4(L)^{2}(\Delta\xi)^{2}}, \qquad D_{i} = -\frac{n_{i+1} - n_{i-1}}{2S\Delta\xi}F(n_{i}).$$
(3.36)

The finite difference schemes corresponding to (3.28) for i = 1 and i = N - 1 are found by imposing the first two boundary conditions from (3.33) onto (3.35), and are given by

$$A_1 v_3 + B_1 v_2 + D_1 = 0, (3.37)$$

$$\underbrace{\left(\frac{4A_{N-1}}{3} + B_{N-1}\right)}_{=\Upsilon_{N-1}^{B}} v_{N-1} + \underbrace{\left(C_{N-1} - \frac{A_{N-1}}{3}\right)}_{=\Upsilon_{N-1}^{C}} v_{N-2} + \underbrace{\frac{2A_{N-1}L\Delta\xi\Sigma(n_{N})}{3} + D_{N-1}}_{=\Upsilon_{N-1}^{D}} = 0,$$
(3.38)

respectively. The solution to v_i is obtained by assembling (3.35), (3.37) and (3.38) into the matrix-vector form $\mathcal{M}\mathbf{v} = \mathbf{f}$, where $\mathbf{v} = (v_1, \ldots, v_i, \ldots, v_{N-1})^T$, $\mathbf{f} = -(D_1, \ldots, D_i, \ldots, \Upsilon_{N-1}^D)^T$, and \mathcal{M} is a tri-diagonal matrix of size $(N-2) \times (N-2)$ given by

$$\mathcal{M} = \begin{pmatrix} B_1 & A_1 & & & & & \\ C_2 & B_2 & A_2 & & & & & \\ & \ddots & \ddots & \ddots & & & & \\ & & C_i & B_i & A_i & & & & \\ & & \ddots & \ddots & \ddots & & \\ & & & C_{N-2} & B_{N-2} & A_{N-2} & \\ & & & & \Upsilon_{N-1}^C & \Upsilon_{N-1}^B \end{pmatrix} . \tag{3.39}$$

The vector \mathbf{v} is found by computing $\mathbf{v} = \mathcal{M}^{-1}\mathbf{f}$. The Thomas algorithm is used to compute \mathcal{M}^{-1} since \mathcal{M} is tri-diagonal, via the built-in function tridiag.

3.3.2 Results

In this subsection we fix $r_m = 0.3$, $r_a = 0.2$ and $\kappa = 100$, and pay particular attention to three exemplar values of ϕ that generate patterned and forward- and

backward-moving travelling-wave solutions. Since the tumour is nutrient-rich and all cells are adequately nourished, we take n to be near-uniform when t=0, and adopt the initial conditions $n_i(x) = \frac{1}{3} + 0.05 \sin(15\pi x)$. This also accounts for small fluctuations in the cell density across the tumour. We note that the choice of $n_i(0) = \frac{1}{3}$ arises from the far-field value of n in travelling-wave coordinates as considered in Section 3.4, and is chosen here for convenience.

In Fig. 3.1(a, b), we present n and v_n when $\phi = 0.2$, where we observe forward-moving travelling waves and linear growth in L, after an initial period of transient growth from the initial cell distribution. In contrast, Fig. 3.1(c, d) illustrate n and v_n when $\phi = 0.5$, where we observe backward-moving travelling waves and linear recession in L. As the tumour vanishes, the position of the tumour edge decays exponentially towards zero, as shown in Fig. 3.1(d). Notably, the case in which $\phi = 0.2$ corresponds to tumour growth, whereas $\phi = 0.5$ corresponds to the retreat and eventual extinction of the tumour. This motivates a travelling-wave analysis of the PDE model (3.20)–(3.23) which is provided in Section 3.4, where we express the speed of the tumour edge in terms of the model parameters and obtain explicit criteria for whether the wave grows or retreats.

In Fig. 3.1(e, f), we present n and v_n when $\phi = 0.85$. After a period of transient growth from the initial data, n(x, t) exhibits a patterned solution comprising multiple regions of high density (shown in yellow), which we term cell peaks. These peaks are sharply separated by regions of low cell density (shown in blue). The maximal volume fraction of all cell peaks is approximately equal to n(L, t), where from (3.25) we have $n(L, t) \sim n_{\infty}$ for $t \gg 1$. As highlighted by the velocity profiles, cells in low density regions migrate up gradients of n toward regions of high cell density, due to attractive forces experienced between them when $\Sigma(n) < 0$. This attraction results in the contraction of the tumour, and consequently the eventual extinction of the tumour. Nevertheless, the patterned solutions observed prior to extinction retain a degree of biological relevance. For example, and as described in a similar multiphase model of tissue growth (Green et al., 2009b), the inherent structural

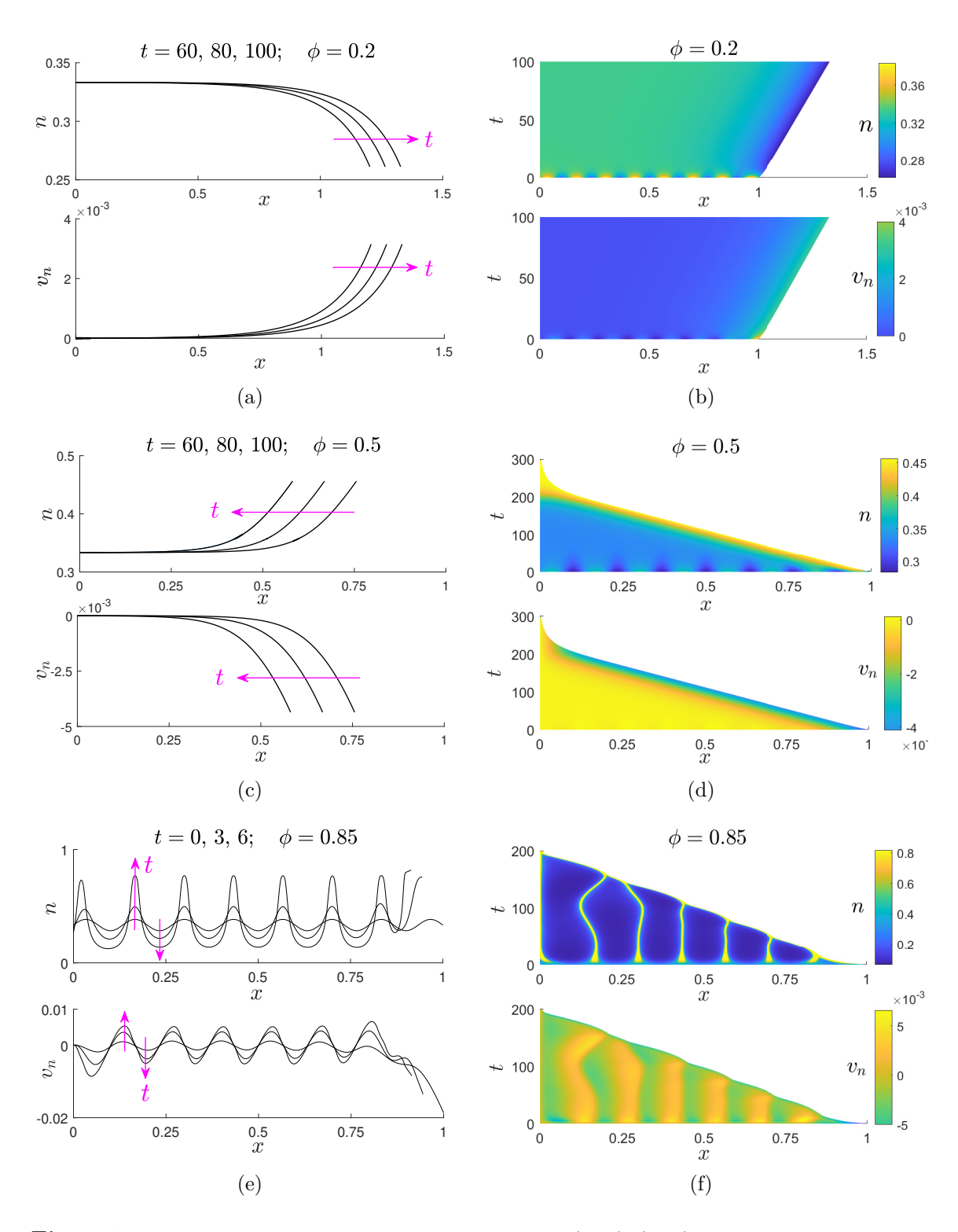


Figure 3.1: Numerical solutions of the PDE system from (3.20)-(3.23) for three values of ϕ . The black lines in (a, c, e) represent n(x, t) at indicated fixed times, while the colour maps in (b, d, f) represent n(x, t) across a temporal interval. The pink arrows point in the direction of increasing time. Parameter values: $r_m = 0.3$, $r_a = 0.2$, $\kappa = 100$ and $\phi = 0.2$ (a, b), $\phi = 0.5$ (c, d) and $\phi = 0.85$ (e, f).

instability of a suspension of *in vitro* tumour cells with a spatially-patterned structure could lead to its break-up, and consequently the formation of separate tumour spheroids. Parameter regimes in which we expect pattern formation, that could be indicative of break-up, are presented in Section 3.4 by determining the instability of travelling-wave solutions.

3.4 Travelling-wave solutions and stability analysis

In this section, we use travelling-wave analysis to obtain the speed at which the tumour either advances or retreats in terms of the model parameters. We also present regions of parameter space in which travelling-wave solutions are linearly unstable in t, which indicate when patterned solutions are expected.

3.4.1 Formulation

We write the PDE system from (3.20)–(3.23) in terms of the variable $L(t) = \overline{L}(t)/\sqrt{\kappa}$ and coordinate $z = \sqrt{\kappa}x - \overline{L}(t)$, where $\overline{L} \sim ct$ and $z \in (-\infty, 0]$. Here, c is the scaled wave speed, i.e. the speed of travelling waves observed in a simulation of (3.20)–(3.23) is $c/\sqrt{\kappa}$. Setting $n \equiv n(z, t)$ and $v_n \equiv v(z, t)/\sqrt{\kappa}$, we obtain

$$\frac{\partial n}{\partial t} - \frac{\partial n}{\partial z} \frac{d\overline{L}}{dt} + \frac{\partial}{\partial z} (nv) = \Gamma(n) \qquad -\infty < z \le 0, \tag{3.40}$$

$$\frac{\partial}{\partial z} \left(n \frac{\partial v}{\partial z} \right) - \frac{\partial}{\partial z} [n \Sigma(n)] - \frac{nv}{1 - n} = 0 \qquad -\infty < z \le 0, \tag{3.41}$$

$$\frac{\mathrm{d}\overline{L}(t)}{\mathrm{d}t} = v(0, t), \qquad n(0, t) = n_{\infty}, \qquad \frac{\partial}{\partial z}v(0, t) = \Sigma(n_{\infty}), \qquad \lim_{z \to -\infty} v(z, t) = 0.$$
(3.42)

We note that since κ does not appear in (3.40)–(3.42), the value of the cell-liquid drag does not determine the stability or direction of travelling waves.

3.4.2 Determining the stability of travelling waves

To determine the stability of travelling waves, we introduce the perturbations

$$n(z, t) \sim N(z) + n_1(z, t), \quad v_n(z, t) \sim V(z) + v_1(z, t), \quad \overline{L}(t) \sim ct + L_1(t), \quad (3.43)$$

where $|n_1|$, $|v_1|$, $|L_1| \ll 1$, so that to leading order, (3.40)–(3.42) provide the system of travelling-wave ODEs

$$-c\frac{\mathrm{d}N}{\mathrm{d}z} + \frac{\mathrm{d}}{\mathrm{d}z}(NV) = \Gamma(N),\tag{3.44}$$

$$\frac{\mathrm{d}}{\mathrm{d}z} \left(N \frac{\mathrm{d}V}{\mathrm{d}z} \right) - \frac{\mathrm{d}}{\mathrm{d}z} \left[N \Sigma(N) \right] - \frac{NV}{1 - N} = 0, \tag{3.45}$$

$$V(0) = c,$$
 $N(0) = n_{\infty},$ $\frac{\mathrm{d}}{\mathrm{d}z}V(0) = \Sigma(n_{\infty}),$ $\lim_{z \to -\infty} V(z) = 0.$ (3.46)

Details of the numerical methods employed to find approximations of N(z), V(z) and c, are presented shortly in subsection 3.4.3. In view of the perturbations from (3.43), the system (3.40)–(3.42) provides the linearised problem

$$\frac{\partial n_1}{\partial t} - c \frac{\partial n_1}{\partial z} - \frac{dN}{dz} \frac{dL_1}{dt} + \frac{\partial}{\partial z} (Nv_1 + Vn_1) = G(N)n_1, \tag{3.47}$$

$$\frac{\partial}{\partial z} \left(\frac{\mathrm{d}V}{\mathrm{d}z} n_1 + N \frac{\partial v_1}{\partial z} \right) - H(N) \frac{\mathrm{d}N}{\mathrm{d}z} n_1 - F(N) \frac{\partial n_1}{\partial z} - \frac{n_1 V}{(1 - N)^2} - \frac{N v_1}{1 - N} = 0, \quad (3.48)$$

$$\frac{\mathrm{d}L_1(t)}{\mathrm{d}t} = v_1(0, t), \qquad n_1(0, t) = 0, \qquad \frac{\partial}{\partial z}v_1(0, t) = 0, \qquad \lim_{z \to -\infty} v_1(z, t) = 0.$$
(3.49)

Here, $G(n) = \frac{d}{dn}\Gamma(n)$, $F(n) = \frac{d}{dn}\left[n\Sigma(n)\right]$ and $H(n) = \frac{d}{dn}F(n)$, where $\Gamma(n)$ and $\Sigma(n)$ are stated in (3.9) and (3.10), respectively.

To determine whether the perturbations n_1 , v_1 and L_1 grow or decay with t, we set

$$n_1(z, t) = \eta(z)e^{\lambda t}, \qquad v_1(z, t) = \beta(z)e^{\lambda t}, \qquad L_1(t) = \ell e^{\lambda t},$$
 (3.50)

where ℓ is a constant and λ is the growth rate. If $\Re(\lambda) > 0$ or $\Re(\lambda) < 0$, then the solution triple (N, V, c) is unstable or stable in t, respectively. Substituting (3.50)

into (3.47)–(3.49), we obtain the autonomous system of ODEs

$$\lambda \eta - \ell \lambda N' - c \eta' + N \beta' + N' \beta + V' \eta + V \eta' = G(N) \eta, \tag{3.51}$$

$$V''\eta + V'\eta' + N\beta'' + N'\beta' - H(N)N'\eta - F(N)\eta' - \frac{V\eta}{(1-N)^2} - \frac{N\beta}{1-N} = 0,$$
(3.52)

$$\beta(0) = \ell \lambda, \qquad \eta(0) = 0, \qquad \beta'(0) = 0, \qquad \lim_{z \to -\infty} \beta(z) = 0,$$
 (3.53)

where $' \equiv \frac{\mathrm{d}}{\mathrm{d}z}$. To obtain λ , we discretise (3.51)–(3.53) using finite differences and assemble the resulting linear system into an eigenvalue problem for λ . Using the function eig in MATLAB, we obtain the corresponding set of eigenvalues and isolate the pair with the largest real part, $\Lambda = \max \left[\Re(\lambda)\right]$. If $\Lambda > 0$, travelling-wave solutions are unstable in t, then (3.20)–(3.23) may exhibit patterned solutions. If $\Lambda < 0$, we expect (3.20)–(3.23) to exhibit stable travelling-wave solutions. Details of the numerical methods employed to obtain the value of Λ are described in the following subsection.

Before presenting the results relating to the travelling-wave speed and criteria for pattern formation, we present the numerical methods employed to solve the travelling-wave ODEs from (3.44)–(3.46) as well as the eigenvalue problem from (3.51)–(3.53).

3.4.3 Numerical methods for the travelling-wave ODEs, equations (3.44)–(3.46)

In this section, we present the numerical methods used to determine N(z), V(z) and c from (3.44)–(3.46).

Formulation

For numerical purposes, we express (3.44)–(3.46) as a system of three, first order ODEs by introducing the variables U(z) = V'(z) where $' \equiv d/dz$. We obtain

$$N'(z) = \frac{\Gamma(N) - NU}{V - c},\tag{3.54}$$

$$V'(z) = U, (3.55)$$

$$U'(z) = \frac{V}{1 - N} + \frac{(F(N) - U)(\Gamma(N) - NU)}{N(V - c)},$$
(3.56)

$$V(0) = c,$$
 $N(0) = n_{\infty},$ $U(0) = \Sigma(n_{\infty}),$ $\lim_{z \to -\infty} N(z) = \alpha,$ (3.57)

where $\alpha = 1 - r_a/r_m$. The fourth from (3.57) is obtained by combining the conditions $\lim_{z \to -\infty} V(z) = 0$ and $\lim_{z \to -\infty} \frac{\mathrm{d}^N}{\mathrm{d}z} = 0$ (the latter being necessary for a travelling-wave solution to exist) with (3.44) to provide $\Gamma(N) \to 0$ as $z \to -\infty$. The system from (3.54)–(3.57) is computationally singular at z = 0 because of the boundary condition V(0) = c and the right-hand side of (3.54) and (3.56). In view of this, we consider the leading edge of the wavefront to be $z = -\delta$ where δ is sufficiently small such that the solution converges. We numerically integrate (3.54)–(3.57) on $z \in [-Z, -\delta]$ in MATLAB using the function bvp5c which uses a fifth-order, implicit Runge-Kutta method.

We impose the boundary conditions from (3.57) as $z \to -\infty$ at z = -Z, where Z is sufficiently large such that the solution converges. The Taylor expansions of N(z) and V(z) around z = 0

$$N(z) \sim n_{\infty} + N'(0)z$$
, $V(z) \sim c + \Sigma(n_{\infty})z$, $U(z) \sim \Sigma(n_{\infty}) + U'(0)z$ (3.58)

are used as boundary conditions at $z = -\delta$. The values of N'(0) and U'(0) are found

by combining (3.54) and (3.57) at z = 0 and employing L'Hôpital's rule, so that

$$N'(0) = \frac{n_{\infty}c}{(F(n_{\infty}) + \Sigma(n_{\infty}) - \Gamma_N)(n_{\infty} - 1)},$$
(3.59)

$$U'(0) = \frac{c[\Gamma_N - 2\Sigma(n_\infty)]}{(F(n_\infty) + \Sigma(n_\infty) - \Gamma_N)(n_\infty - 1)},$$
(3.60)

where $\Gamma_N = \frac{\mathrm{d}}{\mathrm{d}n}\Gamma(n_\infty)$. The unknown value of c is obtained as an eigenvalue in bvp5c.

Slow wave speed ($|c| \ll 1$) asymptotic analysis

The function bvp5c requires an initial approximation of the solutions N, V and c satisfying (3.54)–(3.57) in order to converge. For this, we use asymptotic solutions valid when $|\alpha - n_{\infty}| \ll 1$. When $|\alpha - n_{\infty}| \ll 1$, then $|c| \ll 1$, and we linearise N and V around their far-field values, $\lim_{z \to -\infty} N(z) = \alpha$ and $\lim_{z \to -\infty} V(z) = 0$. Following Lemon and King (2007a), we introduce the perturbations

$$N \sim \alpha + \varepsilon N_1, \qquad V \sim \varepsilon V_0, \qquad c \sim \varepsilon c_0,$$
 (3.61)

where $|\varepsilon| = |\alpha - n_{\infty}| \ll 1$ and $(N_1, V_0, c_0) = \mathcal{O}(1)$. The perturbations N_1 and V_0 satisfy

$$\alpha \frac{\mathrm{d}V_0}{\mathrm{d}z} = G(\alpha)N_1,\tag{3.62}$$

$$\alpha \frac{\mathrm{d}^2 V_0}{\mathrm{d}z^2} - \frac{\mathrm{d}N_1}{\mathrm{d}z} F(\alpha) - \frac{\alpha V_0}{1 - \alpha} = 0, \tag{3.63}$$

$$\lim_{z \to -\infty} V_0(z) = 0, \qquad \lim_{z \to -\infty} N_1(z) = 0, \qquad N_1(0) = -1, \qquad V_0(0) = c_0. \tag{3.64}$$

where $G(n) = \frac{d}{dn}\Gamma(n)$ and $F(n) = \frac{d}{dn}\left[n\Sigma(n)\right]$. Combining (3.62) and (3.63) provides

$$\gamma \frac{\mathrm{d}^2 V_0}{\mathrm{d}z^2} - V_0 = 0, \quad \text{where} \quad \gamma = \frac{1 - \alpha}{G(\alpha)} [G(\alpha) - F(\alpha)],$$
(3.65)

so that

$$N_1 = -e^{z/\sqrt{\gamma}}, \qquad V_0 = k_m \sqrt{\gamma} e^{z/\sqrt{\gamma}}, \qquad c_0 = k_m \sqrt{\gamma}. \tag{3.66}$$

These asymptotic solutions are used as initial guesses of N, V and c from (3.54)—(3.57). For more general parameter values, such as those presented in Fig. 3.4(a),

the method of parameter continuation is used.

Numerical methods for the eigenvalue problem, equa-3.4.4 tions (3.51)–(3.53)

In this section, we present the numerical methods used to determine the set of discrete eigenvalues λ associated with the linear system from (3.51)–(3.53). As stated above, to obtain λ , we discretise (3.51)–(3.53) using finite differences and assemble the resulting linear system into an eigenvalue problem for λ . From this, we isolate the pair of eigenvalues with the largest real part, $\Lambda = \max |\Re(\lambda)|$.

We partition the truncated domain $z \in [-Z, 0]$ uniformly, so that $z_j = -Z +$ $j\Delta z$ for $j=0,\ldots,K$, where $\Delta z=Z/K$ denotes the grid spacing and K+1 is the number of nodes. We denote the travelling-wave solutions (obtained using the methods described in section 3.4.3) by $N_j = N(z_j)$ and $V_j = V(z_j)$, and the unknown perturbations by $\eta_j = \eta(z_j)$ and $\beta_j = \beta(z_j)$. We note that the approximations of N(z) and V(z) are obtained on a non-uniform grid via byp5c as described in section 3.4.3, and are interpolated to be compatible with the uniform grid used in this section. To simplify the notation of the discrete eigenvalue problem, we introduce the notation

$$N'_{j} := \frac{\mathrm{d}}{\mathrm{d}z} N(z_{j}) \approx \frac{1}{2\Delta z} \begin{cases} -3N_{0} + 4N_{1} - N_{2} & \text{if} \quad j = 0, \\ N_{j+1} - N_{j-1} & \text{if} \quad j = 1, \dots, K - 1, \\ N_{K-2} - 4N_{K-1} + 3N_{K} & \text{if} \quad j = K, \end{cases}$$

$$V'_{j} := \frac{\mathrm{d}}{\mathrm{d}z} V(z_{j}) \approx \frac{1}{2\Delta z} \begin{cases} -3V_{0} + 4V_{1} - V_{2} & \text{if} \quad j = 0, \\ V_{j+1} - V_{j-1} & \text{if} \quad j = 1, \dots, K - 1, \\ V_{K-2} - 4V_{K-1} + 3V_{K} & \text{if} \quad j = K. \end{cases}$$
(3.68)

$$V_{j}' := \frac{\mathrm{d}}{\mathrm{d}z} V(z_{j}) \approx \frac{1}{2\Delta z} \begin{cases} -3V_{0} + 4V_{1} - V_{2} & \text{if } j = 0, \\ V_{j+1} - V_{j-1} & \text{if } j = 1, \dots, K - 1, \\ V_{K-2} - 4V_{K-1} + 3V_{K} & \text{if } j = K. \end{cases}$$
(3.68)

The notation N_j' and V_j' will be used in place of the explicit finite difference quotients

stated in (3.67) and (3.68).

We discretise the derivatives of $\eta(z)$ and $\beta(z)$ using central finite differences. The boundary conditions from (3.53) become

$$\beta_K = \ell \lambda, \qquad \eta_K = 0, \qquad \beta_K = \frac{4\beta_{K-1} - \beta_{K-2}}{3}, \qquad \beta_0 = 0.$$
 (3.69)

Using the first and third of (3.69), the constant ℓ can be removed from the second term of (3.51) by writing $\ell\lambda = (4\beta_{K-1} - \beta_{K-2})/3$. The finite difference scheme corresponding to (3.51)–(3.52) for j = 2, ..., K-2 is given by

$$\lambda \eta_{j} = A_{j}^{1} \eta_{j+1} + A_{j}^{0} \eta_{j} + A_{j}^{-1} \eta_{j-1} + B_{j}^{1} \beta_{j+1} + B_{j}^{0} \beta_{j} + B_{j}^{-1} \beta_{j-1} + \frac{N_{j}'}{3} (4\beta_{K-1} - \beta_{K-2}),$$
(3.70)

$$P_j^1 \eta_{j+1} + P_j^0 \eta_j + P_j^{-1} \eta_{j-1} + Q_j^1 \beta_{j+1} + Q_j^0 \beta_j + Q_j^{-1} \beta_{j-1} = 0,$$
(3.71)

such that

$$\begin{split} A_j^1 &= \frac{c - V^j}{2\Delta z}, \quad A_j^0 = G(N^j) - V_j^{'}, \quad A_j^{-1} = \frac{V_j - c}{2\Delta z}, \\ B_j^1 &= -\frac{N_j}{2\Delta z}, \quad B_j^0 = -N_j^{'}, \quad B_j^{-1} = \frac{N_j}{2\Delta z}, \\ P_j^1 &= \frac{V_j^{'}}{2\Delta z} - \frac{F(N_j)}{2\Delta z}, \quad P_j^0 = V_j^{''} - H(N_j)N_j^{'} - \frac{V_j}{1 - N_j}, \quad P_j^{-1} = -\frac{V_j^{'}}{2\Delta z} + \frac{F(N_j)}{2\Delta z}, \\ Q_j^1 &= \frac{N_j}{(\Delta z)^2} + \frac{N_j^{'}}{2\Delta z}, \quad Q_j^0 = -\frac{2N_j}{(\Delta z)^2} - \frac{N_j}{1 - N_i}, \quad Q_j^{-1} = \frac{N_j}{(\Delta z)^2} - \frac{N_j^{'}}{2\Delta z}. \end{split}$$

By combining (3.70) and the boundary conditions from (3.69), the finite difference schemes corresponding to (3.51) for j = 1 and j = K - 1 are given by

$$\lambda \eta_{1} = A_{1}^{1} \eta_{2} + A_{1}^{0} \eta_{1} + B_{1}^{1} \beta_{2} + B_{1}^{0} \beta_{1} + \frac{N_{1}'}{3} \left(4\beta_{K-1} - \beta_{K-2} \right), \tag{3.72}$$

$$\lambda \eta_{K-1} = A_{K-1}^{0} \eta_{K-1} + A_{K-1}^{-1} \eta_{K-2}$$

$$+ \underbrace{\left(B_{K-1}^{0} + \frac{4B_{K-1}^{1}}{3} + \frac{4N_{K-1}'}{3} \right)}_{= \Upsilon_{K-1}^{0}} \beta_{K-1} + \underbrace{\left(B_{K-1}^{-1} - \frac{B_{K-1}^{1}}{3} - \frac{N_{K-1}'}{3} \right)}_{= \Upsilon_{K-1}^{-1}} \beta_{K-2}, \tag{3.73}$$

respectively. The finite difference schemes corresponding to (3.52) for j=1 and j=K-1 are

$$P_1^1 \eta_2 + P_1^0 \eta_1 + Q_1^1 \beta_2 + Q_1^0 \beta_1 = 0, (3.74)$$

$$P_{K-1}^{0}\eta_{K-1} + P_{K-1}^{-1}\eta_{K-2} + \underbrace{\left(Q_{K-1}^{0} + \frac{4Q_{K-1}^{1}}{3}\right)}_{=\Theta_{K-1}^{0}} \beta_{K-1} + \underbrace{\left(Q_{K-1}^{-1} - \frac{Q_{K-1}^{1}}{3}\right)}_{=\Theta^{-1}\beta_{K-1}} \beta_{K-2} (3.75)$$

We assemble (3.70), (3.71) and (3.72)–(3.75) into the generalised eigenvalue problem

$$\lambda \mathbf{Y}_1 \mathbf{f} = \mathbf{Y}_2 \mathbf{f} \tag{3.76}$$

where $\mathbf{f} = (\eta_1, ..., \eta_j, ..., \eta_{K-1}, \beta_1, ..., \beta_j, ..., \beta_{K-1})^T$ and

$$\mathbf{Y}_{1} = \begin{pmatrix} \mathbf{I} & \mathbf{0} \\ \mathbf{0} & \mathbf{0} \end{pmatrix}^{2(K-2)\times 2(K-2)}, \qquad \mathbf{Y}_{2} = \begin{pmatrix} \mathbf{A} & \mathbf{B} \\ \mathbf{P} & \mathbf{Q} \end{pmatrix}^{2(K-2)\times 2(K-2)}. \tag{3.77}$$

Here, the sub-matrices $\mathbf{0}$ and \mathbf{I} are the zero- and identity matrices of size $(K-2) \times (K-2)$ respectively. The sub-matrices \mathbf{A} , \mathbf{B} , \mathbf{P} , \mathbf{Q} are given by

$$\mathbf{A} = \begin{pmatrix} A_1^0 & A_1^1 & & & & & \\ A_2^{-1} & A_2^0 & A_2^1 & & & & \\ & \ddots & \ddots & \ddots & & & \\ & & A_j^{-1} & A_j^0 & A_j^1 & & & & \\ & & \ddots & \ddots & \ddots & & \\ & & & A_{K-2}^{-1} & A_{K-2}^0 & A_{K-2}^1 & \\ & & & & A_{K-1}^{-1} & A_{K-1}^0 \end{pmatrix}, \tag{3.78}$$

$$\boldsymbol{B} = \begin{pmatrix} B_{1}^{0} & B_{1}^{1} & & -\frac{N_{1}^{\prime}}{3} & \frac{4N_{1}^{\prime}}{3} \\ B_{2}^{-1} & B_{2}^{0} & B_{2}^{1} & & -\frac{N_{2}^{\prime}}{3} & \frac{4N_{2}^{\prime}}{3} \\ & \ddots & \ddots & \ddots & \vdots & \vdots \\ & B_{j}^{-1} & B_{j}^{0} & B_{j}^{1} & -\frac{N_{j}^{\prime}}{3} & \frac{4N_{j}^{\prime}}{3} \\ & & \ddots & \ddots & \ddots & \vdots & \vdots \\ & & B_{K-2}^{-1} & B_{K-2}^{0} & \frac{N_{K-2}^{\prime}}{3} & B_{K-2}^{1} + \frac{4N_{K-2}^{\prime}}{3} \\ & & & & \Upsilon_{K-1}^{-1} & \Upsilon_{K-1}^{0} \end{pmatrix}$$

$$\boldsymbol{P} = \begin{pmatrix} P_{1}^{0} & P_{1}^{1} & & & & \\ P_{2}^{-1} & P_{2}^{0} & P_{2}^{1} & & & & \\ & & & P_{j}^{-1} & P_{j}^{0} & P_{j}^{1} & & & \\ & & & & & P_{K-2}^{-1} & P_{K-2}^{0} & P_{K-2}^{1} \\ & & & & & & P_{K-1}^{-1} & P_{K-1}^{0} \end{pmatrix}$$

$$\boldsymbol{Q} = \begin{pmatrix} Q_{1}^{0} & Q_{1}^{1} & & & & \\ Q_{2}^{-1} & Q_{2}^{0} & Q_{2}^{1} & & & & \\ & & & \ddots & \ddots & \ddots & \\ & & & & Q_{K-2}^{-1} & Q_{K-2}^{0} & Q_{K-2}^{1} \\ & & & & \ddots & \ddots & \ddots & \\ & & & & & Q_{K-1}^{-1} & Q_{K-1}^{0} & Q_{K-1}^{1} \\ & & & & & & Q_{K-1}^{-1} & \Theta_{K-1}^{0} \end{pmatrix}$$

$$(3.81)$$

We obtain the discrete set of eigenvalues λ from the generalised eigenvalue problem (3.76) by using the function eig in MATLAB. From this, we isolate the pair of eigenvalues with the largest real part, $\Lambda = \max \left[\Re(\lambda)\right]$.

Before presenting results relating to the criteria for pattern formation, we now briefly illustrate the discrete eigenvalues obtained by solving the eigenvalue problem

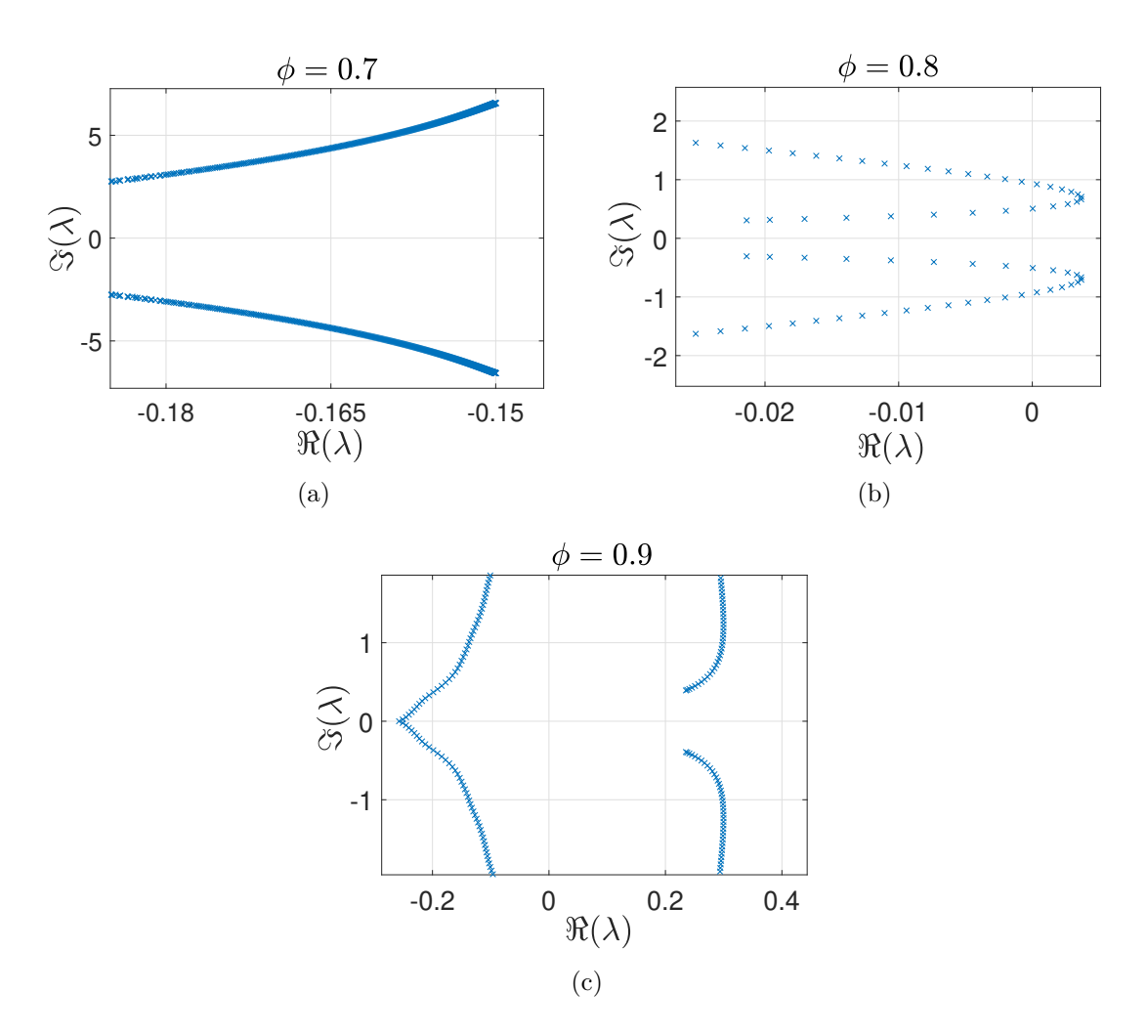


Figure 3.2: The discrete spectrum obtained from (3.76) illustrating the eigenvalues λ with the largest real part for $\phi = 0.7$ (a), $\phi = 0.8$ (b) and $\phi = 0.9$ (c). Parameter values: $r_m = 0.4$, $r_a = 0.2$, K = 1500 and Z = 15.

(3.76) on the truncated domain $z \in [-Z, 0]$ where Z = 15. In figure 3.2, we present the discrete spectrum obtained from (3.76), truncated to highlight the eigenvalues with the largest real-part for three different values of ϕ . As seen in figure 3.2(a), there are no eigenvalues such that $\Re(\lambda) > 0$ when $\phi = 0.7$, which indicates the PDE system from (3.20)–(3.23) will exhibit stable travelling-wave solutions. In contrast, figure 3.2(b,c) illustrates that there exists eigenvalues such that $\Re(\lambda) > 0$ when $\phi = 0.8$ and $\phi = 0.9$, indicating that the PDE system (3.20)–(3.23) can exhibit patterned solutions. In figure 3.3, we present the real-part of the three discrete eigenvalues with the largest real-part ($\lambda_1, \lambda_2, \lambda_3$) obtained from (3.76) as a function of the number of nodes and a fixed set of parameter values (see caption). This figure illustrates that $\Re(\lambda_1, \lambda_2, \lambda_3)$ converge as the number of nodes increase.

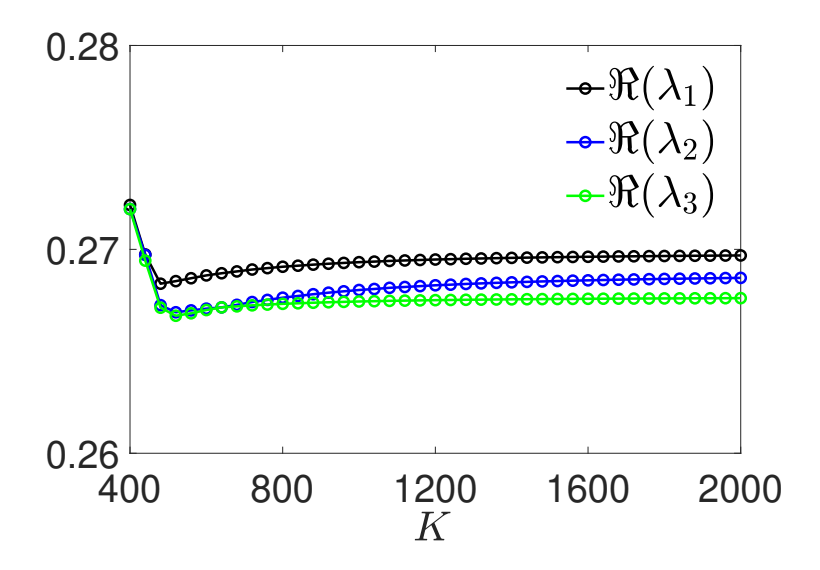


Figure 3.3: An illustration of the convergence of the three eigenvalues obtained from (3.76) with the largest real-part for $K \in [400, 2000]$. Parameter values: $r_m = 0.4$, $r_a = 0.2$, $\phi = 0.9$ and Z = 15.

3.4.5 Results

In this subsection, we present and discuss the criteria for pattern formation obtained from (3.51)–(3.53), as well as the travelling-wave speed obtained from (3.44)–(3.46). We first describe the results presented in Fig. 3.4(a). The solid black line represents the neutral stability curve $\Lambda=0$ obtained numerically from (3.51)–(3.53) as described above, for a fixed value of r_a . Regions in which travelling-wave solutions are unstable ($\Lambda>0$) or stable ($\Lambda<0$) are indicated. In Fig. 3.4(a), we also present the scaled wave speed c when travelling-wave solutions are stable, obtained numerically from (3.44)–(3.46), via the methods presented in subsection 3.4.3. The dashed black line represents the curve c=0, and regions in which the tumour advances (c>0) or retreats (c<0) are indicated. We recall that when travelling-wave solutions are stable, the wave speed, $c/\sqrt{\kappa}$, is the speed at which the tumour either advances or retreats.

To illustrate the accuracy of the stability regions shown in Fig. 3.4(a), we compare two numerical solutions of n(x, t) from the PDE system (3.20)–(3.23) that are marginally stable or unstable. In Fig. 3.4(a), the green and pink dots indicate two parameter regimes in which travelling-wave solutions are marginally un-

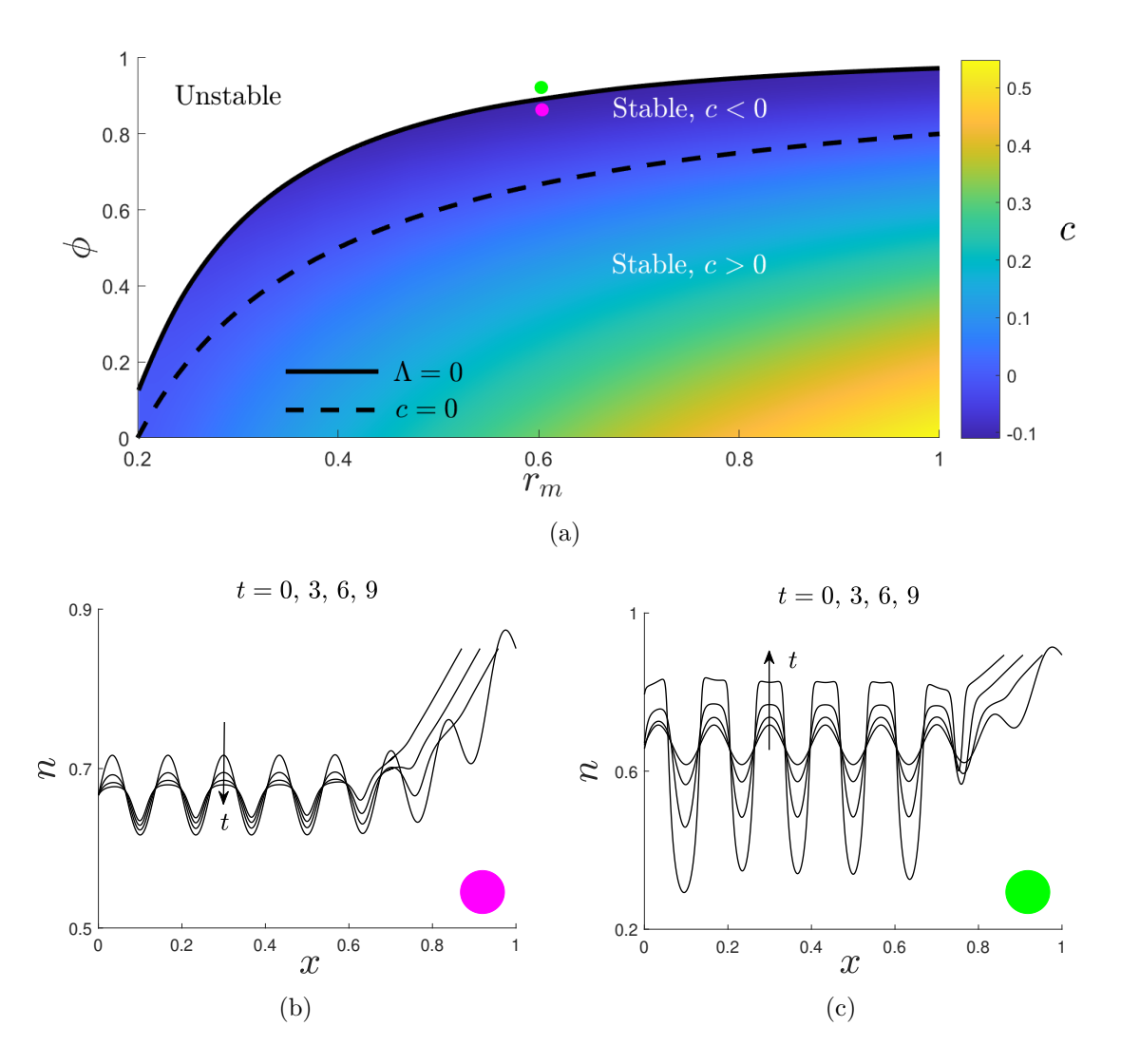


Figure 3.4: An analysis of travelling-wave solutions and their stability. In (a), the black solid line is the curve $\Lambda=0$ obtained numerically from (3.51)–(3.53). The black dashed line is the curve c=0. The colour map shows c, obtained numerically from (3.44)–(3.46). Parameter values for (a) are $0<\phi<1$, $0.2< r_m \le 1$ and $r_a=0.2$. In (b, c), we plot n(x,t) from the PDE system (3.20)–(3.23) for $\phi=0.87$ (pink dot) and $\phi=0.91$ (green dot) when t=0,3,6,9. Parameter values for (b, c) are $r_m=0.6$, $r_a=0.2$, $\kappa=50$. For both (b, c), we use $n_i(x)=N(x)+0.05\sin(15\pi x)$, where N(x) is the travelling-wave solution when t=0.

stable and stable, respectively. In Fig. 3.4(b), we present n(x, t) from (3.20)–(3.23) corresponding to these two parameter regimes at exemplar early time-points. For each parameter regime, we take the initial conditions to be a perturbation of the travelling-wave solution N obtained from (3.44)–(3.46), i.e.

$$n_i(x) = N(x) + 0.05\sin(15\pi x).$$
 (3.82)

When the marginally stable parameter regime (pink dot) is used, solutions decay from the initial perturbation toward a backward-moving travelling wave, similar to that shown in Fig. 3.1(c). As expected, solutions grow toward a pattern-forming solution from the initial perturbation when the marginally unstable parameter regime (green dot) is used. Hence, the results presented in Fig. 3.4(b) are consistent with the unstable and stable regions shown in Fig. 3.4(a), and illustrate a good level of accuracy of the neutral stability curve, $\Lambda = 0$.

As seen from the neutral stability curve $\Lambda = 0$ in Fig. 3.4(a), the value of ϕ required to destabilise travelling-wave solutions decreases with r_m . This suggests that patterns will form if there is insufficient cell growth to support the uniform migration of cells towards their natural packing density. Numerical solutions of the travelling-wave ODEs from (3.44)–(3.46) indicate that the sign of c corresponds to the sign of $\alpha - \phi$. This is consistent with the results in Fig. 3.4(b), as well as the slow-wave ($|c| \ll 1$) asymptotic analysis of (3.44)–(3.46) provided in section 3.4.3. When c > 0 (corresponding to when $\alpha > \phi$), we have $n > \phi$ behind the wavefront and cells are in a constant state of repulsion. Consequently, the tumour edge expands to provide space to which the cells can migrate. Conversely, when c < 0(corresponding to when $\alpha < \phi$), we have $n < \phi$ behind the wave-front and cells are in a constant state of attraction which results in the contraction of the tumour edge. Fig. 3.4(a) indicates that c is greatest when $r_m = 1$ and $\phi \to 0$. This suggests that the tumour grows quickest when the rate of cell production is large, but the cells' natural packing density is small (thereby increasing the strength of repulsive forces experienced between cells when $n > \phi$).

3.5 The stability of a spatially-uniform steady state

In contrast to the travelling-wave stability analysis presented in the previous section, we now determine the stability of the spatially-uniform steady state satisfying equations (3.20) and (3.21) on an infinite spatial domain. This stability analysis neglects the effects of the boundary conditions at the tumour edge, but has nevertheless been used informally in similar moving boundary models of tissue growth, e.g Lemon and

King (2007a) and Byrne et al. (2002). A comparison between this stability analysis and that from Section 3.4, where the effects of the moving boundary are incorporated, allows us to identify whether the moving boundary at the tumour edge affects the onset of pattern formation.

The non-trivial, spatially-uniform steady state of (3.20) and (3.21) is given by

$$(n, v_n) = (\alpha, 0),$$
 (3.83)

where $\alpha = (r_m - r_a)/r_m$. We introduce the linearisation $n \sim \alpha + n_p(x, t)$ and $v_n \sim v_p(x, t)$, where $|n_p|, |v_p| \ll 1$ satisfy the linearised problem

$$\frac{\partial n_p}{\partial t} + \alpha \frac{\partial v_p}{\partial x} - n_p G(\alpha) = 0, \qquad (3.84)$$

$$\alpha \frac{\partial^2 v_p}{\partial x^2} - \frac{\partial n_p}{\partial x} F(\alpha) - \frac{\kappa \alpha v_p}{1 - \alpha} = 0, \tag{3.85}$$

where $G(n) = \frac{\mathrm{d}}{\mathrm{d}n}\Gamma(n)$ and $F(n) = \frac{\mathrm{d}}{\mathrm{d}n}\left[n\Sigma(n)\right]$. To determine whether the perturbations n_p and v_p grow or decay in t, we set $(n_p, v_p) \propto e^{i\gamma x + \rho t}$ where γ is the perturbation wave number and ρ is the growth rate. Substituting this ansatz into (3.84) and (3.85), we obtain the dispersion relation

$$\rho(\gamma) = G(\alpha) - \frac{(1-\alpha)F(\alpha)}{1-\alpha + \kappa \gamma^{-2}}.$$
(3.86)

If $\rho > 0$ or $\rho < 0$, then the steady state from (3.83) is unstable or stable, respectively. As such, it is useful to consider the quantity

$$\rho_{\infty} := \lim_{\gamma \to \infty} \rho = G(\alpha) - F(\alpha). \tag{3.87}$$

If $\rho_{\infty} > 0$, then $\rho(\gamma)$ is monotonically increasing and since $\rho(0) < 0$, we have $\rho(\gamma) > 0$ for a sufficiently large value of γ . If $\rho_{\infty} < 0$, then $\rho(\gamma)$ is monotonically decreasing so that $\rho(\gamma) < 0$. Therefore, the steady state from (3.83) is unstable or stable when $\rho_{\infty} > 0$ or $\rho_{\infty} < 0$, respectively. In Fig. 3.5(a), we illustrate the function $\rho(\gamma)$ for two different parameter regimes that are provided in the caption, and which give rise to the cases $\rho_{\infty} > 0$ and $\rho_{\infty} < 0$.

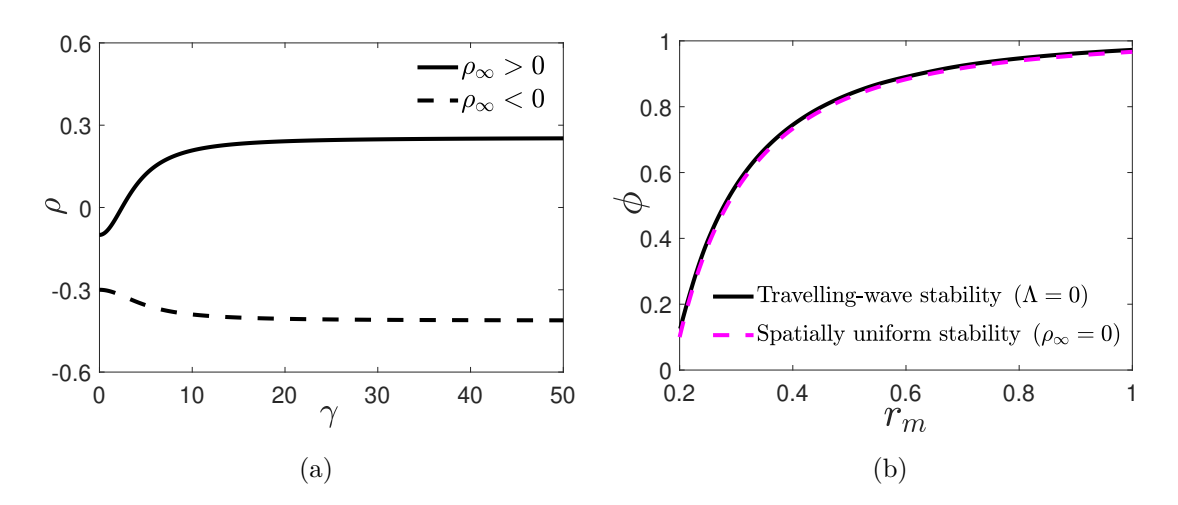


Figure 3.5: A stability analysis of the spatially-uniform steady state $(n, v_n) = (\alpha, 0)$. In (a), the solid black line is the function $\rho(\gamma)$ from (3.86) for $r_m = 0.3$, $r_a = 0.2$ and $\phi = 0.7$, whilst the dashed black line is $\rho(\gamma)$ for $r_m = 0.5$, $r_a = 0.2$ and $\phi = 0.7$. In (b), the solid black line is the curve $\Lambda = 0$ obtained numerically from (3.51)–(3.53), whilst the dashed pink line in is the curve $\rho_{\infty} = 0$, both with $r_a = 0.2$.

We now compare the stability analysis presented in this section with that from Section 3.4. In Fig. 3.5(b), we compare the neutral travelling-wave stability curve $\Lambda=0$ obtained numerically from (3.51)–(3.53) with the neutral stability curve of the spatially-uniform steady-state $\rho_{\infty}=0$ obtained in this section. As seen in Fig. 3.5(b), these two approaches to computing the respective neutral stability curves are in good agreement. This suggests that the values of cell production, cell death and the natural packing density largely determine the emergence of patterned solutions, in contrast to the inclusion or exclusion of the moving boundary. We therefore expect the destabilising mechanism giving rise to patterned solutions to be the attractive forces experienced by cells occurring when $n < \phi$. The good agreement between the curves presented in Fig. 3.5(b) justifies using the simpler analysis described in this section to determine criteria for spatial patterning, rather than the more computationally exhaustive analysis described in Section 3.4.

The close agreement between the neutral stability curves presented in Fig. 3.5(b) allows us to exploit the relation from (3.83) to deduce how the model parameters affect the onset of pattern formation. The parameter regime in which (3.83) is unstable, and hence patterned solutions are expected, can be found explicitly from

 $p_{\infty} > 0$, i.e.

$$\phi > 1 + \frac{r_a^2(r_m - 2)}{r_m(r_a + r_m)}. (3.88)$$

Since $0 < \phi < 1$, (3.88) indicates that solutions will not exhibit pattern formation when $r_m \geq 2$. This indicates that a high cell proliferation rate alone can curtail the formation of patterned solutions, regardless of the strength of attractive forces experienced between cells. Furthermore, (3.88) suggests that no patterns will form if there is a negligible rate of cell death. We also note that (3.88) is independent of κ , this being consistent with the analysis from Section 3.4, which indicated that the value of the cell-liquid drag does not determine whether solutions will exhibit pattern formation.

3.6 Qualitative analysis of pattern formation

In this section, we examine the qualitative features of patterned solutions like those shown in Fig. 3.1(f), which are formed by multiple regions of high cell density (termed cell peaks), separated by regions of low cell density. As discussed in Section 3.3, the inherent structural instability of a suspension of *in vitro* tumour cells with a patterned structure could lead to its break-up, and consequently the formation of separate tumour spheroids. Whilst tumour break-up is not explicitly modelled here, a qualitative analysis of patterned solutions nonetheless provides insight into how the value of model parameters could affect the onset of such a process.

3.6.1 Mathematical formulation

In this subsection, we define the metrics used to quantify the number and width of cell peaks. We define the number of cell peaks $\beta(t)$, to be the number of intervals within $x \in [0, L(t)]$ such that n(x, t) is greater than a threshold \mathcal{V} . The set

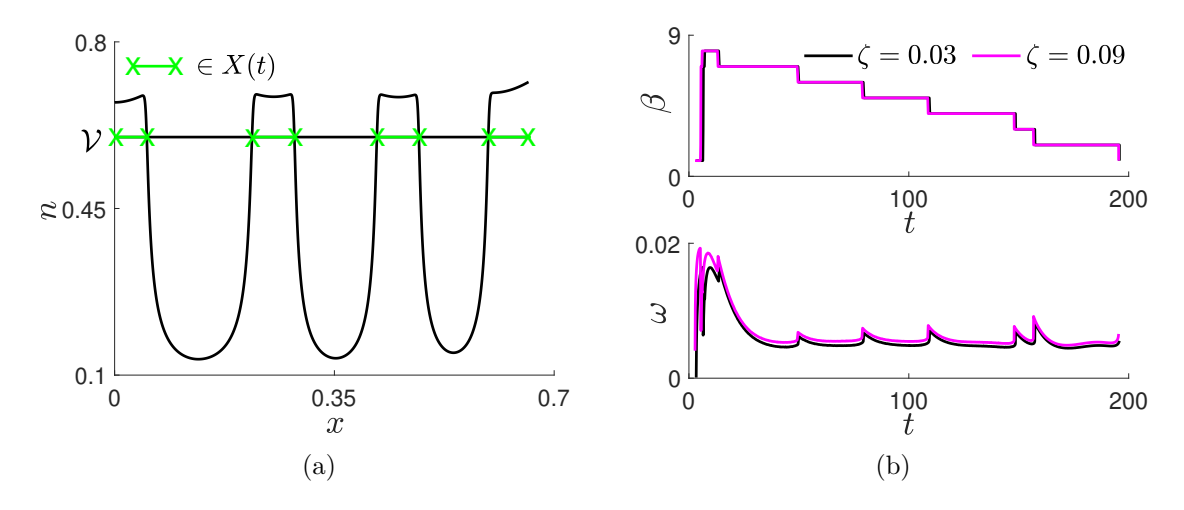


Figure 3.6: A quantification of patterned solution features. In (a), we present a numerical solution n(x,t) from the PDE system (3.20)– (3.23) at t=40 for $r_m=0.4$, $r_a=0.2$, $\phi=0.75$, $\kappa=25$ and $n_i(x)=\alpha+0.05\sin(15\pi x)$. The green line segments between the green crosses indicate the elements in X(t) from (3.89). In (b), we present the metrics $\beta(t)$ and $\omega(t)$ for $\zeta=0.03$ and $\zeta=0.09$. We use $r_m=0.3$, $r_a=0.2$, $\phi=0.85$, $\kappa=100$ and $n_i(x)$ defined as in (a).

containing these intervals, X(t), is defined as

$$X(t) := \left\{ x \in \left[0, L(t) \right] \mid n(x, t) > \mathcal{V} \right\} = \left\{ \left[x_{2i}, x_{2i+1} \right] \text{ for } i = 0, \dots, \beta(t) - 1 \right\},$$
(3.89)

so that $\beta(t)$ is the number of intervals at time t. Fig 3.6(a) shows an example patterned solution illustrating these intervals for a fixed value of t and \mathcal{V} , where we observe four cell peaks. We define the width of a cell peak occupying $[x_{2i}, x_{2i+1}]$ to be $x_{2i+1} - x_{2i}$. Since there are often multiple cell peaks, it is informative to obtain the average width of all cell peaks at any t. We define this average to be

$$\omega(t) = \frac{1}{\beta(t)} \sum_{i=0}^{\beta(t)-1} \left(x_{2i+1} - x_{2i} \right). \tag{3.90}$$

Furthermore, we restrict the t-dependent metrics $\beta(t)$ and $\omega(t)$ to $t \in [T_1, T_2]$, where T_1 and T_2 are the times at which the first and last single cell peak are observed, respectively. Naturally, the choice of the threshold \mathcal{V} can influence the metrics $\beta(t)$ and $\omega(t)$. As discussed in Section 3.3, the maximal volume fraction of cell peaks, such as those shown in yellow in Fig. 3.1(f), is approximately (but never exceeds) the value of n_{∞} . To capture the features of fully formed cell peaks, we therefore set $\mathcal{V} = n_{\infty} - \zeta$, where $\zeta > 0$ is small. In Fig. 3.6(b), we present $\beta(t)$ and $\omega(t)$ on $t \in [T_1, T_2]$, computed from the numerical solution of n(x, t) presented in Fig.

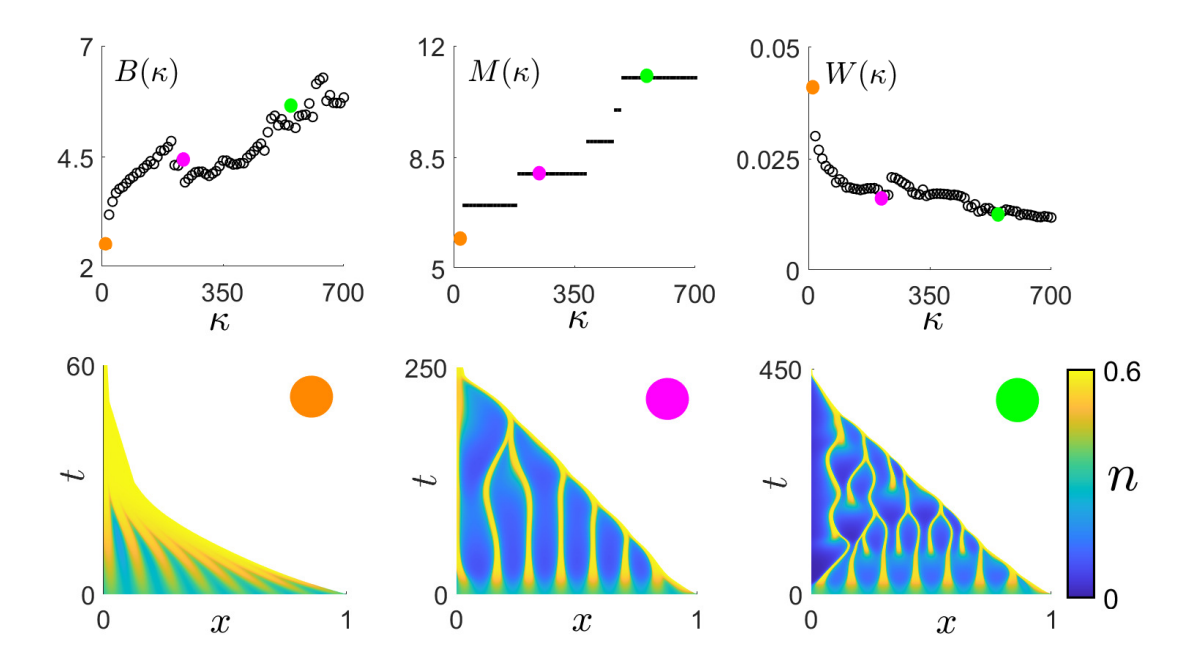


Figure 3.7: The variation of B, M and W from (3.91) with κ , computed from numerical solutions of the PDE system (3.20)– (3.23), together with exemplar numerical solutions of n(x,t) at $\kappa=5$ (orange dot), $\kappa=200$ (pink dot) and $\kappa=500$ (green dot). Remaining parameter values: $r_m=0.3, r_a=0.2, \phi=0.65, \nu=15$.

3.1(f), for two different values of ζ . The negligible difference between the metrics for the two values of ζ suggests that $\beta(t)$ and $\omega(t)$ are not sensitive to the value of ζ selected, and in the following we set $\zeta = 0.06$.

In order to examine how the model parameters affect the qualitative features of patterned solutions, it is instructive to associate the metrics $\beta(t)$ and $\omega(t)$ with scalar quantities. We define

$$M = \max_{t \in [T_1, T_2]} \beta(t), \qquad B = \frac{1}{(T_2 - T_1)} \int_{T_1}^{T_2} \beta(t) \, dt, \qquad W = \frac{1}{(T_2 - T_1)} \int_{T_1}^{T_2} \omega(t) \, dt.$$
(3.91)

Here, M describes the maximum number of cell peaks, whilst the time-averages B and W describe the average number and average width of cell peaks, in a given simulation of the MBM for $t \in [T_1, T_2]$. Additionally, we take $n_i(x) = \alpha + 0.05 \sin(\nu \pi x)$ where ν is a positive integer. By varying ν , we can investigate how the initial cell distribution affects the qualitative features of patterned solutions.

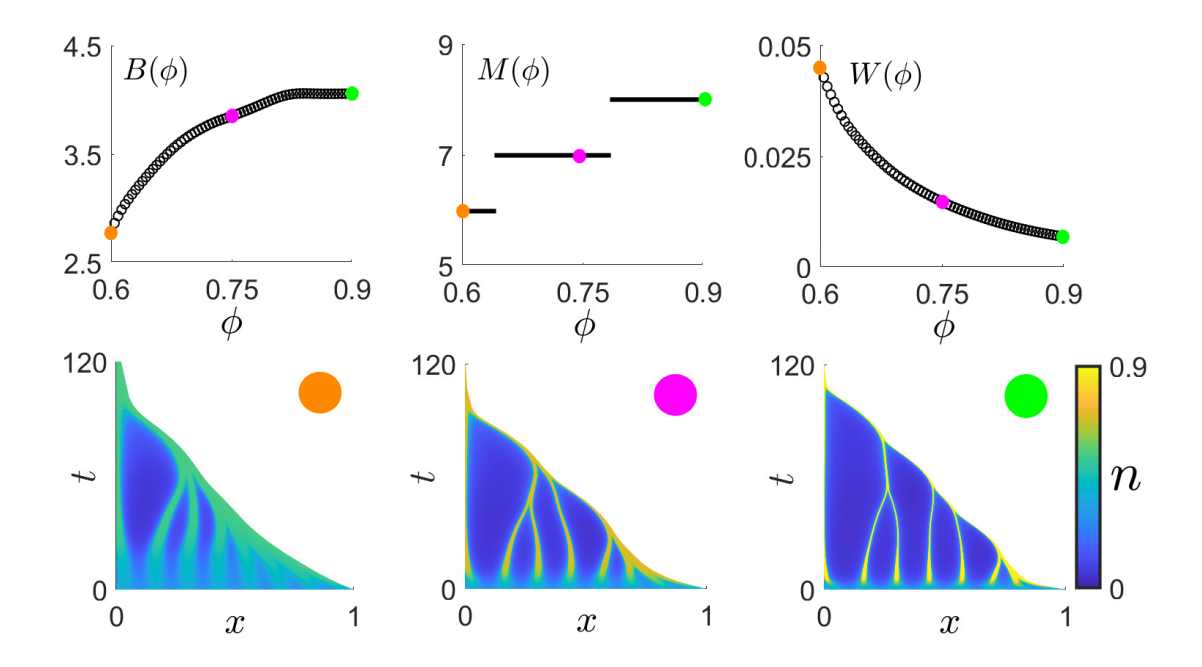


Figure 3.8: The variation of B, M and W from (3.91) with ϕ , computed from numerical solutions of the PDE system (3.20)– (3.23), together with exemplar numerical solutions of n(x, t) at $\phi = 0.6$ (orange dot), $\phi = 0.75$ (pink dot) and $\phi = 0.9$ (green dot). Remaining parameter values: $r_m = 0.3, r_a = 0.2, \kappa = 25, \nu = 15$.

3.6.2 Results

We now use the quantities described in (3.91) to investigate how the model parameters affect the qualitative features of patterned solutions. In Figs. 3.7, 3.8 and 3.9, we present the three quantities (B, M, W) as functions of κ , ϕ and ν , respectively. In each of these figures, we also include numerical solutions of n(x, t) from the PDE system (3.20)–(3.23) for three exemplar values of the respective parameter, as indicated by the coloured dots. The numerical solutions of n(x, t) presented in Figs. 3.7 and 3.9 suggest that the values of κ and ν have a significant effect on the number of cell peaks, and this observation is substantiated by the observed range over which the quantities B and M increase as functions of the parameters κ and ν . Furthermore, the numerical solutions of n(x, t) and the quantities $B(\phi)$ and $M(\phi)$ presented in Fig. 3.8 indicate that ϕ does not greatly influence the number of cell peaks. Interestingly, this observation indicates that the strength of attractive forces experienced by cells when $n < \phi$ is not indicative of the number of separate spheroids that result from the break-up of a suspension of $in\ vitro\ tumour\ cells$.

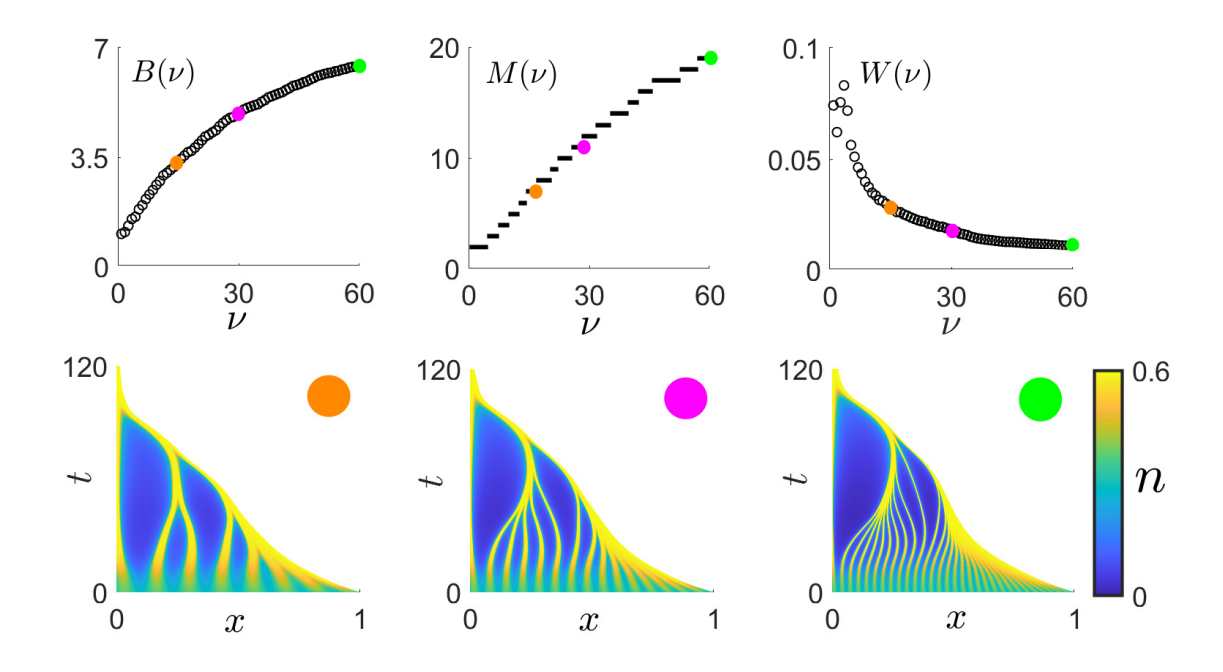


Figure 3.9: The variation of B, M and W from (3.91) with ν , computed from numerical solutions of the PDE system (3.20)– (3.23), together with exemplar numerical solutions of n(x, t) at $\nu = 15$ (orange dot), $\nu = 30$ (pink dot) and $\nu = 60$ (green dot). Remaining parameter values: $r_m = 0.3, r_a = 0.2, \phi = 0.65$ and $\kappa = 25$.

As highlighted by the metric $W(\phi)$ and the numerical solutions of n(x, t) presented in Fig. 3.8, the width of the cell peaks decreases as ϕ increases, as a result of the available cells migrating toward a larger natural packing density. In contrast to this, the quantities $W(\kappa)$ and $W(\nu)$ presented in Figs. 3.7 and 3.9 decrease due to the available cells being distributed over a larger number of cell peaks. In particular, the value of ν has the most significant effect on the cell peak width when compared with the effects of varying κ and ϕ . Whilst the number of cell peaks increase with κ and ν (as discussed above), the resulting decrease of cell peak width may have implications on the viability of new tumour spheroids that result from in vitro break-up.

Whilst the quantities $B(\kappa)$ and $B(\nu)$ provide insight into the average number of cell peaks, they do not capture the differences in the qualitative features of patterns seen in Figs. 3.7 and 3.9 at different points in time. For example, the patterned solutions in Fig. 3.9 illustrate that the number of cell peaks observed at early times are determined by the value of ν ; however, these peaks are not sustained and merge

together at a later time. Additionally, the patterned solutions in Fig. 3.7 indicate that the value of κ controls the number of peaks at later times. In particular, the pink-dot panel in Fig. 3.7 indicates that there exists a relationship between the values of κ and ν such that the cell peaks generated by the initial cell distribution are sustained throughout the tumour. However, for a sufficiently large value of κ , spontaneous pattern emergence is observed in the regions of low cell density, as illustrated in the green-dot panel in Fig. 3.7. In the context of *in vitro* tumour growth, these observations suggests that the initial cell distribution may have a limited effect on the number of cell peaks that can break away from a primary suspension of tumour cells to generate tumour spheroids, if there is insufficient drag between the cells and liquid. This observation is in agreement with the qualitative analysis of the multiphase description of in vitro liver cell aggregation presented in Green et al. (2009b).

3.7 A parameter case study: the $\kappa \to 0$ limit

In this section, we analyse the PDE system from (3.20)–(3.23) in the limit as $\kappa \to 0$. This limit is motivated by obtaining parameter values from experimental literature, which we now present.

To obtain a value for the dimensionless parameter κ , we must obtain estimates for the dimensional parameters χ , μ and L_0 . A value of the cell viscosity, μ , is reported by Lozoya and Lubkin (2012) to be in the range $10^4 - 10^6 \text{ N m}^{-2} \text{ s}$. This estimate was calculated by manipulating data in G. Forgacs G (1998) pertaining to the viscoelastic properties of embryonic tissue. We follow Green et al. (2009b) and take the value of the dimensional cell-liquid drag parameter, χ , to be in the range $10^7 - 10^{10} \text{ N m}^{-4} \text{ s}$. This range of values were obtained from data in Swabb et al. (1974) relating to hepatoma tissue. Finally, we set $L_0 = 10^{-4} \text{ m}$. This is consistent with the experimental values in Klowss et al. (2022) relating to the initial size of an in vitro tumour spheroid. Using the dimensional parameter values described above,

we have $\kappa \approx 10^{-7} - 10^{-2}$.

The remainder of this section is constructed as follows. In subsection 3.7.1, we formulate the leading order problem for $t = \mathcal{O}(1)$ when $\kappa \to 0$. In subsection 3.7.2, we then present some results which illustrate the behaviour of the $t = \mathcal{O}(1)$ problem, where it is shown that the criteria for growth or decay of the tumour edge is equivalent to that obtained in section 3.4.5. We note that in the case when the tumour edge grows, then the leading order problem at the final time scale $t = \mathcal{O}(\kappa^{-1/2})$ is obtained via the travelling-wave coordinates

$$\overline{L}(t) = \frac{ct}{\sqrt{\kappa}}, \qquad z = \sqrt{\kappa}x - \overline{L}(t), \qquad n = n(z), \qquad v_n = \frac{v_n(z)}{\sqrt{\kappa}},$$
 (3.92)

as described in section 3.4.5. In the case when the tumour edge decays, then the $t = \mathcal{O}(1)$ problem discussed shortly is uniformly valid as $t \to \infty$.

3.7.1 Formulation of the leading order problem for $t = \mathcal{O}(1)$

We now formulate the leading order problem arising from the system of PDEs (3.20)–(3.23) for $t = \mathcal{O}(1)$ as $\kappa \to 0$. To leading order in κ , (3.21) provides

$$\frac{\partial}{\partial x} \left[n \frac{\partial v_n}{\partial x} - n \Sigma(n) \right] = 0. \tag{3.93}$$

Integrating (3.93) and using the first boundary condition from (3.23), we obtain

$$\frac{\partial v_n}{\partial x} = \Sigma(n). \tag{3.94}$$

Combining (3.94) with (3.20) provides

$$\frac{\partial n}{\partial t} + v_n \frac{\partial n}{\partial x} = \Gamma(n) - n\Sigma(n). \tag{3.95}$$

The PDE system to leading order in κ for $t = \mathcal{O}(1)$ is therefore given by (3.95) and (3.94), which are coupled to boundary and initial conditions from (3.22) and (3.23). In Lemon and King (2007a), this system is shown to be amenable to a hodograph transformation (Clarkson et al., 1989) which reduces it to a first order linear PDE;

however, in this section we simplify the analysis by assuming that n is initially spatially uniform.

Following Lemon and King (2007a), equations (3.95) and (3.94) may be reduced further when n is initially spatially uniform, i.e. $n(x, 0) = n_0$ for constant n_0 , via solutions of the form

$$n = n(t), \quad v_n = v_0(t) + v(t)x,$$
 (3.96)

whereby using the condition $v_n(0,t) = 0$ provides $v_0(t) = 0$. Substituting (3.96) into (3.95), (3.94) and the moving boundary condition from (3.22) provides the leading order system on $x \in [0, L]$

$$\frac{\mathrm{d}n}{\mathrm{d}t} = \Gamma(n) - n\Sigma(n), \qquad v_n = \Sigma(n)x, \qquad \frac{\mathrm{d}L}{\mathrm{d}t} = \Sigma(n)L, \tag{3.97}$$

which is coupled to the initial conditions $n(0) = n_0$ and L(0) = 1. We note that the first of (3.97) can be integrated to provide the implicit solution

$$t = \Omega(n) - \Omega(n_0), \qquad \Omega'(n) = \frac{1}{\Gamma(n) - n\Sigma(n)}.$$
 (3.98)

Although $\Omega(n)$ can be obtained explicitly, the expression is long and complicated, and its inverse function cannot be calculated in closed-form so as to obtain n explicitly.

The system of nonlinear ODEs from (3.97) represents a novel formulation for several reasons. Firstly, the system (3.97) is derived systematically by considering a spatially dependent model based on cell behaviour. This is in contrast to many classical ODE models of tumour growth (see Murphy et al. (2016) for a review), whereby authors often use ODEs as the starting point for their analysis. Furthermore, the system (3.97) considers the effect of mechanical forces arising due to cell-cell interactions, in contrast with other traditional models which consider cell production and death only.

3.7.2 Results

We now illustrate the behaviour of the system from (3.97), which is valid in the limit $\kappa \to 0$ and when $t = \mathcal{O}(1)$. We first discuss the large-time behaviour of this system to obtain criteria for whether the position of the tumour edge grows or retreats. Following this, we present some numerical solutions of the system from (3.97), before discussing a special parameter regime in which (3.97) admits a closed-form solution.

Large-time behaviour

We now analyse the large-time behaviour of the system from (3.97). Given that the first from (3.97) is an autonomous ODE, we have that as $t \to \infty$

$$n \sim n_{\infty}, \qquad v_n \sim \Sigma(n_{\infty})x, \qquad L \sim e^{\Sigma(n_{\infty})t},$$
 (3.99)

where $\Gamma(n_{\infty}) - n_{\infty}\Sigma(n_{\infty}) = 0$. Consequently, the tumour edge will grow or decay exponentially depending on the sign of $\Sigma(n_{\infty})$ and hence the sign of $n_{\infty} - \phi$. If $n_{\infty} > \phi$, the cell volume fraction of the tumour is larger than the natural cell density, and repulsive forces experienced between cells results in the expansion of the tumour. Conversely, if $n_{\infty} < \phi$, cells attract one another and the tumour edge consequently recedes. If $n_{\infty} = \phi$, then from (3.97) we have that $n \sim \phi$ and $L \sim L_{\infty}$ as $t \to \infty$, where L_{∞} is a constant determined by n_0 . We note that the sign of $n_{\infty} - \phi$ is the same as the sign of $\alpha - \phi$, so that the criteria for growth or decay of the moving boundary as $\kappa \to 0$ agrees with that obtained in section 3.4.5.

Numerical results

In figure 3.10, we compare the numerical solutions for n(x, t) on $0 \le x \le L(t)$ obtained from the PDE system from (3.20)–(3.23) for $\kappa = 0.001$, against the solutions of the leading order problem from (3.97) for two choices of ϕ . The numerical solutions of (3.97) are obtained via the function ode45 in MATLAB. Overall, an excellent agreement between the numerical and asymptotic solutions is observed.

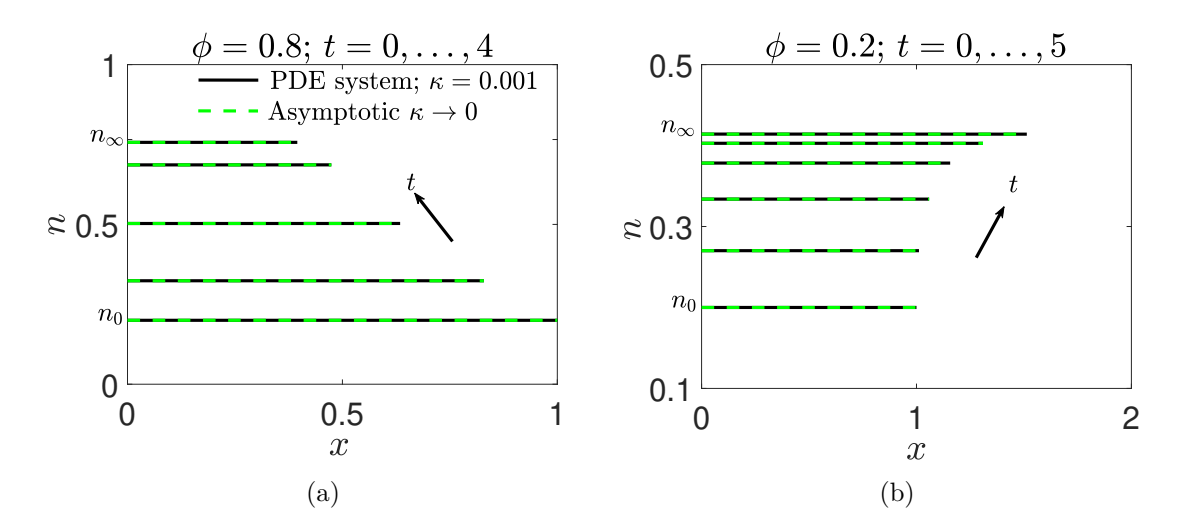


Figure 3.10: Numerical solution (solid black line) of the PDE system from (3.20)–(3.23) when $\kappa = 0.001$ against asymptotic solution (dashed green line) obtained from (3.97) for $n_0 = 0.2$ and two different values of ϕ . Parameter values: $r_m = 0.8$ and $r_a = 0.3$.

To compare the numerical solutions of n(x, t) from the PDE system (3.20)–(3.23) for small κ against the leading order solutions of (3.97) on a temporal domain, we now define

$$n_a(t) = \frac{1}{L(t)} \int_0^{L(t)} n(x, t) dx.$$
 (3.100)

This spatial average associates the near-spatially-uniform solution obtained from the PDE system (3.20)–(3.23) with a single value at any t.

In figure 3.11, we compare the numerical solutions of $n_a(t)$ and $\log(L)$ obtained from the PDE system (3.20)–(3.23) when $\kappa = 0.001$, against the numerical solution of n(t) and $\log(L)$ obtained from (3.97) for various ϕ . Overall, an excellent agreement between the numerical and asymptotic solutions is observed. In figure 3.11(a), we observe sigmoidal growth in the cell volume fraction, whilst figure 3.11(b) highlights the eventual exponential growth or decay of the tumour boundary after a period of transient behaviour. Notably, and in agreement with the large-time behaviour discussed above, the case in which the volume fraction of cells is largest and smallest results in exponential decay and growth of the tumour edge, respectively. This observation is striking, as it is plausible to expect that a tumour with a large volume fraction of cells will result in growth of the tumour boundary rather than decay. Furthermore, we observe in figure 3.11(b) that L(t) initially decreases before subse-

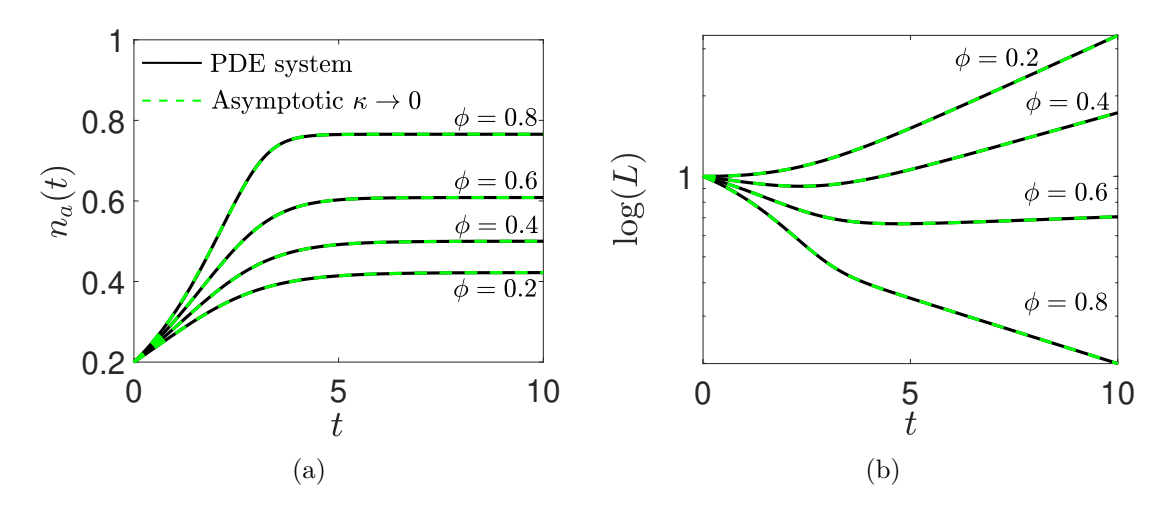


Figure 3.11: The quantity $n_a(t)$ (solid black line) obtained from numerical solution of the PDE system from (3.20)–(3.23) when $\kappa = 0.001$ against $n_a(t)$ asymptotic solution (dashed green line) obtained from (3.97) for $n_0 = 0.2$ and four different values of ϕ . Parameter values: $r_m = 0.8$ and $r_a = 0.3$.

quently increasing exponentially when $\phi = 0.4$ and $\phi = 0.6$. This initial decrease is illustrated by the small-time behaviour $L \sim 1 + \Sigma(n_0)t$ valid for $t \ll 1$, suggesting that L will initially increase or decrease based on the sign of $n_0 - \phi$. This condition contrasts the large-time condition for the growth or decay of L based on the sign of $n_\infty - \phi$, so that the initial behaviour of L does not necessarily predict its large-time behaviour.

Analytical results

The system from (3.97) can be solved explicitly in the special case $r_a = \phi$ because the inverse of $\Omega(n)$ from (3.98) is available in closed form. When $r_a = \phi$, the first from (3.98) provides

$$n(t) = \frac{r_m - \phi - \sqrt{(r_m - \phi)^2 + (r_m - \phi)(1 - r_m + Ae^{2(\phi - r_m)t})}}{1 - r_m - Ae^{2(\phi - r_m)t}},$$
 (3.101)

where

$$A = \frac{\phi(2n_0 - 1) + r_m(n_0 - 1)^2}{n_0^2} - 1.$$
 (3.102)

The solution from (3.101) indicates that n(t) increases logistically from the initial conditions, and is similar to the solution of the classical logistics ODE commonly employed to model tumour growth (Vaghi et al., 2020).

3.8 Conclusion

In this chapter, we analyse spatially-patterned and travelling-wave solutions of the two-phase, moving boundary model of tumour growth developed in Byrne et al. (2002). The model consists of two equations governing a cell volume fraction denoted by n and its associated velocity, as well as a moving boundary condition for the tumour edge. Mechanisms to represent forces generated by cell-cell interactions are accounted for by considering relevant constitutive assumptions in a similar fashion to those in Byrne et al. (2002) and Breward et al. (2002). One important parameter related to cell-cell interactions is ϕ , which represents the cells' natural packing density. If $n > \phi$, then cells repel each other to relieve membrane stress, and if $n < \phi$, then cells will attract one another due to their filopodia coming into contact. In keeping with King and Franks (2004), we assume that nutrient is abundantly distributed throughout the tumour. Whilst this assumption omits important elements such as nutrient limited induced cell death, it is physically relevant in the context of an in vivo tumour in the initial stage of development where all cells are adequately nourished. Additionally, this nutrient rich assumption is appropriate when considering the initial growth of a suspension of in vitro tumour cells (Byrne et al., 2002). Whilst the model developed in Byrne et al. (2002) pertains to both in vivo and in vitro tumour growth, the techniques developed in its analysis regarding pattern formation can be applied to a wider class of multiphase tissue growth models, such as that described in Lemon and King (2007a).

Solutions of the tumour model analysed herein can develop into a forward- or backward-moving travelling wave, which correspond to the growth or retreat of the tumour edge, the latter resulting in tumour extinction. A travelling-wave analysis is used to obtain criteria for the growth or extinction of the tumour via stable travelling waves, in terms of model parameters. We determine that forward-moving travelling-wave solutions have $n > \phi$ behind the wave-front, and cells are in a constant state of repulsion. Consequently, the tumour edge expands to provide space in which

the cells can migrate. Conversely, if $n < \phi$, cells behind the wave-front are in a constant state of attraction, which results in the contraction of the tumour edge and a backward-moving travelling wave. We find that the tumour grows the fastest when the rate of cell production is large, but the cells' natural packing density is small (thereby increasing the strength of repulsive forces experienced between cells when $n > \phi$). We also find that the value of the cell-liquid drag does not determine the direction of travelling waves, but does significantly control the wave speed.

We also observe patterned solutions that are associated with multiple regions of high cell density (termed cell peaks) separated by regions of low cell density. From an initial cell distribution, cells migrate up gradients of n from regions of low to high density to form distinct cell peaks, due to attractive forces experienced between them when $n < \phi$. This attraction results in the contraction of the tumour, and consequently the eventual extinction of the tumour. Nevertheless, patterned solutions observed prior to extinction retain a degree of biological relevance. For example, and as described in Green et al. (2009b), the inherent structural instability of a suspension of in vitro tumour with patterned structures could lead to break-up, and consequently the formation of separate spheroids. Whilst the aspect of tumour break-up is not explicitly modelled here, a qualitative analysis of patterned solutions nonetheless provides insight into how model parameters could affect the onset of such a process. Notably, we find that the initial cell distribution only determines the number of cell peaks within the tumour at early times, whereas the value of the cell-liquid drag determines the number of cell peaks at later times. This suggests that the initial cell distribution could have a limited effect on the number of new spheroids that result from in vitro tumour break-up, which is in agreement with the qualitative analysis of the multiphase description of in vitro liver cell aggregation presented in Green et al. (2009b).

We determine the instability of travelling-wave solutions in time to obtain regions of parameter space in which patterned solutions are observed. This stability analysis incorporates the effects of the boundary conditions imposed at the tumour edge and tumour core, as well as the moving tumour edge. The accuracy of the stability regions generated by this linear stability analysis are verified by comparing them with numerical solutions of the cell volume fraction in suitable parameter regimes. The biological implications of the travelling-wave stability analysis suggest that pattern solutions will emerge if there is insufficient net cell growth to support the attraction of cells uniformly toward their natural packing density.

In addition to the travelling-wave stability analysis described above, we determine the stability of a spatially-uniform steady state. In contrast to the travellingwave stability analysis, this spatially-uniform steady state does not satisfy the moving boundary condition at the tumour edge. Interestingly, however, the regions of instability obtained via the travelling-wave and spatially-uniform stability analyses are in very good agreement, suggesting that the inclusion or exclusion of the moving boundary does not determine when patterned solutions will form. We therefore expect the destabilising mechanism giving rise to pattern formation to be the attractive forces experienced by cells occurring when $n < \phi$. A similar multiphase moving boundary model to that described in this chapter is presented in Lemon and King (2007a), and the stability of a spatially-uniform steady state (which does not satisfy the moving boundary condition) is analysed to obtain criteria in which pattern-forming solutions are expected. The good agreement between the two types of stability analyses presented in this chapter provides a justification for exploiting the simpler spatially-uniform analysis, such as for the class of multiphase models in Lemon and King (2007a).

One interpretation of the initial cell volume fraction distribution in our model is a uniform suspension of cells on a substrate. Whilst a travelling-wave solution represents uniform growth of these cells, pattern formation can be associated with aggregation and tumour cell cluster formation, see Beaune et al. (2014) for experimental illustrations of this process. In suitable growth conditions, these clusters will detach from the substrate and form individual multicellular tumour spheroids, although this is not explicitly modelled here. As such, we believe the analysis and

results in this chapter provide a framework for determining the successful generation of tumour spheroids from substrate suspensions. Following Green et al. (2009b), our analysis could be extended to incorporate the effects of the substrate.

A possible extension of the work presented in this chapter is to investigate how additional constitutive assumptions describing cell-cell interactions affect the onset of pattern formation. For example, in Breward et al. (2002), a mechanism is employed in the constitutive assumptions that ensures attractive forces experienced between cells are short-range, so that cells do not attempt to cluster if they are too far apart. Another natural extension of this work is to examine the influence that nutrient limitation has on the onset of pattern formation within a tumour. In contrast to the model presented in this chapter, preliminary numerical simulations of the nutrient-limited extension indicate that pattern-forming solutions can exist on a growing spatial domain.

Chapter 4

A multiphase model for nutrient limited tumour growth

4.1 Introduction

In this chapter, we analyse solutions of the multiphase, moving boundary model developed in Byrne et al. (2002). This model describes solid tumour growth, and considers the evolution of a motile, viscous cell phase and an inviscid extra-cellular liquid phase, both of which are modelled as incompressible fluids. In contrast to the previous chapter, we now assume that a single diffusive concentration of nutrient is present in the tumour. Tissue mechanics, cellular growth and a mechanism to represent cell-liquid drag are accounted for by considering relevant constitutive assumptions in a similar fashion to those in Byrne et al. (2002) and Breward et al. (2002).

A detailed analysis of the two-phase model of Byrne et al. (2002) is provided in Breward et al. (2002), and the cell phase in this model exhibits either travelling waves which propagate with constant speed or a steady state, both of which are in agreement with experimental observations. The analysis presented in Breward et al. (2002) focuses on investigating the effects of varying parameters related to cell-liquid drag and cell viscosity on a growing tumour, and finds that increasing these parameters results in a reduction of the rate of tumour growth. In this chapter,

however, we focus on investigating the effects of varying parameters directly relating to the nutrient distribution within a tumour, i.e. nutrient diffusivity. In contrast to Breward et al. (2002), we also formulate the travelling-wave ODEs corresponding to the model of Byrne et al. (2002), and provide a numerical method to obtain their solutions.

The chapter is constructed as follows. In section 4.2, a summary of the twophase model developed in Byrne et al. (2002) is presented and subsequently nondimensionalised. Following this, some exemplar numerical solutions of the model are
presented in section 4.4.2, which exhibit forward-moving travelling waves, steadystate solutions, and solutions representing tumour extinction. In section 4.4, a
travelling-wave analysis is presented. This allows us to investigate the effects of
varying parameters related to nutrient distribution on a growing tumour. After
this, we obtain criteria for the extinction of the tumour in section 4.5; interestingly,
this criteria depends only on parameters related to cell growth and motility, and not
on parameters related to nutrient distribution such as nutrient diffusivity.

4.2 Model development

We now present a summary of the two phase model developed in Byrne et al. (2002), which describes the growth of a solid tumour. As described in section 3.2, this model consists of two phases denoted by n(x, t) and w(x, t), that represent the volume fraction of cells and extracellular liquid, respectively. These phases satisfy the no-voids volume constraint n + w = 1. The velocity fields $v_n(x, t)$ and $v_w(x, t)$ are associated with the phases n and w, accordingly. We model the cell and liquid phases as viscous and inviscid fluids, respectively. In contrast to chapter 3, the rates of cell growth and cell death are now dependent on a single diffusive concentration of nutrient denoted by c(x, t). The spatial domain of the tumour evolves over time due to cellular motion, so the volume fractions n and w evolve on the moving domain $0 \le x \le L(t)$, where x = 0 and x = L(t) denote the tumour core and tumour edge,

respectively.

As derived in section 3.2, the dimensional equations governing the quantities n(x, t), $v_n(x, t)$ and L(t) are given by

$$\frac{\partial n}{\partial t} + \frac{\partial}{\partial x}(nv_n) = \Gamma(n, c), \tag{4.1}$$

$$\mu \frac{\partial}{\partial x} \left(n \frac{\partial v_n}{\partial x} \right) - \frac{\partial}{\partial x} \left[n \Sigma(n) \right] - \frac{\chi n v_n}{1 - n} = 0, \tag{4.2}$$

$$\frac{\mathrm{d}L}{\mathrm{d}t} = v_n(L, t),\tag{4.3}$$

$$\mu \frac{\partial v_n}{\partial x}\Big|_{x=L} = \Sigma(n)\Big|_{x=L}, \quad v_n(0, t) = 0, \quad n(x, 0) = n_i(x), \quad L(0) = L_0.$$
 (4.4)

Here, $\Gamma(n, c)$ is the net rate of cell proliferation which is now dependent on the nutrient c(x, t), and $\Sigma(n)$ represents additional pressures that arise due to cell-cell interactions and is stated explicitly in (3.10). The positive constants μ and χ represent the values of the viscosity of the cell phase and interphase drag between the cells and the liquid, respectively.

We now derive the equations governing the nutrient, c(x, t). Remaining consistent with Byrne et al. (2002) and Breward et al. (2002), we assume that the nutrient is uniformly distributed in the tumour surroundings, is consumed by cells and is transported within the cell and liquid phases via both advection and diffusion. In view of these processes, the equation governing the nutrient c(x, t) is given by

$$\frac{\partial c}{\partial t} + \frac{\partial}{\partial x} [c(nv_n + wv_w)] = D \frac{\partial^2 c}{\partial x^2} - \overline{Q}(n, c), \tag{4.5}$$

where \overline{Q} is the rate at which cells consume nutrient and D is the constant diffusivity of the nutrient. We assume that the time-scales associated with nutrient diffusion and consumption are much shorter than that of tumour growth (Byrne et al., 2002; Lemon and King, 2007b), so that the first term in (4.5) may be neglected to obtain

$$\frac{\partial^2 c}{\partial x^2} = Q(n, c), \tag{4.6}$$

where $Q = \overline{Q}/D$ and (3.16) is used to eliminate the advection term from (4.5). We assume that the tumour is symmetric about its centre (x = 0) and that the concentration of nutrient is fixed at the tumour edge, so that

$$\frac{\partial c}{\partial x} = 0$$
 at $x = 0$ and $c = c_{\infty}$ at $x = L(t)$, (4.7)

where c_{∞} is a positive constant.

4.2.1 Constitutive assumptions

We now define constitutive assumptions for $\Gamma(n, c)$ and Q(n, c) that are suitable to describe tumour growth. We assume that daughter cells are constructed via mitosis using the available liquid, and that when cells die they dissolve into the liquid. We also assume that the rates of mitosis and death are regulated by the available nutrient. Following these assumptions, we take

$$\Gamma(n, c) = k_m(c)n(1-n) - k_d(c)n,$$
(4.8)

where k_m and k_d are the positive rates of cell mitosis and death. Following King and Franks (2004), we assume that the rate at which cells consume nutrient is proportional to the available nutrient and set

$$Q(n, c) = \rho nc, \tag{4.9}$$

where ρ is a positive constant which describes the ratio between the nutrient consumption rate and nutrient diffusivity.

The functions k_m and k_d should be monotonically increasing and decreasing functions, respectively, to account for the fact that inadequate levels of nutrient will reduce and increase the rate of cell proliferation and death. We therefore adopt the linear kinetics

$$k_m(c) = r_m c, \qquad k_d(c) = r_a(\sigma - c) \tag{4.10}$$

where r_m and r_a are positive constants and $\sigma > c_\infty$ is required to retain positivity

in $k_d(c)$. We note that even in optimal nutrient conditions, i.e. $c=c_{\infty}$, we have $k_d(c_{\infty})=r_a(\sigma-c_{\infty})>0$ which accounts for cell death via apoptosis.

4.2.2 Non-dimensionalisation

We now non-dimensionalise the model consisting of (4.1)–(4.4), (4.6) and (4.7). By introducing the dimensionless variables

$$\hat{t} = \frac{\tau}{\mu}t, \qquad \hat{x} = \frac{x}{L_0} \qquad \hat{v}_n = \frac{\mu}{\tau L_0}v_n, \qquad \hat{L} = \frac{L}{L_0}, \qquad \hat{c} = \frac{c}{c_\infty}$$
 (4.11)

the following dimensionless model results:

$$\frac{\partial n}{\partial \hat{t}} + \frac{\partial}{\partial \hat{x}} (n\hat{v}_n) = \hat{\Gamma}(n, \, \hat{c}), \qquad 0 < \hat{x} < \hat{L}, \tag{4.12}$$

$$\frac{\partial}{\partial \hat{x}} \left(n \frac{\partial \hat{v}_n}{\partial \hat{x}} \right) - \frac{\partial}{\partial \hat{x}} \left[n \hat{\Sigma}(n) \right] - \kappa \frac{n \hat{v}_n}{1 - n} = 0, \qquad 0 < \hat{x} < \hat{L}, \tag{4.13}$$

$$\frac{\partial^2 c}{\partial \hat{x}^2} = \hat{\rho} n \hat{c}, \qquad 0 < \hat{x} < \hat{L}, \qquad (4.14)$$

$$\frac{\mathrm{d}\hat{L}}{\mathrm{d}\hat{t}} = \hat{v}_n(\hat{L}, \,\hat{t}),\tag{4.15}$$

$$\frac{\partial \hat{v}_n}{\partial \hat{x}}\Big|_{\hat{x}=\hat{L}} = \hat{\Sigma}(n)\Big|_{\hat{x}=\hat{L}}, \qquad \hat{v}_n(0,\,\hat{t}) = 0, \qquad \hat{c}(\hat{L},\,\hat{t}) = 1, \qquad \frac{\partial \hat{c}}{\partial \hat{x}}\Big|_{\hat{x}=0} = 0, \quad (4.16)$$

$$n(\hat{x}, 0) = n_i(\hat{x}), \qquad \hat{L}(0) = 1,$$

$$(4.17)$$

where

$$\hat{\Gamma}(n,\,\hat{c}) = \hat{r}_m n(1-n)\hat{c} - \hat{r}_a n(\hat{\sigma} - \hat{c}), \qquad \hat{\Sigma}(n) = \frac{\Sigma(n)}{\tau},\tag{4.18}$$

and $\hat{r}_m = c_{\infty} r_m \mu / \tau$, $\hat{r}_a = c_{\infty} r_a \mu / \tau$, $\hat{\sigma} = \sigma / c_{\infty}$, $\hat{\rho} = \rho L_0^2$, $\kappa = \chi L_0^2 / \mu$. In the following, we dispense with the hat notation for clarity.

As described in section 3.2, combining (4.12), (4.15) and the first and third from (4.16) at x = L(t) provides the autonomous ODE

$$\frac{\mathrm{d}n_L}{\mathrm{d}t} = \Gamma(n_L, 1) - n_L \Sigma(n_L), \tag{4.19}$$

where $n_L = n(L, t)$ so that if $r_m > r_a(\sigma - 1)$, then $n_L \sim n_\infty$ for sufficiently large time, where $\Gamma(n_\infty, 1) - n_\infty \Sigma(n_\infty) = 0$. We assume that $r_m > r_a(\sigma - 1)$ so that there is net cell growth at the tumour edge. In subsequent large-time analysis we may therefore replace the first boundary condition from (4.16) with

$$n = n_{\infty}$$
 or $\frac{\partial v}{\partial x} = \Sigma(n_{\infty})$ at $x = L(t)$. (4.20)

4.3 Numerical results

To illustrate the behaviour of the model from (4.12)–(4.17), we present and discuss some exemplar numerical solutions on the moving domain $0 \le x \le L(t)$.

4.3.1 Numerical methods

To obtain numerical solutions of (4.12)–(4.17), we fix the moving boundary by scaling x with L(t) as $\xi = x/L(t)$, so that $\xi \in [0, 1]$, and the model becomes

$$\frac{\partial n}{\partial t} = \frac{1}{L} \frac{\partial n}{\partial \xi} \left(\xi \frac{\mathrm{d}L}{\mathrm{d}t} - v_n \right) - \frac{n}{L} \frac{\partial v_n}{\partial \xi} + \Gamma(n, c), \tag{4.21}$$

$$\frac{1}{L^2} \frac{\partial}{\partial \xi} \left(n \frac{\partial v_n}{\partial \xi} \right) - \frac{1}{L} \frac{\partial}{\partial \xi} \left[n \Sigma(n) \right] - \kappa \frac{n v_n}{1 - n} = 0, \tag{4.22}$$

$$\frac{1}{L^2} \frac{\partial^2 c}{\partial \xi^2} = \rho n c, \tag{4.23}$$

$$\frac{\mathrm{d}L(t)}{\mathrm{d}t} = v_n(1, t),\tag{4.24}$$

$$\frac{1}{L} \frac{\partial v_n}{\partial \xi} (1, t) = \Sigma(n) \bigg|_{\xi = 1}, \quad v_n(0, t) = 0, \quad \frac{\partial c}{\partial \xi} \bigg|_{\xi = 0} = 0, \quad c(1, t) = 1, \quad (4.25)$$

$$n(\xi, 0) = n_i(\xi), \qquad L(0) = 1.$$
 (4.26)

The numerical methods used to solve this system for $c \equiv 1$ are described in section 3.3, wherein ξ is partitioned uniformly and the dependent variables are spatially

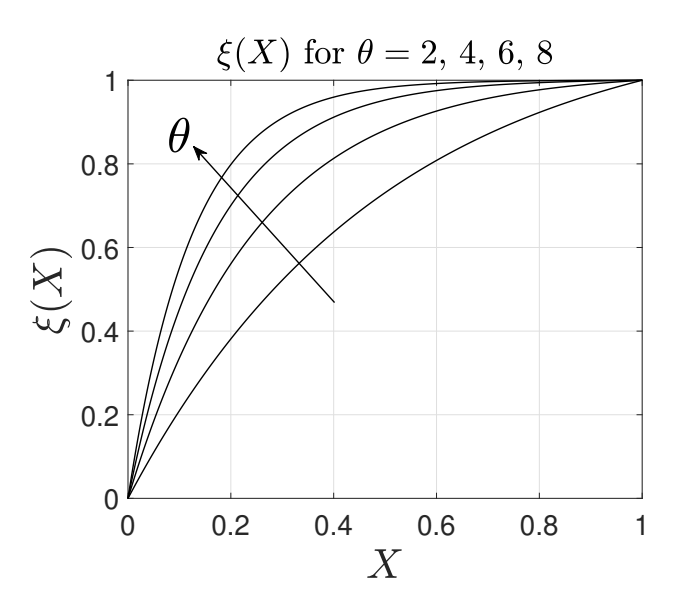


Figure 4.1: The function ξ from (4.27) for $\theta = 2, 4, 6, 8$ and K = 1000.

discretised using finite differences. In contrast, we now develop a numerical scheme where ξ is not partitioned uniformly, with a concentrated number of mesh points in the vicinity of $\xi = 1$. This allows accurate solutions of (4.21)–(4.26) to be obtained for large ρ , for which a boundary-layer forms at $\xi = 1$.

To partition $\xi \in [0, 1]$ non-uniformly, we first uniformly partition the interval $X \in [0, 1]$ such that $X_i = i\Delta X$ for i = 0, ..., K, where $\Delta X = 1/K$ and K + 1 is the number of spatial nodes. We then introduce the discrete function $\xi_i(X_i)$, which maps the uniform mesh X_i to the non-uniform mesh ξ_i , such that

$$\xi_i(X_i) = \left(1 + \frac{e^{\theta}}{1 - e^{\theta}}\right) e^{\theta(1 - X_i)} - \frac{e^{\theta}}{1 - e^{\theta}},$$
 (4.27)

whereby increasing the constant $\theta > 0$ increases the number of spatial nodes in the vicinity of $\xi_i = 1$. We note that the monotone increasing function ξ_i preserves the important properties $\xi(0) = 0$ and $\xi(1) = 1$. In figure 4.1, we plot the function $\xi_i(X_i)$ for five values of θ , which illustrates that the concentration of mesh points in the vicinity $\xi = 0$ and $\xi = 1$ decreases and increases under the mapping $\xi_i(X_i)$, respectively.

Using the non-uniform mesh ξ_i , we spatially discretise (4.21), (4.22) and (4.23) using finite differences and introduce the semi-discretised variables $n_i(t) = n(\xi_i, t)$, $v_i(t) = n(\xi_i, t)$

 $v_n(\xi_i, t)$ and $c_i(t) = c(\xi_i, t)$. Upwind or downwind finite differences are used for the first term on the right-hand side of (4.21), the direction of which is determined by the sign of the quantity in the brackets. The explicit finite difference scheme corresponding to (4.21), (4.24) and (4.26) for i = 0, ..., K is given by

$$\frac{\partial n_{i}}{\partial t} = \left(\xi_{i}v_{K} - v_{i}\right) \cdot \frac{1}{L} \begin{cases} \frac{n_{i+1} - n_{i}}{\xi_{i+1} - \xi_{i}} & \text{if } \xi_{i}v_{K} - v_{i} > 0 \text{ or } i = 0, \\ \frac{n_{i} - n_{i-1}}{\xi_{i} - \xi_{i-1}} & \text{if } \xi_{i}v_{K} - v_{i} < 0 \text{ or } i = K, \end{cases}$$

$$-\frac{n_{i}}{L} \cdot \begin{cases} \frac{v_{1}}{\xi_{1} - \xi_{0}} & \text{if } i = 0, \\ \frac{v_{i+1} - v_{i-1}}{\xi_{i+1} - \xi_{i-1}} & \text{if } i = 1, \dots, K - 1, + \Gamma(n_{i}, c_{i}), \\ \frac{v_{K} - v_{K-1}}{\xi_{N} - \xi_{N-1}} & \text{if } i = K, \end{cases}$$

$$(4.28)$$

$$\frac{\mathrm{d}L}{\mathrm{d}t} = v_K,\tag{4.29}$$

$$v_K = L\Sigma(n_K)(\xi_K - \xi_{K-1}) + v_{K-1}, \qquad v_0 = 0, \qquad c_K = 1, \qquad c_0 = c_1.$$
 (4.30)

The equations from (4.28) and (4.29) are then numerically integrated in time using the function ode45 in MATLAB, which uses a Runge-Kutta method.

Using central discretisations for both first- and second-order derivatives, the finite difference scheme corresponding to (4.22) for i = 2, ..., K-2 is given by

$$\frac{n_{i}}{(L)^{2}} \cdot \frac{v_{i+1}(\xi_{i} - \xi_{i-1}) - v_{i}(\xi_{i+1} - \xi_{i-1}) + v_{i-1}(\xi_{i+1} - \xi_{i})}{\frac{1}{2}(\xi_{i+1} - \xi_{i-1})(\xi_{i+1} - \xi_{i})(\xi_{i} - \xi_{i-1})} + \frac{1}{L^{2}} \cdot \frac{n_{i+1} - n_{i-1}}{\xi_{i+1} - \xi_{i-1}} \cdot \frac{v_{i+1} - v_{i-1}}{\xi_{i+1} - \xi_{i-1}} - \frac{1}{L} \cdot \frac{n_{i+1} - n_{i-1}}{\xi_{i+1} - \xi_{i-1}} \cdot F(n_{i}) - \kappa \frac{n_{i}v_{i}}{(1 - n_{i})} = 0.$$
(4.31)

This equation can be rearranged to give

$$A_i v_{i+1} + B_i v_i + C_i v_{i-1} + D_i = 0, (4.32)$$

where

$$A_{i} = \frac{n_{i}}{L^{2}(\xi_{i+1} - \xi_{i-1})(\xi_{i+1} - \xi_{i})} + \frac{n_{i+1} - n_{i-1}}{(L)^{2}(\xi_{i+1} - \xi_{i-1})^{2}},$$
(4.33)

$$B_{i} = -\frac{2n_{i}}{(L)^{2}(\xi_{i+1} - \xi_{i})(\xi_{i} - \xi_{i-1})} - \kappa \frac{n_{i}}{(1 - n_{i})},$$
(4.34)

$$C_{i} = \frac{n_{i}}{L^{2}(\xi_{i+1} - \xi_{i-1})(\xi_{i} - \xi_{i-1})} - \frac{n_{i+1} - n_{i-1}}{L^{2}(\xi_{i+1} - \xi_{i-1})^{2}},$$
(4.35)

$$D_i = -\frac{1}{L} \cdot \frac{n_{i+1} - n_{i-1}}{\xi_{i+1} - \xi_{i-1}} \cdot F(n_i). \tag{4.36}$$

The finite difference schemes corresponding to (4.22) for i = 1 and i = K - 1 are found by imposing the first two boundary conditions from (4.30) onto (4.32), and are given by

$$A_1 v_3 + B_1 v_2 + D_1 = 0, (4.37)$$

$$\underbrace{\left(A_{K-1} + B_{K-1}\right)}_{=\Upsilon_{K-1}^{B}} v_{K-1} + C_{K-1}v_{K-2} + \underbrace{\frac{A_{K-1}L\Sigma(n_{K})(\xi_{K} - \xi_{K-1})}{3} + D_{K-1}}_{=\Upsilon_{K-1}^{D}} = 0,$$

$$\underbrace{\left(A_{K-1} + B_{K-1}\right)}_{=\Upsilon_{K-1}^{B}} v_{K-1} + C_{K-1}v_{K-2} + \underbrace{\frac{A_{K-1}L\Sigma(n_{K})(\xi_{K} - \xi_{K-1})}{3} + D_{K-1}}_{=\Upsilon_{K-1}^{D}} = 0,$$

$$\underbrace{\left(A_{K-1} + B_{K-1}\right)}_{=\Upsilon_{K-1}^{D}} v_{K-1} + C_{K-1}v_{K-2} + \underbrace{\frac{A_{K-1}L\Sigma(n_{K})(\xi_{K} - \xi_{K-1})}{3} + D_{K-1}}_{=\Upsilon_{K-1}^{D}} = 0,$$

$$\underbrace{\left(A_{K-1} + B_{K-1}\right)}_{=\Upsilon_{K-1}^{D}} v_{K-1} + C_{K-1}v_{K-2} + \underbrace{\frac{A_{K-1}L\Sigma(n_{K})(\xi_{K} - \xi_{K-1})}{3} + D_{K-1}}_{=\Upsilon_{K-1}^{D}} = 0,$$

$$\underbrace{\left(A_{K-1} + B_{K-1}\right)}_{=\Upsilon_{K-1}^{D}} v_{K-1} + C_{K-1}v_{K-2} + \underbrace{\frac{A_{K-1}L\Sigma(n_{K})(\xi_{K} - \xi_{K-1})}{3} + D_{K-1}}_{=\Upsilon_{K-1}^{D}} = 0,$$

$$\underbrace{\left(A_{K-1} + B_{K-1}\right)}_{=\Upsilon_{K-1}^{D}} v_{K-1} + C_{K-1}v_{K-2} + \underbrace{\frac{A_{K-1}L\Sigma(n_{K})(\xi_{K} - \xi_{K-1})}{3} + D_{K-1}}_{=\Upsilon_{K-1}^{D}} = 0,$$

$$\underbrace{\left(A_{K-1} + B_{K-1}\right)}_{=\Upsilon_{K-1}^{D}} v_{K-1} + C_{K-1}v_{K-2} + \underbrace{\frac{A_{K-1}L\Sigma(n_{K})(\xi_{K} - \xi_{K-1})}{3} + D_{K-1}}_{=\Upsilon_{K-1}^{D}} = 0,$$

$$\underbrace{\left(A_{K-1} + B_{K-1}\right)}_{=\Upsilon_{K-1}^{D}} v_{K-1} + C_{K-1}v_{K-2} + \underbrace{\frac{A_{K-1}L\Sigma(n_{K})(\xi_{K} - \xi_{K-1})}{3} + D_{K-1}}_{=\Upsilon_{K-1}^{D}} = 0,$$

respectively. The solution to v_i is obtained by assembling (4.32), (4.37) and (4.38) into the matrix-vector form $\mathcal{M}\mathbf{v} = \mathbf{f}$, where $\mathbf{v} = (v_1, \ldots, v_i, \ldots, v_{K-1})^T$, $\mathbf{f} = -(D_1, \ldots, D_i, \ldots, \Upsilon_{K-1}^D)^T$, and \mathcal{M} is a tri-diagonal matrix of size $(K-1) \times (K-1)$ given by

$$\mathcal{M} = \begin{pmatrix} B_1 & A_1 & 0 & \dots & 0 & \dots & 0 \\ C_2 & B_2 & A_2 & & & & \vdots \\ 0 & \ddots & \ddots & \ddots & & 0 \\ \vdots & & C_i & B_i & A_i & & \vdots \\ 0 & & \ddots & \ddots & \ddots & 0 \\ \vdots & & & C_{K-2} & B_{K-2} & A_{K-2} \\ 0 & \dots & 0 & \dots & 0 & C_{K-1} & \Upsilon_{K-1}^B \end{pmatrix} . \tag{4.39}$$

The vector \mathbf{v} is found by computing $\mathbf{v} = \mathcal{M}^{-1}\mathbf{f}$. The function tridiag is used in MATLAB to compute \mathcal{M}^{-1} , given that \mathcal{M} is tri-diagonal.

Using central discretisations, the finite difference scheme corresponding to (4.23) for $i=2,\ldots,K-2$ is given by

$$\frac{c_{i+1}(\xi_i - \xi_{i-1}) - c_i(\xi_{i+1} - \xi_{i-1}) + c_{i-1}(\xi_{i+1} - \xi_i)}{\frac{1}{2}(\xi_{i+1} - \xi_{i-1})(\xi_{i+1} - \xi_i)(\xi_i - \xi_{i-1})} = (L)^2 \rho n_i c_i.$$
(4.40)

This equation can be rearranged to give

$$E_i c_{i+1} + F_i c_i + G_i c_{i-1} = 0, (4.41)$$

where

$$E_{i} = \frac{1}{(\xi_{i+1} - \xi_{i-1})(\xi_{i+1} - \xi_{i})}, \quad G_{i} = \frac{1}{(\xi_{i+1} - \xi_{i-1})(\xi_{i} - \xi_{i-1})}, \tag{4.42}$$

$$F_i = -\frac{2}{(\xi_{i+1} - \xi_i)(\xi_i - \xi_{i-1})} - (L)^2 \rho n_i.$$
(4.43)

The finite difference schemes corresponding to (4.23) for i = 1 and i = K - 1 are found by imposing the last two boundary conditions from (4.30) onto (4.41), and are given by

$$2E_1c_2 + F_1c_1 = 0,$$
 $E_{K-1} + F_{K-1}c_{K-1} + G_{K-1}c_{K-2} = 0,$ (4.44)

respectively. The solution to c_i is obtained by assembling (4.41) and (4.44) into the matrix-vector form $\mathcal{P}\mathbf{c} = \mathbf{h}$, where $\mathbf{c} = (c_1, \ldots, c_i, \ldots, c_{K-1})^T$, $\mathbf{h} = (0, 0, \ldots, 0, -E_{K-1})^T$, and \mathcal{P} is a tri-diagonal matrix of size $(K-1) \times (K-1)$ given by

$$\mathcal{P} = \begin{pmatrix}
F_1 + G_1 & E_1 & 0 & \dots & 0 & \dots & 0 \\
G_2 & F_2 & E_2 & & & & \vdots \\
0 & \ddots & \ddots & \ddots & & 0 \\
\vdots & & G_i & F_i & E_i & & \vdots \\
0 & & \ddots & \ddots & \ddots & 0 \\
\vdots & & & G_{K-2} & F_{K-2} & E_{K-2} \\
0 & & \dots & 0 & \dots & 0 & G_{K-1} & F_{K-1}
\end{pmatrix} .$$
(4.45)

The vector \mathbf{c} is found by using the function tridiag in MATLAB to compute $\mathbf{c} = \mathcal{P}^{-1}\mathbf{h}$.

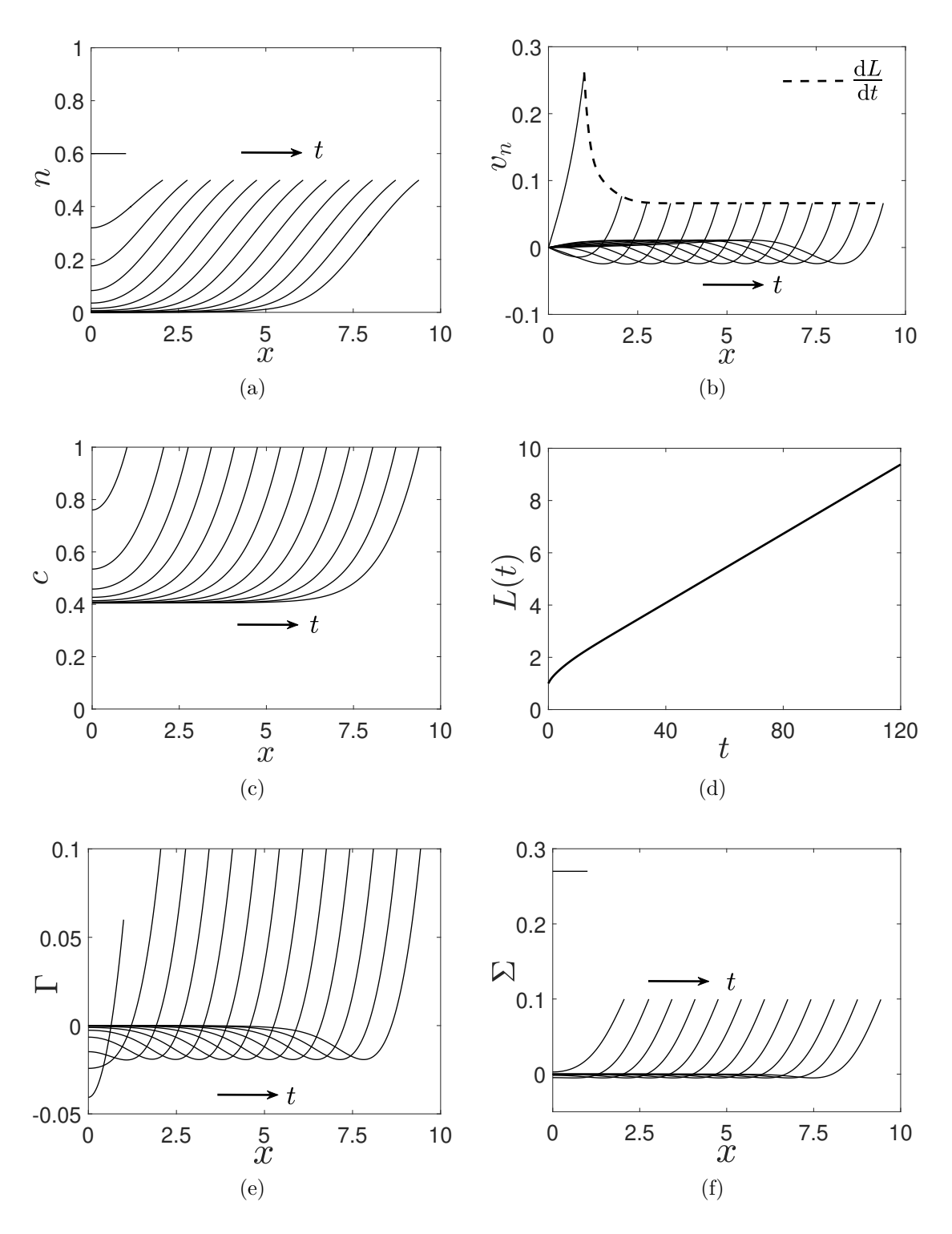


Figure 4.2: Numerical solutions of the PDE system from (4.12)-(4.17) for $\phi=0.3$. The black lines represent variable solutions at fixed times $t=0,\,10,\,\ldots,\,120$ and the arrows point in the direction of increasing time. The dashed line in (b) represents $v_n(L,\,t)$ and highlights the linear growth of L(t) observed in (d). The functions $\Gamma(n,\,c)$ and $\Sigma(n)$ are plotted in (e) and (f), respectively. Parameter values: $r_m=1,\,r_a=0.3,\,\kappa=1,\,\rho=1,\,\sigma=2$ and $n_0=0.6$.

4.3.2 Travelling-wave, steady-state and extinction-type solutions

In this subsection we fix $r_m = 1$, $r_a = 0.3$, $\sigma = 2$, $\kappa = 1$ and $\rho = 1$, and pay particular attention to three exemplar values of ϕ that generate travelling-wave and steady-state solutions, and solutions representing tumour extinction. The large-time behaviours of the solution types discussed here are independent of the initial conditions on n, and so for convenience we arbitrarily choose $n_i(x) = 0.6$.

In Fig. 4.2(a–d), we present numerical solutions for n, v_n , c and L when $\phi=0.3$, where we observe the emergence of forward-moving travelling waves and linear growth in L, after an initial period of transient growth from the initial cell distribution. The linear growth in L(t) is also highlighted in Fig. 4.2(b), where we see that L'(t) tends to a constant value for sufficiently large time. As seen in figure 4.2(a), there is a proliferating rim in the vicinity of the tumour edge, within which adequate levels of nutrient sustain the production of cells, i.e where $\Gamma>0$; see figure 4.2(e). Further into the tumour interior, the effects of cell death due to inadequate levels of nutrient dominate those of cell production, resulting in a region devoid of cells. In figure 4.2(c), the nutrient monotonically decreases away from the tumour edge due to its consumption by cells until it saturates to a constant value. The numerical results presented in figure 4.2 represent the continual growth of a tumour, and this motivates a travelling-wave analysis of the PDE model (4.12)–(4.17) which is provided in section 4.4.

In figure 4.3(a–d), we present numerical solutions for n, v_n , c and L when $\phi = 0.55$, where we observe the eventual formation of a spatially non-uniform steady state in n, v_n , c with L tending toward a constant value for sufficiently large time. For the steady-state solution in n represented by the dashed line in (a), there exists a region in the vicinity of the tumour edge in which $\Gamma > 0$, so that the net rate of cell production is positive; see figure 4.3(e). However, the dashed line in figure 4.3(b), representing the steady-state velocity is negative, indicating that cells in

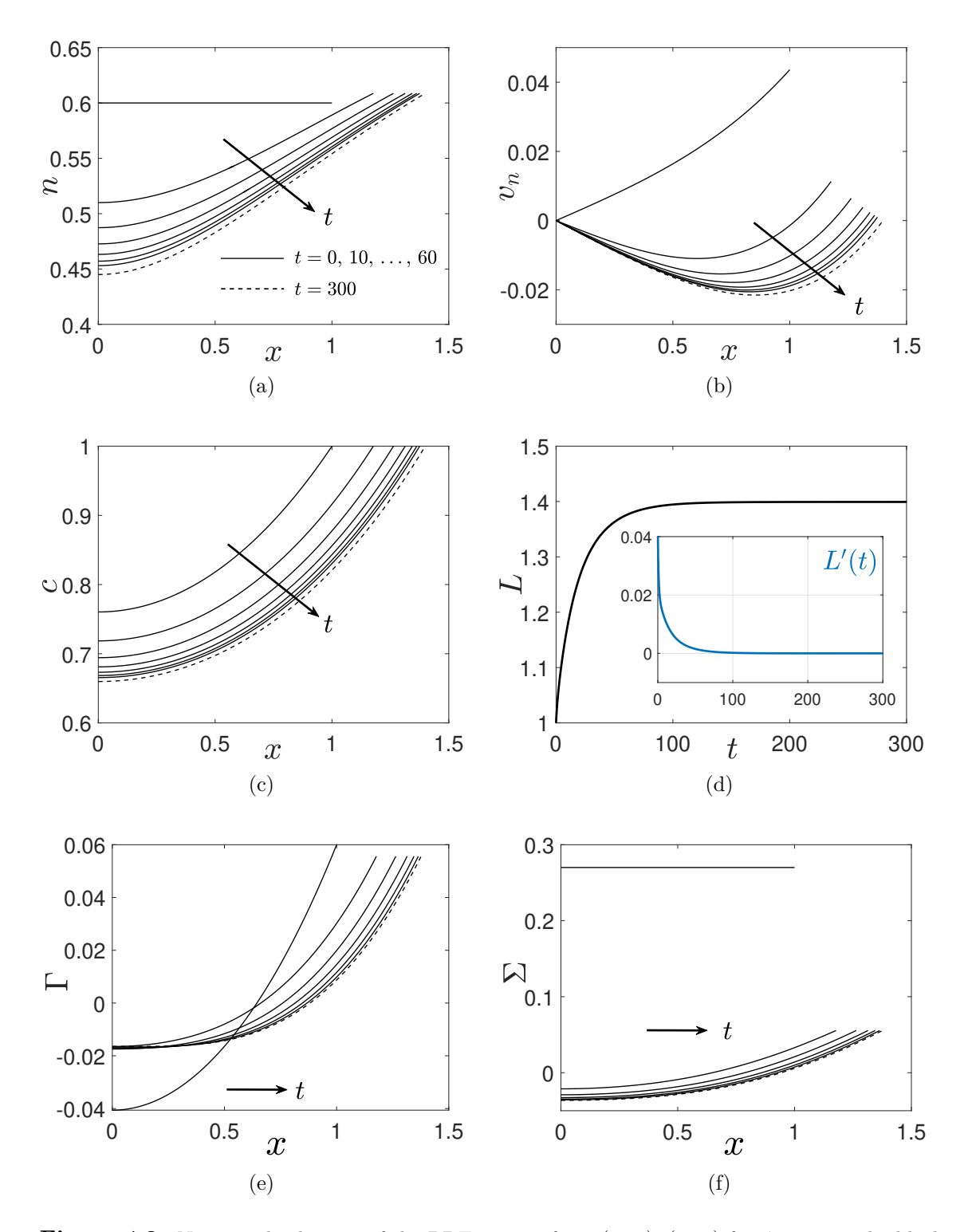


Figure 4.3: Numerical solutions of the PDE system from (4.12)-(4.17) for $\phi=0.55$. The black lines represent variable solutions at fixed times $t=0,10,\ldots,60$ and the arrows point in the direction of increasing time. The dashed lines in (a-c) represent the variables n, v_n and c for t=300, at which time L(t) is approximately constant. The functions $\Gamma(n,c)$ and $\Sigma(n)$ are plotted in (e) and (f), respectively. The inset in (d) represents L'(t) and highlights the steady-state nature of L(t). Parameter values: $r_m=1, r_a=0.3, \kappa=1, \rho=1, \sigma=2$ and $r_0=0.6$.

this region are moving toward the tumour core, where $\Gamma < 0$. This indicates that the PDE system (4.12)–(4.17) admits a steady-state solution if there is a balance between cell production and cell attraction when $\Sigma < 0$; see fig 4.3(f). This reasoning is substantiated by (4.12): Taking n to be only spatially dependent, the first term from (4.12) vanishes and the resultant equation states that the advection of n equals the net rate of cell growth, Γ .

In figure 4.4(a–d), we present numerical solutions for n, v_n and c on the fixed domain $\xi = x/L$ and L when $\phi = 0.8$. The inset in figure 4.4(d) shows $\log(L)$, which indicates L decays exponentially toward zero after an initial period of transient decay. These results represent tumour extinction, and we obtain criteria by which the PDE system (4.12)–(4.17) admits these extinction-type solutions in section 4.5.

4.4 Travelling-wave analysis

The results presented in figure 4.2 indicate the emergence of travelling waves of constant speed. In light of this, we assume that L evolves linearly for sufficiently large time, and employ travelling-wave analysis to obtain important quantities, such as the travelling wave speed, in terms of the model parameters.

The remainder of this section is constructed as follows. In subsection 4.4.1, we formulate the travelling-wave ODEs corresponding to the PDE system from (4.12)—(4.17). Following this, we present the numerical methods used to obtain solutions of the travelling-wave ODEs, and subsequently present some numerical results in subsection 4.4.3. In subsections 4.4.4 and 4.4.5, we construct asymptotic solutions of the travelling-wave ODEs in the limit of large and negligible nutrient diffusivity, respectively.

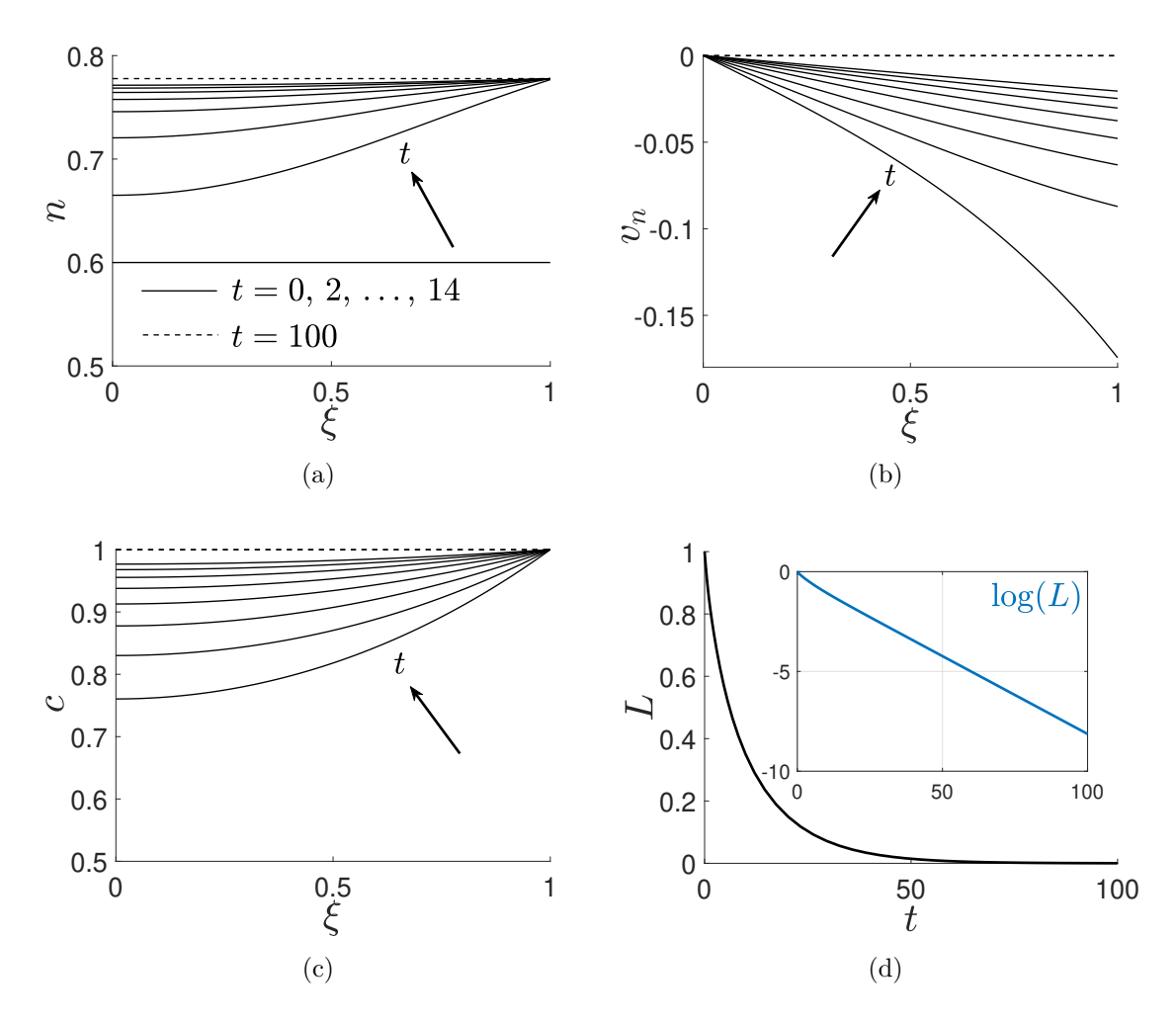


Figure 4.4: Numerical solutions of the PDE system from (4.12)-(4.17) for $\phi=0.8$. The black lines represent variable solutions at fixed times $t=0,\,2,\,\ldots,\,14$ and the arrows point in the direction of increasing time. The dashed lines in (a-c) represent the variables $n,\,v_n$ and c for t=100, at which time L(t) is approximately zero. The inset in (d) represents $\log(L)$ and highlights the exponential decay of L(t). Parameter values: $r_m=1,\,r_a=0.3,\,\kappa=1,\,\rho=1,\sigma=2$ and $n_0=0.6$.

4.4.1 Formulation

We write the PDE system from (4.12)–(4.17) in terms of the variable $\overline{L}(t) = L(t)\sqrt{\kappa}$ and coordinate $z = \sqrt{\kappa}x - \overline{L}(t) \sim \sqrt{\kappa}x - Ut$, where $z \in (-\infty, 0]$. Here, U is the scaled wave speed, i.e. the speed of travelling waves observed in a simulation of the PDE system (4.12)–(4.17) is $U/\sqrt{\kappa}$. Setting $n \equiv n(z)$, $v_n \equiv v(z)/\sqrt{\kappa}$ and $c \equiv c(z)$

we obtain

$$-U\frac{\mathrm{d}n}{\mathrm{d}z} + \frac{\mathrm{d}}{\mathrm{d}z}(nv) = \Gamma(n, c), \tag{4.46}$$

$$\frac{\mathrm{d}}{\mathrm{d}z} \left(n \frac{\mathrm{d}v}{\mathrm{d}z} \right) - \frac{\mathrm{d}}{\mathrm{d}z} \left[n \Sigma(n) \right] - \frac{nv}{1-n} = 0, \tag{4.47}$$

$$\frac{\mathrm{d}^2 c}{\mathrm{d}z^2} = \beta nc,\tag{4.48}$$

$$\frac{\mathrm{d}v}{\mathrm{d}z}\Big|_{z=0} = \Sigma(n), \quad v(0) = U, \quad c(0) = 1, \quad \lim_{z \to -\infty} \left(v(z), \frac{\mathrm{d}c}{\mathrm{d}z}\right) = 0, \quad (4.49)$$

where $\beta = \rho/\kappa$. We now develop the methods used to obtain numerical solutions of (4.46)–(4.49).

4.4.2 Numerical Methods

In this section, we present the numerical methods used to find n(z), v(z), c(z) and U from (4.46)–(4.49). For numerical purposes, we express (4.46)–(4.49) as a system of five, first order ODEs by introducing the variables h(z) = v'(z) and g(z) = c'(z) where $' \equiv d/dz$. We obtain

$$n'(z) = \frac{\Gamma(n, c) - nh}{v - U}, \qquad v'(z) = h,$$
 (4.50)

$$h'(z) = \frac{v}{1-n} + \frac{(F(n) - h)(\Gamma(n, c) - nh)}{n(v - U)},$$
(4.51)

$$c'(z) = g, \qquad g'(z) = \beta nc, \tag{4.52}$$

$$v'(0) = \Sigma(n_{\infty}), \quad v(0) = U, \quad c(0) = 1, \quad \lim_{z \to -\infty} \left[v(z), g(z) \right] = 0,$$
 (4.53)

where $F=\frac{\mathrm{d}}{\mathrm{d}n}[n\Sigma(n)]$. This system is computationally singular at z=0 due to the boundary condition v(0)=U. We therefore consider the leading edge of the wavefront to be $z=-\delta$, where δ is chosen to be sufficiently small that the solution converges. We numerically integrate (4.50)–(4.53) on the truncated domain $z\in[-M,-\delta]$, and must therefore obtain asymptotically appropriate boundary conditions at the points $z=-\delta$ and z=-M.

The conditions at $z=-\delta$ are found by expanding the dependent variables from (4.50)–(4.53) around z=0. We obtain as $z\to 0$

$$n \sim n_{\infty} + n'(0)z, \quad v \sim U + \Sigma(n_{\infty})z, \quad h \sim \Sigma(n_{\infty}) + h'(0)z,$$

 $c \sim 1 + g(0)z, \quad g \sim g(0) + \beta n_{\infty}z.$ (4.54)

The values of n'(0) and h'(0) are found by taking the limit as $z \to 0$ of the first from (4.50) and (4.51) via L'Hôpital's rule, and subsequently summing them. We have

$$n'(0) = \frac{g(0)\Gamma_c - n_{\infty}h'(0)}{2\Sigma(n_{\infty}) - \Gamma_n},$$
(4.55)

$$h'(0) = \frac{2\Sigma(n_{\infty}) - \Gamma_n}{\Sigma(n_{\infty}) + F(n_{\infty}) - \Gamma_n} \left(\frac{U}{1 - n_{\infty}} + \frac{\Gamma_c g(0) \left[F(n_{\infty}) - \Sigma(n_{\infty}) \right]}{n_{\infty} \left[2\Sigma(n_{\infty}) - \Gamma_n \right]} \right), \tag{4.56}$$

where $\Gamma_n = \frac{\partial \Gamma}{\partial n}(n_{\infty}, 1)$ and $\Gamma_c = \frac{\partial \Gamma}{\partial c}(n_{\infty}, 1)$. The value of g(0) is unknown and must be determined numerically as part of the solution.

The appropriate boundary conditions at z = -M are found by analysing (4.46)–(4.49) in the limit as $z \to -\infty$. Numerical simulations of the PDE system (4.12)–(4.17) indicate that $n, v \to 0$ and $c \to c_0$ as $z \to -\infty$, where c_0 is an unknown constant. We therefore introduce the perturbations to these values valid as $z \to -\infty$,

$$n \sim n_0(z), \qquad v \sim v_0(z), \qquad c \sim c_0 + c_1(z)$$
 (4.57)

such that $|n_0|$, $|v_0|$, $|c_1| \ll 1$ satisfy the system

$$\frac{\mathrm{d}n_0}{\mathrm{d}z} = Kn_0,\tag{4.58}$$

$$\frac{\mathrm{d}}{\mathrm{d}z} \left(n_0 \frac{\mathrm{d}v_0}{\mathrm{d}z} \right) + 2\phi n_0 \frac{\mathrm{d}n_0}{\mathrm{d}z} - n_0 v_0 = 0, \tag{4.59}$$

$$\frac{\mathrm{d}^2 c_1}{\mathrm{d}z^2} = \beta n_0 c_0,\tag{4.60}$$

where $K = \frac{1}{U}[r_a\sigma - c_0(r_m + r_a)]$. The solutions of this system are

$$n_0 = \mathcal{N}e^{Kz}, \quad v_0 = \mathcal{V}e^{\frac{z}{2}(\sqrt{4+K^2}-K)} - \frac{2\phi K \mathcal{N}e^{Kz}}{2K^2-1}, \quad c_1 = \frac{\beta c_0 \mathcal{N}e^{Kz}}{K^2},$$
 (4.61)

where \mathcal{N} and \mathcal{V} are unknown and must be determined numerically as part of the

solution. The asymptotic representations for h and g as $z \to -\infty$ are obtained via h = v' and g = c'.

Thus far, we have developed a method to numerically solve (4.46)–(4.49). We integrate the system of five first order ODEs from (4.50)–(4.53) using the function bvp5c in MATLAB. We use the asymptotic representations described above as $z \to 0$ and $z \to -\infty$ as boundary conditions at $z = -\delta$ and z = -M, respectively. The values of the five unknown parameters $(U, g(0), \mathcal{N}, \mathcal{V}, c_0)$ are obtained as eigenvalues in bvp5c. The function bcp5c requires an initial approximation of the solutions satisfying (4.50)–(4.53) in order to converge toward a feasible solution. For this, we first compute the travelling-wave solutions n(x, t), v(x, t) and c(x, t) from the PDE system (4.12)–(4.17) for a sufficiently large fixed value of t. These solutions are then fitted to curves using the built-in application curve fitter in MATLAB. These fitted curves can then be used as initial approximations of the solutions of (4.50)–(4.53) for a fixed set of parameters. The method of parameter continuation is then used to obtain the solutions for other parameter sets.

4.4.3 Numerical results

Using the numerical methods presented in the prior subsection, we now investigate how varying the natural cell density ϕ , and compound parameter $\beta = \rho/\kappa$ (where ρ is proportional to the ratio between the nutrient consumption rate and nutrient diffusivity), affect the cell volume fraction n(z) and its associated velocity v(z).

In figure 4.5, we present some numerical solutions for n(z), v(z) and c(z) using the methods described in subsection 4.4.2 for various values of ϕ . As seen in figure 4.5(a), the cell volume fraction in regions (i) and (ii) increase and decrease as ϕ increases, respectively. In region (i), n(z) increases with ϕ to attain a higher cell density, as expected. In region (ii) however, n(z) is unable to increase toward ϕ due to an insufficient level of nutrient, see region (ii) in figure 4.5(c). To increase toward ϕ , cells therefore migrate toward the region of higher cell density (ii) under

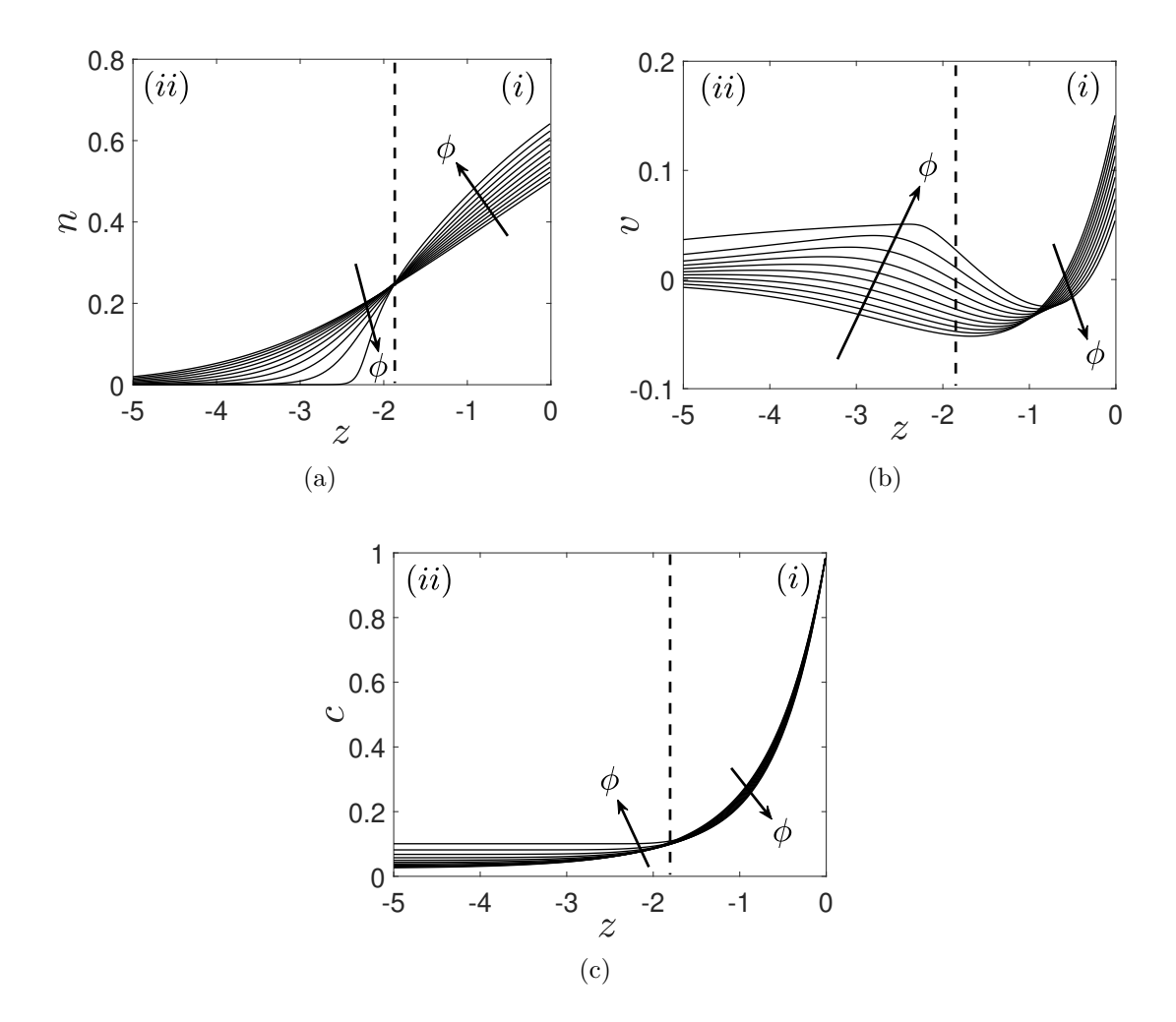


Figure 4.5: Numerical solutions for n(z), v(z) and c(z) from the travelling-wave ODE system (4.46)–(4.49) for various values of ϕ spaced uniformly over the interval $\phi = [0.1, 0.5]$. The arrows point in the increasing direction of ϕ . The regions (i) and (ii) in (a, b) indicate where n(z) increase and decrease with ϕ , respectively. Parameter values: $r_m = 1$, $r_a = 0.1$, $\sigma = 2$, $\beta = 5$ and M = 20.

the action of $\Sigma(n)$. This migration of cells from region (ii) to (i) is highlighted by the positivity of v(z) in region (ii), as observed in figure 4.5(b). More concisely, figure 4.5(a) suggests that increasing the natural cell density ϕ can sharpen the interface between the proliferating rim and the necrotic core. In figure 4.5(b), we also observe two qualitatively different behaviours in v(z). For smaller values of ϕ , v(z) decreases away from the wave-front where it becomes and remains negative due to attractive forces governed by Σ when n is small. However, for larger values of ϕ , v(z) decreases away from the wave front becoming negative, before increasing to become positive in the tumour core. This positive region of v(z) arises due to the forces generated by cells migrating up gradients of n being greater than those driving tumour expansion.

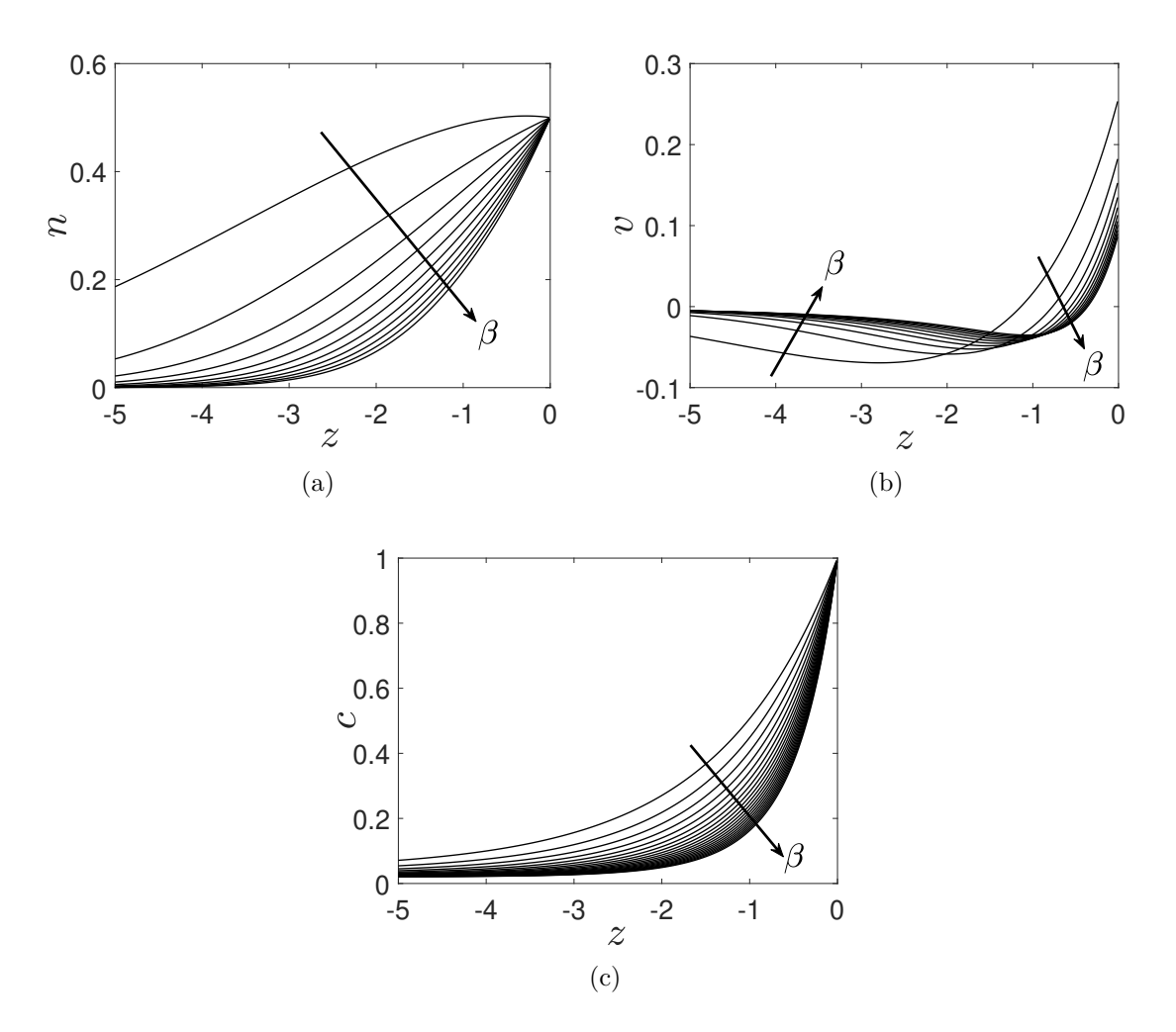


Figure 4.6: Numerical solutions of n(z), v(z) and c(z) from the travelling-wave ODE system (4.46)–(4.49) for various values of β spaced uniformly over the interval $\beta = [1, 5]$, respectively. The arrows point in the increasing direction of β . Parameter values: $r_m = 1$, $r_a = 0.1$, $\sigma = 2$, $\phi = 0.1$ and M = 20.

In figure 4.6, some numerical solutions for n(z), v(z) and c(z) are presented for various values of β . Given that increasing β corresponds to decreasing nutrient diffusivity, it is not surprising that the level of nutrient within the tumour reduces as β increases, as seen in figure 4.6(c). Consequently, the cell volume fraction decreases as β increases in figure 4.6(a), due to a decreasing net rate of cell production. We note that the effects of varying β are further investigated in subsections 4.4.4 and 4.4.5, where an asymptotic analysis of the travelling-wave ODEs from (4.46)–(4.49) when $\beta \ll 1$ and $\beta \gg 1$ is provided, respectively.

To quantify changes to the cell volume fraction, we follow Lemon and King

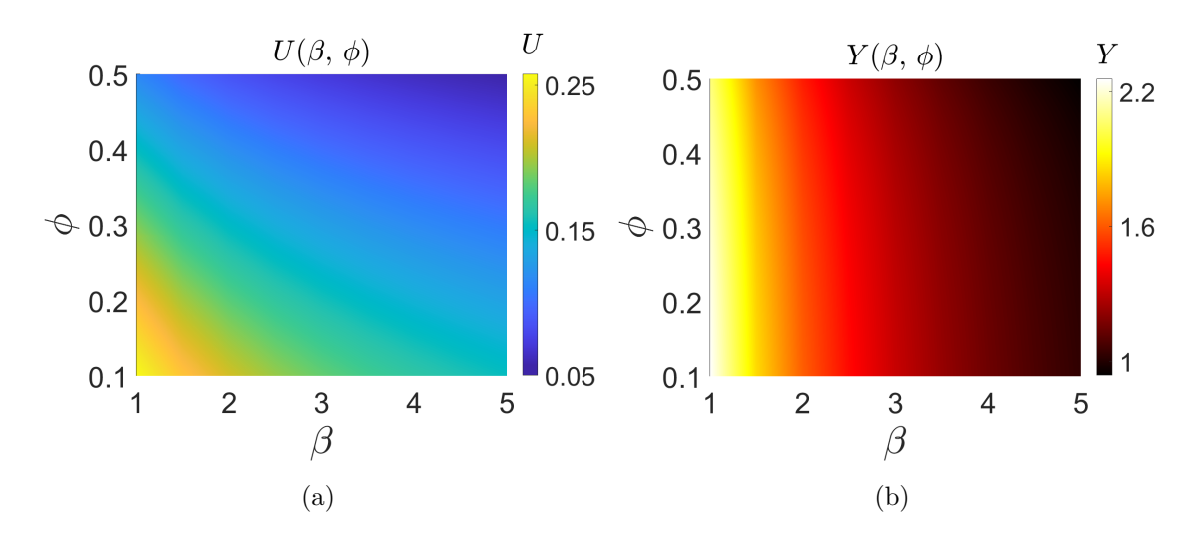


Figure 4.7: Numerical solution of the wave speed $U(\beta, \phi)$ (a) and the quantity $Y(\beta, \phi)$ (b) from (4.62) computed from numerical solutions of n(z). Parameter values: $\phi = 0.1$, $r_a = 0.1$, $\sigma = 2$ and M = 20.

(2007b) and define the cell yield

$$Y = \int_{-\infty}^{0} n(z) dz. \tag{4.62}$$

This quantity measures the amount of cells within a tumour, and can be expressed as a function of the model parameters. In figure 4.7(b) we present the cell yield $Y(\beta, \phi)$, where we observe that the cell yield appears to have little dependence on ϕ , and is largely determined by the value of β . This suggests that an increase in the natural cell density can serve to distribute the available cells closer to the tumour edge, as seen in figure 4.5(a). Whilst ϕ has little influence on the value of the cell yield, it can significantly effect the tumour growth speed, as shown by the function $U(\beta, \phi)$ in figure 4.5(b).

4.4.4 Asymptotic analysis for $\beta \ll 1$

In this subsection, we construct asymptotic solutions of the travelling-wave system from (4.46)–(4.49) valid when $\beta \ll 1$ (so that either $\rho \ll 1$ or $\kappa \gg 1$). Physically, this corresponds to the case when either the nutrient rapidly diffuses through the tumour or the value of the cell-liquid drag is large. By first scaling z with β , we consider a region in which $z = \mathcal{O}(\beta^{-1/2})$ representing the tumour interior, and then a

region representing the tumour rim in which $z = \mathcal{O}(1)$. By matching the expansions valid in each region, we obtain composite asymptotic solutions of (4.46)–(4.49) valid on $z \in (-\infty, 0]$ for $\beta \ll 1$.

The region $z = \mathcal{O}(\beta^{-1/2})$

For the region $z = \mathcal{O}(\beta^{-1/2})$ representing the tumour interior, we introduce the variables $\zeta = z\sqrt{\beta}$ and $\nu = v/\sqrt{\beta}$ with $(\zeta, \nu) = \mathcal{O}(1)$, so that (4.46)–(4.49) provides

$$\Gamma(n, c) = 0, \qquad \nu = \frac{n-1}{n} \frac{\mathrm{d}}{\mathrm{d}\zeta} \left[n\Sigma(n) \right], \qquad \frac{\mathrm{d}^2 c}{\mathrm{d}\zeta^2} = nc,$$
 (4.63)

to leading order in β . As seen from (4.63), the cell volume fraction in this interior region is now only dependent on the effects of nutrient limitation and the net rate of cell growth, but not the effects of cellular attraction/repulsion governed by $\Sigma(n)$. The first from (4.63) allows n to be expressed in terms of c, i.e.

$$n = 1 - \frac{r_a(\sigma - c)}{r_m c},\tag{4.64}$$

so that the third from (4.63) becomes

$$\frac{\mathrm{d}^2 c}{\mathrm{d}\zeta^2} = c \left[1 - \frac{r_a(\sigma - c)}{r_m c} \right],\tag{4.65}$$

which is coupled to the condition $\lim_{\zeta \to -\infty} \frac{\mathrm{d}c}{\mathrm{d}\zeta} = 0$. We have that

$$n(\zeta) = k_1 - \frac{r_a \sigma}{r_m \left[A e^{\sqrt{k_1} \zeta} + k_2 \right]}, \qquad c(\zeta) = A e^{\sqrt{k_1} \zeta} + k_2, \tag{4.66}$$

$$v(\zeta) = -\frac{r_a \, \sigma + k_2 \, r_m + A \, r_m \, e^{\sqrt{k_1} \, \zeta} - k_1 \, k_2 \, r_m - A \, k_1 \, r_m \, e^{\sqrt{k_1} \, \zeta}}{k_1 \, k_2 \, r_m - r_a \, \sigma + A \, k_1 \, r_m \, e^{\sqrt{k_1} \, \zeta}} \times \frac{\mathrm{d}}{\mathrm{d}\zeta} \left(-\frac{\left(k_1 - \frac{r_a \, \sigma}{r_m \left(k_2 + A \, e^{\sqrt{k_1} \, \zeta}\right)}\right)^2 \left(\phi - k_1 + \frac{r_a \, \sigma}{r_m \left(k_2 + A \, e^{\sqrt{k_1} \, \zeta}\right)}\right)}{\frac{r_a \, \sigma}{r_m \left(k_2 + A \, e^{\sqrt{k_1} \, \zeta}\right)} - k_1 + 1} \right), \tag{4.67}$$

where $k_1 = 1 + r_a/r_m$, $k_2 = r_a \sigma/(r_m + r_a)$ and A is a matching constant. We note that $\lim_{\zeta \to -\infty} n(\zeta) = 0$, which confirms the presence of a necrotic core within the

tumour. Furthermore, we see that $\lim_{\zeta \to -\infty} c(\zeta) = k_2$, indicating that the level of nutrient present in the tissue core is only dependent on parameters related to cell growth and cell death.

The region $z = \mathcal{O}(1)$

For the region in which $z = \mathcal{O}(1)$ representing the tumour edge we set n := N(z) and v := V(z). To leading order in β , (4.48) provides

$$\frac{\mathrm{d}^2 c}{\mathrm{d}z^2} = 0,\tag{4.68}$$

which is coupled to the conditions c(0) = 1 and $\lim_{z \to -\infty} c(z) = 0$, so that $c \sim 1$ and the tumour is therefore nutrient-rich in this region. The equations governing the quantities $N, V = \mathcal{O}(1)$ in the $z = \mathcal{O}(1)$ region are hence

$$-U\frac{\mathrm{d}N}{\mathrm{d}z} + \frac{\mathrm{d}}{\mathrm{d}z}(NV) = \Gamma(N, 1),\tag{4.69}$$

$$\frac{\mathrm{d}}{\mathrm{d}z} \left(N \frac{\mathrm{d}V}{\mathrm{d}z} \right) - \frac{\mathrm{d}}{\mathrm{d}z} \left[N \Sigma(N) \right] - \frac{NV}{1 - N} = 0, \tag{4.70}$$

$$V(0) = U,$$
 $V'(0) = \Sigma(n_{\infty}),$ $\lim_{z \to -\infty} V(z) = 0,$ $\lim_{z \to -\infty} N(z) = \Theta,$ (4.71)

where $\Theta = 1 - r_a(\sigma - 1)/r_m$. This system of ODEs is identical to those analysed in section 3.4 and numerical methods are developed in subsection 3.4.3 to obtain its solution.

Matching conditions and composite solutions

We now obtain composite solutions for n(z), v(z), c(z) and U over the entire domain to leading order in β . Firstly, we have that $\lim_{\zeta\to 0} c(\zeta) = 1$ which determines $A = 1 - k_2$. We also have that $\lim_{z\to -\infty} N(z) = \lim_{\zeta\to 0} n(\zeta) = \Theta$, so that composite

solutions when $\beta \ll 1$ are given by

$$n(z) \sim N(z) + k_1 - \frac{r_a \sigma}{r_m \left[(1 - k_2) e^{\sqrt{k_1 \beta} z} + k_2 \right]} - \Theta,$$
 (4.72)

$$c(z) \sim (1 - k_2)e^{\sqrt{k_1\beta}z} + k_2$$
 (4.73)

$$v(z) \sim V(z), \qquad U \sim V(0),$$
 (4.74)

where N(z) and V(z) are calculated numerically using the methods presented in subsection 3.4.3. Given that $v = \mathcal{O}(\beta^{1/2})$ and $v = \mathcal{O}(1)$ in the core region $z = \mathcal{O}(\beta^{-1/2})$ and rim region $z = \mathcal{O}(1)$ respectively, the composite leading order expansion from (4.74) depend only on solutions for V(z) from the region $z = \mathcal{O}(1)$. Therefore, to obtain the growth speed of the tumour when $\beta \ll 1$, it suffices to solve the nutrient-rich travelling-wave ODEs from (4.69)–(4.71), an analysis of which was presented in section 3.4.

In figure 4.8, we compare the numerical solution for n and c when obtained by solving the PDE system from (4.12)–(4.17) for $\beta = 0.001$ against their respective asymptotic solutions from (4.72) and (4.73). The travelling-wave solutions n(z) and c(z) are obtained from the PDE system from (4.12)–(4.17) by computing n(x, t) and c(x, t) for a sufficiently large fixed t. Overall, a very good agreement between the numerical and asymptotic solutions is observed. From figure 4.8(a), the cell density is negligible in the tumour core; despite this, the nutrient-limited region over which n(z) decreases toward this necrotic core will provide a substantial contribution to the total cell yield Y, as defined by the integral from (4.62).

4.4.5 Asymptotic analysis for $\beta \gg 1$

In this subsection, we obtain asymptotic solutions of the system from (4.46)–(4.49) valid when $\beta \gg 1$ (so that either $\rho \gg 1$ or $\kappa \ll 1$) Physically, this corresponds to the case when either the nutrient diffuses slowly through the tumour, or the cell-liquid drag is negligible. For clarity, we set $\beta = 1/\varepsilon$ such that $\varepsilon \ll 1$.

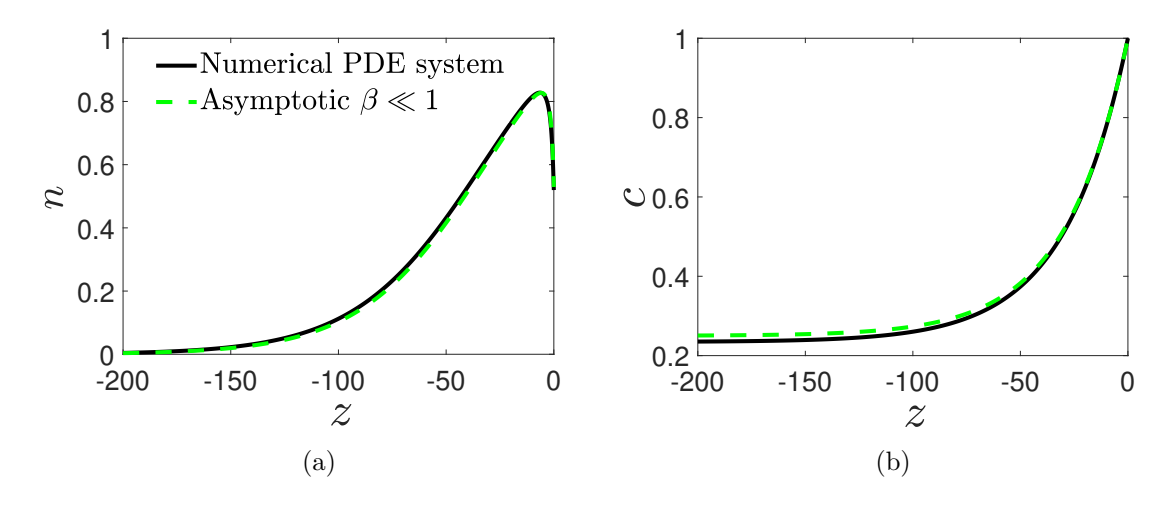


Figure 4.8: Numerical solution (solid black line) of the PDE system from (4.12)–(4.17) and asymptotic solution (dashed green line) from (4.72) and (4.73) for (a) n and (b) c for $\beta=0.001$. Parameter values: $r_m=1, r_a=0.2, \sigma=1.5, \phi=0.2$ and $n_0=0.6$.

When $z = \mathcal{O}(1)$, we initially adopt an algebraic expansion of n and c in powers of ε , so that (4.48) provides n = 0 to leading order in ε . This indicates that n is exponentially small, i.e. $n = o(\varepsilon^{\iota})$ for any $\iota > 0$. In view of this, (4.48) provides

$$\frac{\mathrm{d}^2 c}{\mathrm{d}z^2} = 0,\tag{4.75}$$

to leading order in ε , so that $c = c_0$, where $c_0 = \mathcal{O}(1)$ is a constant determined by the scaling z with $\varepsilon^{\frac{1}{2}}$, as follows.

We introduce the variables $\zeta = z/\sqrt{\varepsilon}$, $V(\zeta) = v/\sqrt{\varepsilon}$, $Q = U/\sqrt{\varepsilon}$ and set $n := N(\zeta)$ and $c := C(\zeta)$, with $(\zeta, V, Q, N, C) = \mathcal{O}(1)$. To leading order in ε , (4.46)–(4.49) provides

$$N'(\zeta) = \frac{\Gamma(N,C) - N\Sigma(N)}{V - Q},\tag{4.76}$$

$$V'(\zeta) = \Sigma(N), \tag{4.77}$$

$$C'(\zeta) = G \tag{4.78}$$

$$G'(\zeta) = NC, \tag{4.79}$$

$$V(0) = Q, \quad C(0) = 1, \quad \lim_{\zeta \to -\infty} (N(\zeta), G(\zeta), V(\zeta)) = 0,$$
 (4.80)

where $' \equiv \frac{d}{d\zeta}$ and G = C'. We note that, the boundary conditions from the full

system (4.46)–(4.49) are satisfied as $\xi \to -\infty$, which indicates solutions to (4.76)–(4.80) are uniformly valid for all z. We solve (4.76)–(4.80) numerically via a shooting method, with initial data specified at the wave front, $\zeta = 0$. This system is computationally singular at $\xi = 0$ due to the boundary condition V(0) = Q. We therefore consider the leading edge of the wavefront to be $\xi = -\delta$, where δ is chosen to be sufficiently small that the solution converges. We numerically integrate (4.76)–(4.80) on the truncated domain $\xi \in [-M, -\delta]$, and must therefore obtain asymptotically appropriate boundary conditions at the points $\xi = -\delta$ and $\xi = -M$.

The initial data at $\zeta=-\delta$ is found by expanding the dependent variables around $\zeta=0$, so that as $\zeta\to 0$ we have

$$N \sim n_{\infty} + N'(0)\zeta$$
, $V \sim Q + \Sigma(n_{\infty})\zeta$, $C \sim 1 + G(0)\zeta$, $G \sim G(0) + n_{\infty}\zeta$, (4.81)

The value of N'(0) is found explicitly by taking the limit as $\zeta \to 0$ via L'Hôpital's rule. We have,

$$N'(0) = \frac{G(0)\Gamma_C(n_{\infty}, 1)}{\Sigma(n_{\infty}) - \Gamma_N(n_{\infty}, 1) + F(n_{\infty})},$$
(4.82)

such that $\Gamma_N = \frac{\partial \Gamma}{\partial N}$, $\Gamma_C = \frac{\partial \Gamma}{\partial C}$ and $F(N) = \frac{\mathrm{d}}{\mathrm{d}N}[N\Sigma(N)]$. The values of Q and G(0) are unknown and must be determined as part of the problem.

The appropriate boundary conditions at $\xi = -M$ are found by analysing (4.76)—(4.80) in the limit as $\xi \to -\infty$, where $N, V, G \to 0$ and $C \to C_0$, such that C_0 is an unknown constant. We therefore introduce the perturbations $N \sim N_0$, $V \sim V_0$, $G \sim G_0$ and $C \sim C_0 + C_1$ such that $|N_0|$, $|V_0|$, $|G_1|$, $|C_1| \ll 1$ satisfy the system

$$N_0' = KN_0, \qquad V_0' = -\phi N_0, \qquad C_1' = G_0, \qquad G_0' = N_0 C_0$$
 (4.83)

where $K = \frac{1}{Q} [r_a \sigma - C_0(r_m + r_a)]$. The solutions of this system are

$$N_0 = \mathcal{N}_0 e^{Kz}, \qquad V_0 = -\frac{\phi \mathcal{N}_0 e^{Kz}}{K}, \qquad C_1 = \frac{C_0 \mathcal{N}_0 e^{Kz}}{K^2}, \qquad G_1 = \frac{C_0 \mathcal{N}_0 e^{Kz}}{K}$$
 (4.84)

so that as $\xi \to -\infty$ we have

$$V \sim -\frac{\phi N}{K}, \qquad C \sim C_0 + \frac{C_0 N}{K^2}, \qquad G \sim \frac{C_0 N}{K}.$$
 (4.85)

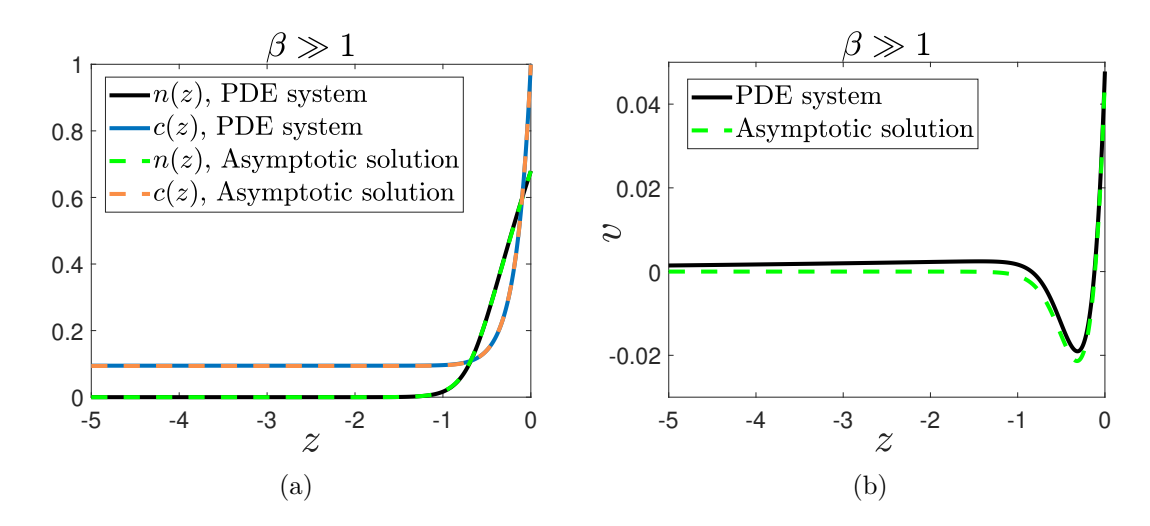


Figure 4.9: Numerical solution of the PDE system from (4.12)-(4.17) and asymptotic solutions from (4.76)-(4.80) for $\beta=50$. Parameter values: $r_m=2, r_a=0.5, \sigma=1.1, \phi=0.4, n_0=0.6$ and M=-50.

These relationships are used as boundary conditions at $\xi = -M$.

Using the function ode45 in MATLAB, we numerically integrate (4.76)–(4.80) from $\zeta = -\delta$ to $\zeta = -M$ for various values of Q, G(0) and G_0 using the initial data from (4.81) at $\zeta = -\delta$. Using the function fminsearch in MATLAB, we obtain the values of Q, G(0) and G_0 such that the boundary conditions at $\zeta = -M$ are satisfied. From this, we are able to obtain N, V, G and G and the corresponding value of G.

In figure 4.9, we compare the numerical solution for n, v and c when obtained by solving the PDE system from (4.12)–(4.17) for $\beta = 50$ against their respective asymptotic solutions N, V and C from (4.76)–(4.80). The travelling-wave solutions n(z), v(z) and c(z) are obtained from the PDE system from (4.12)–(4.17) as described in subsection 4.4.4. We overcome numerical problems experienced when solving the PDE system, which arise in the boundary-layer, by employing a non-uniform mesh with a concentrated number of mesh points in the vicinity of the tumour edge; see section 4.3.1. Overall, a very good agreement between the numerical and asymptotic solutions is observed, despite only a moderately large value of β being used.

4.5 Criteria for extinction-type solutions

The numerical results presented in section 4.3.2 illustrate that as the natural cell density ϕ increases, solutions of the PDE system (4.12)–(4.17) transition from travellingwave, to steady-state and then extinction-type such that $L \to 0$. The former two solution types correspond to the formation of a non-zero population of cells; however, the latter corresponds to tumour extinction, and we now obtain criteria by which the PDE system (4.12)–(4.17) admits these extinction-type solutions.

The numerical solutions presented in section 4.3.2 suggest the criteria for extinctiontype solutions can be sought by identifying the bifurcation between steady-state solutions and extinction-type solutions. To obtain this bifurcation criteria, we first present the steady-state system of ODEs resulting from the PDE system (4.12)– (4.17). Assuming that $n \sim n(x)$, $v_n \sim v_n(x)$, $c \sim c(x)$ and that $L \sim L_{\infty}$ for $t \gg 1$ where L_{∞} is constant, the PDE system from (4.12)–(4.73) provides

$$\frac{\partial}{\partial x}(nv_n) = \Gamma(n, c), \qquad 0 < x < L_{\infty}, \qquad (4.86)$$

$$\frac{\partial}{\partial x} \left(n \frac{\partial v_n}{\partial x} \right) - \frac{\partial}{\partial x} \left[n \Sigma(n) \right] - \kappa \frac{n v_n}{1 - n} = 0, \qquad 0 < x < L_{\infty}, \tag{4.87}$$

$$\frac{\partial^2 c}{\partial x^2} = \rho n c, \qquad 0 < x < L_{\infty}, \qquad (4.88)$$

$$\frac{\mathrm{d}v_n}{\mathrm{d}x}\Big|_{x=L_{\infty}} = \Sigma(n), \quad v_n(L_{\infty}) = 0, \quad c(L_{\infty}) = 1, \quad v_n(0) = 0, \qquad \frac{\mathrm{d}c}{\mathrm{d}x}\Big|_{x=0} = 0.$$
(4.89)

Numerical solutions of the PDE system (4.12)–(4.17) suggest that L_{∞} decreases toward zero as the bifurcation between steady-state and extinction-type solutions is approached, and we hence assume that this bifurcation point lies at $L_{\infty} = 0$. In view of this, we obtain criteria for extinction-type solutions by analysing the system of steady-state ODEs (4.86)–(4.89) in the limit $L_{\infty} \to 0$.

4.5.1 Asymptotic analysis of the steady-state ODEs as $L_{\infty} \rightarrow 0$

In this subsection, we analyse the system of steady-state ODEs from (4.86)–(4.89) in the limit $L_{\infty} \to 0$ to obtain the bifurcation between steady-state and extinction-type solutions.

For convenience, we first scale $x \in [0, L_{\infty}]$ with L_{∞} as $X = x/L_{\infty}$, so that $X \in [0, 1]$ and (4.86)–(4.89) provides

$$\frac{\partial}{\partial X}(nv_n) = L_{\infty}\Gamma(n, c), \qquad 0 < X < 1, \qquad (4.90)$$

$$\frac{\partial}{\partial X} \left(n \frac{\partial v_n}{\partial X} \right) - L_{\infty} \frac{\partial}{\partial X} \left[n \Sigma(n) \right] - L_{\infty}^2 \kappa \frac{n v_n}{1 - n} = 0, \qquad 0 < X < 1, \tag{4.91}$$

$$\frac{\partial^2 c}{\partial X^2} = L_{\infty}^2 \rho n c, \qquad 0 < X < 1, \qquad (4.92)$$

$$\frac{\mathrm{d}v_n}{\mathrm{d}X}\bigg|_{X=1} = L_{\infty}\Sigma(n), \quad v_n(1) = 0, \quad c(1) = 1, \quad v_n(0) = 0, \quad \frac{\mathrm{d}c}{\mathrm{d}X}\bigg|_{X=0} = 0. \quad (4.93)$$

Guided by numerical solutions of the PDE system (4.12)–(4.17) when $L_{\infty} \ll 1$, we introduce the perturbations

$$n \sim n_0(X) + \epsilon^{\alpha} n_1(X), \quad v_n \sim \epsilon^{\eta} v_0(X), \quad c \sim c_0(X) + \epsilon^{\gamma} c_1(X), \quad L_{\infty} \sim \epsilon \ell, \quad (4.94)$$

where α , η and γ are positive constants and $\epsilon \to 0^+$. Here, ϵ is a small parameter which will subsequently be determined as a function of the model parameters via an appropriate dominant balance, thereby identifying a relationship between the model parameters ensuring that $L_{\infty} \to 0$.

We first substitute the perturbations from (4.94) into (4.90)-(4.92) to obtain

$$\epsilon^{\eta} \frac{\partial}{\partial X}(n_0 v_0) = \epsilon \ell \Gamma(n_0, c_0), \tag{4.95}$$

$$\epsilon^{\eta} \frac{\partial}{\partial X} \left(n_0 \frac{\partial v_0}{\partial X} \right) - \ell \epsilon \frac{\partial}{\partial X} \left[n_0 \Sigma(n_0) \right] - \epsilon^{2+\eta} \ell^2 \kappa \frac{n_0 v_0}{1 - n_0} = 0, \tag{4.96}$$

$$\frac{\partial^2 c_0}{\partial X^2} = \epsilon^2 \ell \rho n_0 c_0. \tag{4.97}$$

To leading order in ϵ , we integrate left-hand side of (4.97) and use the boundary conditions on c from (4.93) to obtain $c_0 = 1$. The numerical solutions of the PDE system from (4.12)–(4.17) indicate that n is near-spatially-uniform when L_{∞} is small. In view of this, we assume that $\eta > 1$, so that (4.95) provides $\Gamma(n_0, 1) = 0$ to leading order, thereby determining n_0 to be spatially-uniform:

$$n_0 = 1 - r_a(\sigma - 1)/r_m. (4.98)$$

To find an expression for v_0 , we first note that the third term from (4.96) is negligible in comparison to the remaining two, and a dominant balance in (4.96) is hence is obtained when $\eta = 1$; however, this contradicts the prior assumption that $\eta > 1$.

To address this contradiction, we define ϵ as a function of the model parameters by using that for spatially-uniform n, (4.19) suggests that $\Gamma(n, 1) = n\Sigma(n)$ as $t \to \infty$. In view of this, and given that $n = n_0 + \mathcal{O}(\varepsilon^2)$ where n_0 satisfies $\Gamma(n_0, 1) = 0$, we must also have $n_0\Sigma(n_0) = 0$ so that $n_0 = \phi$ to leading order and hence $n_0 = \phi + \mathcal{O}(\epsilon^2)$. As such, we set $\epsilon^2 = n_0 - \phi$ so that (4.91) now provides

$$\epsilon^{\eta} \frac{\partial}{\partial X} \left(n_0 \frac{\partial v_0}{\partial X} \right) - \ell \epsilon^3 \frac{\partial}{\partial X} \left[n_0 \frac{1 + \epsilon^{\alpha - 2} n_1}{1 - n_0} \right] - \epsilon^{2 + \eta} \ell^2 \kappa \frac{n_0 v_0}{1 - n_0} = 0. \tag{4.99}$$

Choosing $\alpha = 2$ and then $\eta = 3$, a dominant balance is obtained between the first two terms of (4.99). Integrating this balance and using the first boundary condition from (4.93), we obtain

$$\frac{\partial v_0}{\partial X} = \ell \frac{1 + n_1}{1 - n_0}.\tag{4.100}$$

We now find expressions for $n_1(X)$, $c_1(X)$, $v_1(X)$ and ℓ . Recalling that $\eta = 3$

and $\alpha = 2$, $n_1(X)$ and $c_1(X)$ satisfy the equations

$$\epsilon^3 \frac{\partial v_0}{\partial X} = \epsilon \frac{\ell}{n_0} \Big[\epsilon^2 n_1 A(n_0, 1) + \epsilon^\gamma c_1 B(n_0, 1) \Big], \tag{4.101}$$

$$\epsilon^{\gamma} \frac{\partial^2 c_1}{\partial X^2} = \epsilon^2 \ell^2 \rho n_0, \tag{4.102}$$

where $A(n, c) = \frac{\partial \Gamma}{\partial n}$ and $B(n, c) = \frac{\partial \Gamma}{\partial c}$. Choosing $\gamma = 2$ and using the boundary conditions $\frac{\mathrm{d}c_1}{\mathrm{d}X}\Big|_{X=0} = 0$ and $c_1(0) = 0$, (4.102) provides

$$c_1(X) = \frac{\ell^2 \rho n_0}{2} (X^2 - 1). \tag{4.103}$$

With $\gamma = 2$, all of the terms in (4.101) balance, and summing this balance with (4.100) provides

$$\frac{n_0(1+n_1)}{1-n_0} = n_1 A(n_0, 1) + c_1 B(n_0, 1), \tag{4.104}$$

so that

$$n_1(X) = \frac{2n_0 - (1 - n_0)B\ell^2 \rho n_0(X^2 - 1)}{2(1 - n_0)A - 2n_0}.$$
(4.105)

To find v_0 , we integrate the sum of (4.105) and (4.100), and use the boundary condition $v_0(0) = 0$ to obtain

$$v_0(X) = \frac{\ell}{1 - n_0} \left(1 + \frac{n_0}{(1 - n_0)A - n_0} + \ell^2 \Psi \right) X - \frac{\ell^3 \Psi}{3(1 - n_0)} X^3, \tag{4.106}$$

where

$$\Psi = \frac{(1 - n_0)B\rho n_0}{2(1 - n_0)A - 2n_0}. (4.107)$$

Finally, imposing the boundary condition $v_0(1) = 0$ on (4.106), we obtain

$$\ell = \sqrt{\frac{3}{2\Psi} \left(\frac{n_0}{(n_0 - 1)A + n_0} - 1 \right)}.$$
 (4.108)

In this subsection, we have determined asymptotic solutions of the steady-state ODE system from (4.90)–(4.93) as $L_{\infty} \to 0$, via the perturbations from (4.94) where $(\alpha, \eta, \gamma) = (2, 3, 2)$. The small parameter $\epsilon \to 0^+$ introduced in (4.94) is determined as $\epsilon^2 = n_0 - \phi$, so that $L_{\infty} \to 0$ as $n_0 - \phi \to 0^+$. As discussed above, we expect the bifurcation point between steady-state and extinction-type solutions to be at

 $L_{\infty}=0$, i.e. when $n_0=\phi$. We also expect the PDE system from (4.12)–(4.17) to admit extinction-type solutions such that $L\to 0$ when $n_0-\phi<0$.

4.5.2 Results

In this subsection, we present and discuss the criteria for extinction-type solutions obtained by analysing the system of steady-state ODEs from (4.90)–(4.93) in the limit $L_{\infty} \to 0$. Before this, we illustrate the accuracy of the asymptotic expansion from (4.94) by comparing it with numerical solutions of the PDE system from (4.12)–(4.17).

In figure 4.10(a), we compare the quantity $L_{\infty}(\epsilon)$ obtained by numerically solving the PDE system from (4.12)–(4.17) against the quantity $\epsilon \ell$, where ℓ is stated in (4.108). The quantity L_{∞} is obtained from the PDE system (4.12)–(4.17) by evaluating L(t) for a sufficiently large value of t. Overall, we observe that asymptotic expansion for L_{∞} converges to the numerical solutions as ϵ decreases toward zero. In figure 4.10(a–c), we compare numerical solutions for n, v_n and c obtained from the PDE system (4.12)–(4.17) against the first three perturbations from (4.94) for $\epsilon = 0.1$, from which we observe a very good agreement.

In figure 4.11(a), the solid black line represents the bifurcation curve $L_{\infty}=0$, i.e. $(n_0=\phi)$, obtained in subsection 4.5.1. We indicate parameter regions in which extinction-type solutions or non-extinction type solutions (i.e. travelling-wave or steady-state) are expected. We also indicate three parameter regimes in the extinction region close to the bifurcation curve $L_{\infty}=0$ with coloured dots. To illustrate the accuracy of the extinction region shown in figure 4.11(a), we present $\log(L)$ obtained numerically from the PDE system (4.12)–(4.17), corresponding to the green, orange and pink dot parameter regimes in figure 4.11(b) with their respectively coloured lines. As expected, figure 4.11(b) indicates extinction-type solutions such that $L \to 0$ as $t \to \infty$ for all three parameter regimes. Hence, the results presented in figure 4.11(b) are consistent with the regions presented in figure 4.11(a)

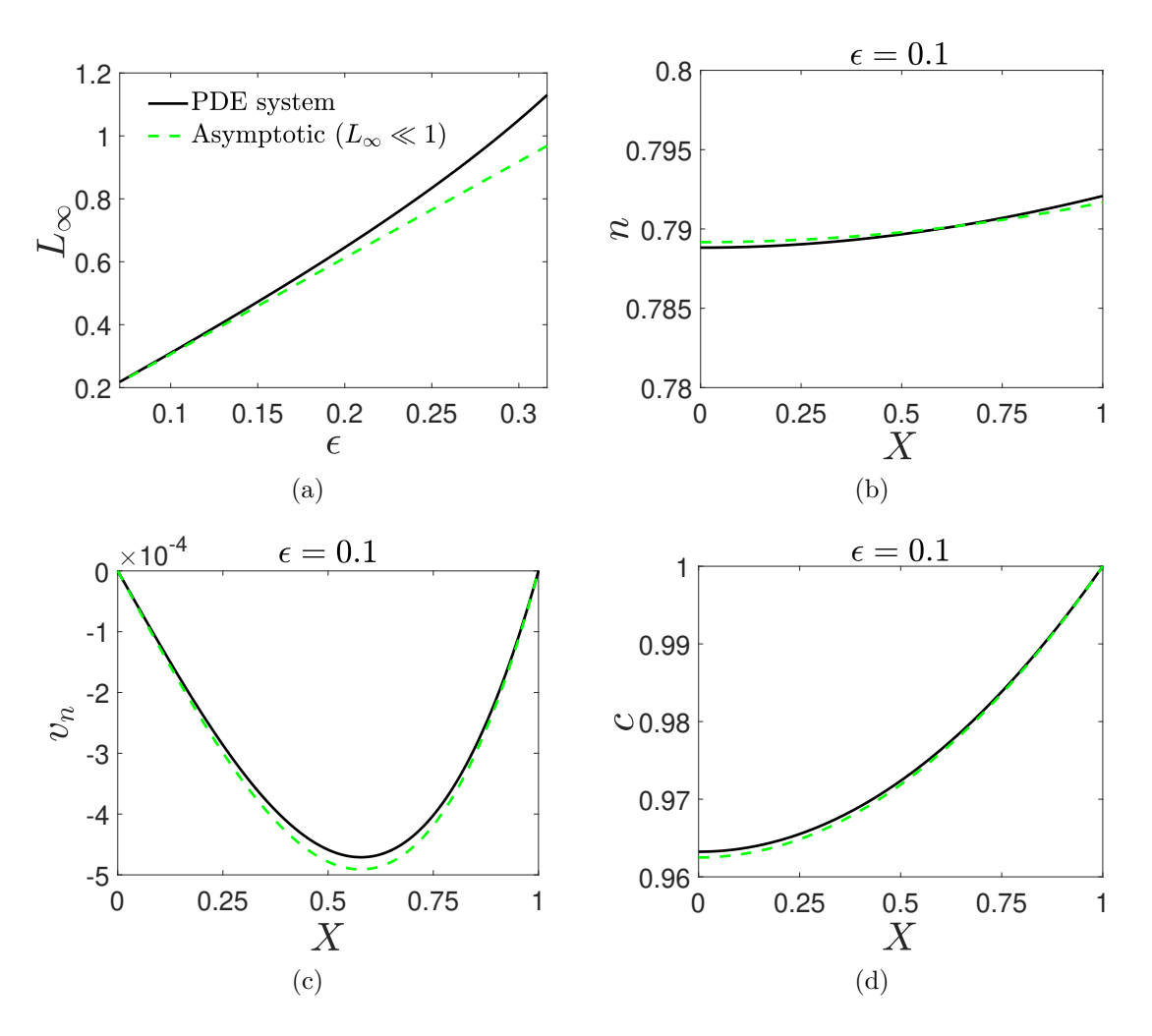


Figure 4.10: Numerical solution of the PDE system from (4.12)–(4.17) and asymptotic solutions from (4.94) for (a) $L_{\infty}(\epsilon)$ where $\epsilon \in [0.07, 0.32]$ and for (b) n(X), (c) $v_n(X)$ and (d) c(X) where $\epsilon = 0.1$. Parameter values: $r_m = 1$, $r_a = 0.8$, $\sigma = 2$, $\rho = 1$, (a) $\phi = [0.7, 0.7950]$ and (c–d) $\phi = 0.79$.

and illustrate a good level of accuracy of the bifurcation curve, $L_{\infty} = 0$.

As seen from the bifurcation curve $L_{\infty}=0$ in figure 4.11(a), the value of ϕ required to generate an extinction-type solution decreases with r_m . This suggests that tumour extinction will occur if there is insufficient cell growth to generate repulsive forces inducing tumour expansion. Interestingly, the extinction criteria $n_0 < \phi$ is also independent of ρ and κ , suggesting that the value of the nutrient diffusivity or cell-liquid drag does not determine when extinction-type solutions will be observed. However, numerical solutions of the PDE system (4.12)–(4.17) indicate that $L_{\infty} = \mathcal{O}(\rho^{-1/2})$ for $\rho \gg 1$, suggesting the size of the tumour can be made arbitrarily small by decreasing the value of the nutrient diffusivity.

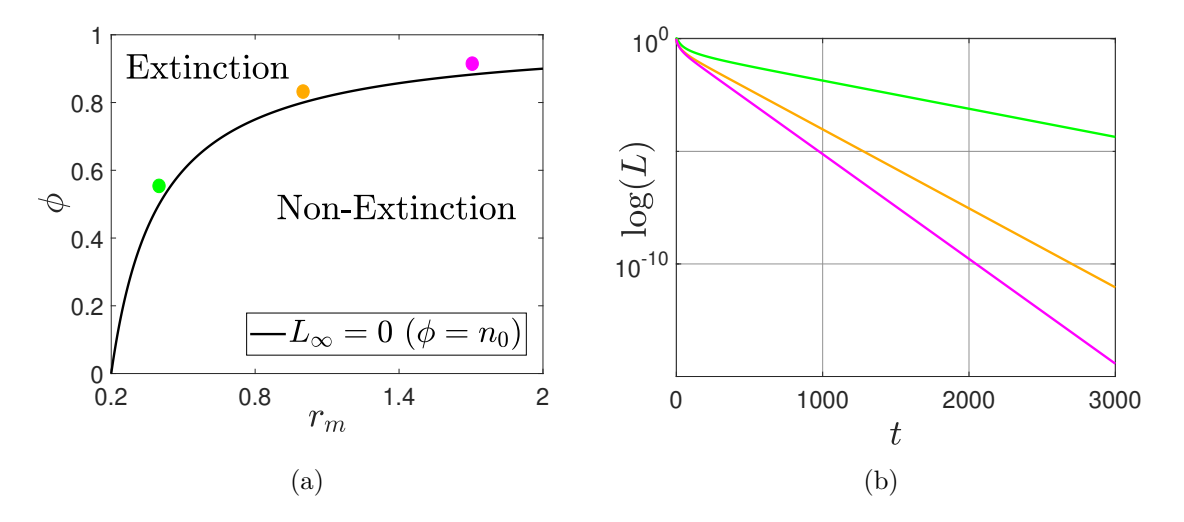


Figure 4.11: In (a), the black solid line is the curve $L_{\infty} = 0$ corresponding to the relationship $\phi = n_0$ where $n_0 = 1 - r_a(\sigma - 1)/r_m$. The green, orange and pink dots in (a) correspond to the coordinates $(r_m, \phi) = (0.4, 0.51)$, $(r_m, \phi) = (1, 0.81)$ and $(r_m, \phi) = (1.7, 0.89)$, respectively. In (b), the green, orange and pink lines represent $\log(L)$ obtained from the PDE system from (4.12)–(4.17), with parameter values corresponding to the respective coloured dots in (a). Parameter values: $r_a = 0.2$, $\sigma = 2$, $\rho = 1$ and $\kappa = 1$.

4.6 Conclusions

In this chapter, the multiphase, moving boundary model of avascular tumour growth developed in Byrne et al. (2002) is analysed. This model consists of three coupled, partial differential equations governing a cell volume fraction n(x, t), its associated velocity and a concentration of nutrient, as well as a moving boundary condition for the tumour edge. The nutrient is abundantly distributed at the tumour edge, and is transported throughout the tumour via diffusion where it is consumed by cells. Mechanisms representing forces generated by cell-cell interactions, cell-liquid drag and cell necrosis are accounted for by considering relevant constitutive assumptions in a similar fashion to those in Byrne et al. (2002) and Breward et al. (2002). One important parameter related to cell-cell interactions is ϕ , which represents the cells' natural packing density. If $n > \phi$, then cells repel each other to relieve membrane stress, and if $n < \phi$, then cells will attract one another due to their filopodia coming into contact.

Solutions of the tumour growth model can develop into a forward-moving travelling wave which corresponds to tumour growth. These solutions have $n > \phi$ in a

vicinity of the wave-front, the cells there experiencing repulsive forces which drive tumour expansion. This expansion, alongside the consumption of nutrient by cells in the proliferating tumour edge, deprives nutrient from the tumour interior resulting in a necrotic core, which is in agreement with both theoretical (Greenspan, 1972; Ward and King, 1997) and experimental studies (Klowss et al., 2022). To accurately characterise these travelling-wave solutions in terms of the model parameters, we analyse the corresponding system of travelling-wave ODEs.

A numerical and asymptotic analysis of the travelling-wave ODEs show that varying the nutrient diffusivity, D, has a significant affect on the structure and growth rate of the tumor. When the diffusivity is large $(D \gg 1)$, the cell volume fraction gradually decreases away from a proliferating rim of $\mathcal{O}(1)$ width on the long-length scale $\mathcal{O}(D^{\frac{1}{2}})$, the tumour interior therefore providing a substantial contribution to the total cell yield. In contrast, when the diffusivity is negligible $(D \ll 1)$, the proliferating rim is of $\mathcal{O}(D^{\frac{1}{2}})$ width, immediately behind which the cell volume fraction is exponentially small. This emphasises the crucial role of a highly diffusible nutrient in the development of viable in vitro tumour spheroids, and suggests that a population of in vivo tumour cells can be reduced by limiting the diffusion of nutrient provided by the surrounding vasculature.

This being said, we note that the diffusivity of key nutrients involved in tumour growth such as oxygen and glucose are not readily controllable in vitro. Our analysis does, however, suggest that the strength of the drag between the cells and liquid has a similar effect on tumor structure as diffusivity, which could be varied by modifying the mechanical characteristics of the extra-cellular liquid. Specifically, via a scaling analysis of the travelling-wave ODEs, we demonstrate that varying the value of the cell-liquid drag can counteract the effects of high or low nutrient diffusivity on the tumour structure. For example, when nutrient diffusivity is low $(D \ll 1)$ but the value of the cell-liquid drag is $\mathcal{O}(D^{-1})$, the width of the proliferating rim is $\mathcal{O}(1)$ instead of $\mathcal{O}(D^{\frac{1}{2}})$.

123

As well as travelling-wave solutions which represent tumour growth, we also observe solutions where the tumour boundary decays exponentially toward zero, which corresponds to tumour extinction. After a period of transient behaviour, these solutions have $n < \phi$ everywhere, so that cells are in a constant state of attraction and results in the contraction and eventual extinction of the tumour. Via a bifurcation analysis of the tumour growth model, we obtain criteria for the extinction of the tumour, which depends on parameters related to cell growth/death and the natural cell density ϕ , but interestingly not on the value of nutrient diffusivity. We do, however, note that controlling cell growth/death rates and the natural packing density of a particular cell line is not readily achievable, particularly *in vivo*. Nonetheless, the novel bifurcation analysis presented in this chapter serves as a foundation for establishing extinction criteria for extensions of the tumour model of Byrne et al. (2002). For instance, this tumour model could be extended to incorporate a chemotherapeutic drug concentration, for which the bifurcation analysis in this chapter could be applied to determine the concentration required for tumour extinction.

A possible extension of the work presented in this chapter is to investigate the effects of chemotaxis on a growing tumour. For example, in Green et al. (2018), a mechanism is employed in the constitutive assumptions representing forces generated by cells responding to a concentration of chemotattractant. Another natural extension of this work is to examine the effect of additional phases on a growing tumour. For example, Breward et al. (2003) extends the model of Byrne et al. (2002) by considering a phase representing blood vessels.

Chapter 5

Conclusions and Future Work

5.1 Thesis Overview

In this thesis, we have developed and analysed two multiphase, moving boundary models representing the evolution of biological tissue. The first model considers a description of engineered tissue growth, whereas the second describes tumour growth. Throughout this work, these models are used to characterise the effects of cell growth and tissue mechanics on various tissue structures. We also believe the mathematical results obtained in their analysis can be applied to a wider class of continuum mathematical models. In addition, the analysis contained herein serves as a foundation for future mathematical investigations.

After providing an overview of engineered tissue and tumour growth, we introduce various mathematical models which have been used to investigate these processes in chapter 1. We then outline a derivation of the conservation of mass equations governing two-phase flow, which are employed throughout this thesis.

5.2 Summary of Results

5.2.1 Chapter 2

In chapter 2, we developed and analysed a multiphase, moving boundary model representing the development of tissue in vitro in an artificial scaffold. Following many multiphase studies of engineered tissue growth (Lemon and King, 2007a; O'Dea et al., 2010; Lemon et al., 2006), we restrict our attention to a cell phase, extra-cellular liquid phase and a scaffold phase, the former two being modelled as incompressible fluids and the latter as an inert solid. Assuming that the interphase drags associated with the fluid phases are dominated by those with the scaffold, we relate the velocity of the fluid phases to their respective pressures via Darcy's laws. In contrast to the above studies which employ equations of momentum balance, one novelty of this work arises via the use of Darcy's law, which allows the elimination of the cell velocity from the governing equations. The reduced model comprises a nonlinear reaction-diffusion equation for the cell phase, coupled to a moving boundary condition for the tissue edge. Our formulation also differs from the existing literature that employ Darcy's law to model tissue growth (Eyles et al., 2019; King and Franks, 2004; Franks and King, 2003), which treat the velocity field of a two-fluid flow as a single continuum.

A non-dimensionalisation of the reduced model considered in chapter 2 exposes an important dimensionless grouping, κ , that describes the difference between the scaffold porosity and the ratio between the cell death and growth rates. For $\kappa > 0$, we show that the cell volume fraction spreads through the scaffold as a semi-infinite travelling wave with constant speed, which corresponds to successful growth. We compute the speed at which the tissue edge moves through the scaffold via a travelling-wave analysis, and thereby determine optimal values of parameters related to tissue mechanics and growth which optimise this wave speed. For example, we demonstrate that wave speed is greatest when the viscosity of the cells is much greater than the viscosity of the liquid, and when the scaffold porosity is large.

For $|\kappa| \ll 1$, we employ an asymptotic analysis to find explicit solutions for the cell volume fraction and moving boundary from the time-dependent model. In this case, the model reduces to a Porous-Fisher-Stefan system (Fadai and Simpson, 2020; Fisher, 1937; Aaronson, 1980) with logistic growth. Alongside the various biological implications obtained from these explicit solutions valid when $|\kappa| \ll 1$, the analysis itself provides a novel mathematical contribution. Specifically, we extend the work of Newman (1980) who constructed an implicit solution for the time-dependent Porous-Fisher Equation, by obtaining the corresponding explicit large-time solutions for both a positive and negative reaction term.

Although the reaction-diffusion model developed in chapter 2 represents a tractable description of tissue growth, it is ill-posed due to negative diffusion in parameter regimes where attractive forces arising from cell-cell and cell-scaffold interactions dominate repulsive forces. As such, our model can not admit solutions representing the formation of separate cell aggregates arising from cellular attractive forces, like those presented in existing multiphase models of engineered tissue growth such as Green et al. (2018), Lemon et al. (2006) and Lemon and King (2007a). A further limitation of our model is that non-negligible forces generated by cellular viscosity in a highly porous medium are not captured by Darcy's law. To overcome these limitations, it is appropriate to consider equations of momentum balance (which account for stresses arising from cellular viscosity) in place of Darcy's law, such as in Lemon et al. (2006) and O'Dea et al. (2010). This modification is addressed and examined in chapters 3 and 4.

5.2.2 Chapter 3

The remainder of this thesis focuses on the multiphase, moving boundary of tumour growth developed in Byrne et al. (2002), which considers the evolution of a motile, viscous a cell phase and an inviscid liquid phase. Although this model describes tumour growth, the results obtained in its analysis can be applied to a wider class

of multiphase tissue growth models. The velocity of the cell and liquid phases are related to their respective pressures via momentum balance equations, which leads to a more complex model than the reaction-diffusion system considered in chapter 2. Furthermore, in contrast to the model developed in chapter 2, the model of Byrne et al. (2002) is well-posed in parameter regimes where attractive forces arising from cell-cell interactions dominate repulsive forces.

In chapter 3, we analyse spatially-patterned and travelling-wave solutions of the tumour growth model developed in Byrne et al. (2002). Following King and Franks (2004), we assume that nutrient is abundantly distributed throughout the tumour. Whilst this assumption omits important elements such as cell death induced via nutrient limitation, it is physically relevant in the context of an *in vivo* tumour in the initial stage of development where all cells are adequately nourished. Additionally, this nutrient rich assumption is appropriate when considering the initial growth of a suspension of *in vitro* tumour cells (Byrne et al., 2002) or a monolayer cell culture.

The primary focus of the analysis in chapter 3 pertains to patterned solutions, which are associated with multiple regions of high cell density separated by regions of low cell density. As described in Green et al. (2009a), these patterned solutions can be associated with the structural instability of an *in vitro* suspension of cells, which could lead to their break-up and consequently the formation of separate spheroids. The formation of these patterned solutions can also associated with the formation of high density cell aggregates in a monolayer culture, as seen in the experimental studies of da Silva et al. (2018).

In contrast to existing studies of multiphase, moving boundary models of tissue growth (Byrne et al., 2002; Lemon and King, 2007a,b), this work adopts a unique approach to obtain regions of parameter space in which patterned solutions are observed. Specifically, these regions are determined by computing the instability of travelling-wave solutions of the tumour growth model, which incorporates the effects of the moving boundary and attendant boundary conditions. Whilst the regions dis-

played an excellent degree of accuracy when compared to the full time-dependent model, they were computationally expensive to compute. To overcome this limitation, we determined the stability of a spatially-uniform steady state. In contrast to the travelling-wave stability analysis, this steady state does not satisfy the moving boundary condition at the tumour edge; however, it provides an analytical dispersion relation in terms of the model parameters. Interestingly, the regions of instability obtained via the travelling-wave and spatially-uniform stability analyses are in very good agreement, which allows us to exploit the simpler dispersion relation approach to deduce how varying model parameters affects the onset of pattern formation. For example, using this dispersion relation, we demonstrate that patterned solutions will not form if there is no cell death, and obtained a maximum value for the rate of cell proliferation such that patterned solutions will form. Furthermore, the good agreement between the two stability analyses suggests the inclusion or exclusion of the moving boundary does not determine when patterned solutions will form, thereby allowing us to identify the dominant destabilising mechanism giving rise to pattern formation.

5.2.3 Chapter 4

In chapter 4, we revisit the model of Byrne et al. (2002), although we now assume the presence of a single diffusive concentration of nutrient within the tumour, which is abundantly distributed at the tumour edge. In certain parameter regimes, the model exhibits forward-moving travelling waves, which corresponds to tumour growth. This expansion, along-side the consumption of nutrient by cells at the tumour edge, deprives nutrient from the tumour interior resulting in a necrotic core, which is in agreement with both theoretical (Greenspan, 1972; Ward and King, 1997) and experimental studies (Klowss et al., 2022).

Although the seminal model of Byrne et al. (2002) has been employed and extended in many studies of tumour growth (Breward et al., 2003; Remesan et al.,

2023), the corresponding travelling-wave ODEs have not been analysed. In view of this, we extend the work of Breward et al. (2002) by developing a numerical algorithm to solve these ODEs using techniques described in Ward and King (1999), which allow us to obtain important quantities relating to tumour growth in terms of the model parameters. Another new aspect of this work arises by obtaining asymptotic solutions of these travelling-wave ODEs in terms of a compound parameter related to nutrient diffusivity and the value of the cell-liquid drag. Interestingly, we found that the effects of high or low nutrient diffusivity on the tumour structure can be counteracted by varying the value of the cell-liquid drag.

As well as travelling-wave solutions, the tumour model of Byrne et al. (2002) can exhibit solutions corresponding to tumour extinction, whereby the tumour edge decays exponentially toward zero. It is surprising that, despite representing a significant biological phenomena, the extinction-type solutions admitted by this model have not yet been investigated. As such, we obtain criteria for tumour extinction via a bifurcation analysis, and determine that if the natural packing density of cells is larger than the net rate of cell growth, the tumour cells will be in a constant state of attraction resulting in tumour contraction and hence extinction. Whilst parameters related to packing density and growth/death rates of a particular cell line may not be readily controllable, this bifurcation analysis serves as a foundation for establishing extinction criteria for extensions of the two-phase tumour model.

5.2.4 Future Work

Some natural extensions to the individual models described in each chapter are provided, and we now briefly outline some overarching extensions that can apply to all of these models.

Throughout this thesis, we follow Byrne et al. (2002), Lemon and King (2007a) and Lemon et al. (2006) and assume a one-dimensional Cartesian geometry. While this choice allows for the application of various mathematical techniques, such as

travelling-wave and asymptotic analysis, we acknowledge that this geometry is idealised and does not fully represent the intricacies of tissue growth. As such, a possible avenue for future exploration could involve investigating the models developed in this thesis on more realistic geometries. For example, in chapter 5, the model could be extended to a spherical geometry to better capture the growth dynamics of a tumour spheroid. However, it is important to note that modelling on higher dimensions than one may entail significant numerical computations.

Following Lemon and King (2007b) and Klowss et al. (2022), an additional extension to explore could involve incorporating statistical theory to compare the numerical and analytical results obtained in this thesis with experimental data. This comparative analysis could provide valuable insights and predictions related to determining suitable values for model parameters.

Bibliography

- D. G. Aaronson. Density-Dependent Interaction-Diffusion Systems. Dynamics and Modelling of Reactive Systems, Academic Press, 1980. 161–176.
- G. Beaune, Nada Khalifat T. V. Stirbat, O. Cochet-Escartin, S Garcia, V. V. Gurchenkov, M. P. Murrell, S. Dufour, D. Cuvelier, and F. Brochard-Wyart. *How cells flow in the spreading of cellular aggregates*. PNAS, 2014. 111(22):8055-8060.
- A. Boonderick, W. Triampo, and N. Nuttavut. A Review of Cellular Automata Models of Tumor Growth. International Mathematics forum, 2010. 61:3023-3029.
- C. J. W. Breward, H. M. Byrne, and C. E. Lewis. *The role of cell-cell interactions in a two-phase model for avascular tumour growth*. Journal of Mathematical Biology, 2002. 45:125-152.
- C. J. W. Breward, H. M. Byrne, and C. E. Lewis. A multiphase model describing vascular tumour growth. Bulletin of Mathematical Biology, 2003. 65(4):609-640.
- A. C. Burton. Rate of growth of solid tumours as a problem of diffusion. Growth, 1966. 30(2):157-76.
- H. M. Byrne, J.R. King, D.L.S McElwain, and L. Preziosi. *Two-Phase Model of Solid Tumour Growth*. Applied Mathematics Letters, 2002. 16:567-573.
- B. P. Chan and K. W. Leong. Scaffolding in tissue engineering: general approaches and tissue-specific considerations. European Spine Journal, 2008a. 17(4): 467–479.
- B. P. Chan and K. W. Leong. Scaffolding in tissue engineering: general approaches and tissue-specific considerations. European Spine Journal, 2008b. 17(4):467–479.
- C.A. Chung, T. Lin, S. Chen, and H. Huang. Hybrid cellular automaton modeling of nutrient modulated cell growth in tissue engineering constructs. Journal of Theoretical Biology, 2010. 262:267–278.
- P. A. Clarkson, A. S. Fokas, and M. J. Ablowitz. *Hodograph Transformations of Linearizable Partial Differential Equations*. SIAM Journal on Applied Mathematics, 1989. 49(4):1188–1209.
- P.C.A. da Silva, A.A. Santos, S.G. Alves, and M.L. Martins. *Cell aggregation in monolayer culture: Clues to a universal kinetics*. Physica A: Statistical Mechanics and its Applications, 2018. 510:725-740.

L.G. de Pillis, W. Gu, and A.E. Radunskaya. *Mixed Immunotherapy and Chemotherapy of Tumors: Modeling, Applications and Biological Interpretations*. Journal of Theoretical Biology, 2006. 238:841–862.

- D. E. Discher, P. Janmey, and Y.L. Wang. Tissue cells feel and respond to the stiffness of their substrate. Science, 2005. 310:1139–1143.
- D. Drew and S. Passman. *Theory of Multicomponents Fluids*. Applied Mathematical Sciences, Springer, 1998. Volume 135.
- D. A. Drew. *Mathematical modelling of two-phase flow*. Annual Review of Fluid Mechanics, 1983. 15:261–291.
- K. Dzobo, N. E. Thomford, D. A. Senthebane, H. Shipanga, A. Rowe, C. Dandara, M. Pillay, and K. S. C. M. Motaung. Advances in Regenerative Medicine and Tissue Engineering: Innovation and Transformation of Medicine. Stem Cells International, 2018. Article ID 2495848.
- R. Edmondson, J.J Broglie, A. F. Adcock, and L. Yang. Three-Dimensional Cell Culture Systems and Their Applications in Drug Discovery and Cell-Based Biosensors. Assay Drug Development Technology, 2014. 12(4): 207–218.
- G. B. Ermentrout and L. Edelstein-Keshet. *Cellular Automata Approaches to Biological Modeling*. Journal of Theoretical Biology, 1993. 160:97-133.
- J. Eyles, J. R. King, and V. Styles. A tractable mathematical model for tissue growth. Interfaces and Free Boundaries, 2019. 21(4): 463-493.
- N. T. Fadai. Semi-infinite travelling waves arising in a general reaction-diffusion Stefan model. Nonlinearity, 2021. 34:725-743.
- N. T. Fadai and M. J. Simpson. New travelling wave solutions of the Porous-Fisher model with a moving boundary. Journal of Physics A: Mathematical and Theoretical, 2020. 53(9).
- N. P. Fam, S. Verma, M. Kutryk, and D. J. Stewart. *Clinician guide to angiogenisis*. Circulation, 2003. 108:2613–2618.
- R. A. Fisher. The wave of advantageous genes. The Annals of Eugenics, 1937. 7:355–369.
- Adam Fletcher. World's first tissue engineered whole organ transplant is a success. BioNews, 2008. 485.
- J. Folkman. What is the evidence that tumors are angiogenesis dependent? J Natl Cancer Inst., 1990. 82(1):4–7.
- S. J. Franks and J. R. King. Interactions between a uniformly proliferating tumour and its surroundings: uniform material properties. Mathematical Medicine and Biology, 2003. 20: 47–89.
- Y. Shafrir M. A. Steinberg G. Forgacs G, R. A. Foty. Viscoelastic properties of living embryonic tissues: a quantitative study. BioPhys. J, 1998. 74:2227–34.

R. A. Gattenby and E. T. Gawlinski. A Reaction-Diffusion Model of Cancer Invasion. Cancer Res., 1996. 56:5745-5753.

- E. Green, S. Waters, K. M. Shakesheff, and H. M. Byrne. *A Mathematical Model of Liver Cell Aggregation In Vitro*. Bulletin of Mathematical Biology, 2009a. 71(4):906-930.
- J. E. F. Green, S. L. Waters, K. M. Shakesheff, and H. M. Byrne. A Mathematical Model of Liver Cell Aggregation In Vitro. Bulletin of Mathematical Biology, 2009b. 71:906–930.
- J. E. F. Green, J. P. Whiteley, J. M. Oliver, H. M. Byrne, and S. L. Waters. *Pattern formation in multiphase models of chemotactic cell aggregation*. Journal of Mathematical Biology, 2018. 35(3):319-346.
- H. P. Greenspan. *Models for the Growth of a Solid Tumor by Diffusion*. Studies in Applied Mathematics, 1972. 52:317–340.
- A. V. Hill. *The diffusion of oxygen and lactic acid through tissues*. Proceedings of the Royal Society B, 1928. 104:39–96.
- Y. Ikada. *Challenges in tissue engineering*. Journal of the Royal Society Interface, 2006. 3:589–601.
- G. Jensen, C. Morrill, and Y. Huang. 3D tissue engineering, an emerging technique for pharmaceutical research. Acta Pharmaceutica Sinica B, 2018a. 8(5): 756-766.
- G. Jensen, C. Morrill, and Y. Huang. 3D tissue engineering, an emerging technique for pharmaceutical research. Acta Pharmaceutica Sinica B, 2018b. 8(5): 756-766.
- M.E Katt, A.L Placone, A.D Wong, Z.S Xu, and P.C Searson. In Vitro Tumor Models: Advantages, Disadvantages, Variables, and Selecting the Right Platform. Front Bioeng Biotechnology, 2016. 12:4-12.
- J. R. King and S. J. Franks. *Mathematical analysis of some multi-dimensional tissue-growth models*. European Journal of Applied Mathematics, 2004. 15: 273–295.
- J. J. Klowss, A. P. Browning, R. J. Murphy, E. J. Carr, M. J. Plank, G. Gunasingh, N. K. Haass, and M. J. Simpson. A stochastic mathematical model of 4D tumour spheroids with real-time fluorescent cell cycle labelling. J. R. Soc. Interface, 2022. 19:20210903.
- J. M. Lackie. Cell Movement and Cell Behavior. Allen and Unwin, 1986.
- D. Lehotzky and G. K. H. Zupanc. Cellular Automata Modeling of Stem-Cell-Driven Development of Tissue in the Nervous System. Developmental Neurobiology, 2019. 79(5):497-517.
- G. Lemon and J. King. Travelling-wave behaviour in a multiphase model of a population of cells in an artificial scaffold. Journal of Mathematical Biology, 2007a. 24(1):57-83.

G. Lemon and J. R. King. Multiphase modelling of cell behaviour on artificial scaffolds: effects of nutrient depletion and spatially nonuniform porosity. Journal of Mathematical Medicine and Biology, 2007b. 24:5783.

- G. Lemon, J. R. King, H. M. Byrne, O. E. Jensen, and K. M. Shakesheff. *Mathematical modelling of engineered tissue growth using a multiphase porous flow mixture theory*. Journal of Mathematical Biology, 2006. 52:571-594.
- G. Lemon, D. Howard, M. J. Tomlinson, L. D. Buttery, F. R.A.J. Rose, S. L. Waters, and J. R. King. *Mathematical modelling of tissue-engineered angiogenesis*. Journal of Biological Systems, 2009. 221:101–120.
- M. Levitt. Could the organ shortage ever be met? Life Sciences, Society and Policy, 2015. 11: 6.
- O. A. Lozoya and S. R. Lubkin. Mechanical control of spheroid growth: Distinct morphogenetic regimes. J. BioMechs, 2012. 45(2):319–325.
- P. X. Ma. Scaffolds for tissue fabrication. Materials Today, 2004. 7(5):30-40.
- C. K. Macnamara. Biomechanical modelling of cancer: Agent-based force-based models of solid tumours within the context of the tumour microenvironment. Computational and Systems Oncology, 2021. DOI: https://doi.org/10.1002/cso2.1018.
- J. Malda, T. B. F. Woodfield, F. V. D. Vloodt, F. K. Kooy, D. E Martens, J. Tramper, C. A V. Blitterswijk, and J. Rielse. *The effect of PEGT/PBT scaffold architecture on oxygen gradients in tissue engineered cartilaginous constructs*. Biomaterials, 2004. 25(26):5681-5796.
- S. D. McCullen, A. G. Y. Chow, and M. M. Stevens. *In vivo tissue engineering of musculoskeletal tissues*. Current Opinion in Biotechnology, 2011. 22(5): 715-720.
- B. McDaniel, T. Badri, and R. B. Steele. *Basal Cell Carcinoma*. National Library of Medicine, 2020. DOI:https://www.ncbi.nlm.nih.gov/books/NBK482439/.
- D. L. S McElwain and G. J. Pettet. *Cell migration in multicell spheroids: Swimming against the tide*. Bulletin of Mathematical Biology, 1993. 55:655–674.
- R. B. Mokhtari, T.S Homayouni, N. Baluch, E. Morgatskaya, S. Kumar, B. Das, and H. Yeger. *Combination therapy in combating cancer*. Oncotarget, 2017. 8(23):38022-38043.
- A. Monazzam, P. Razifar, Ö. Lindhe, R. Josephsson, B. Långström, and M Bergström. A new, fast and semi-automated size determination method (SASDM) for studying multicellular tumor spheroids. Cancer Cell International, 2005. 5:32.
- C. M. Murphy, M. G. Haugh, and F. J. O'Brien. The effect of mean pore size on cell attachment, proliferation and migration in collagen-glycosaminoglycan scaffolds for bone tissue engineering. Biomaterials, 2010. 31(3):461-466.
- H. Murphy, H. Jaafari, and H. M. Dobrovolny. Differences in predictions of ODE models of tumor growth: a cautionary example. BMC Cancer, 2016. 26(16):163.

- J. D. Murray. Mathematical Biology I: An Introduction. Springer-Verlag, 2002.
- W. I. Newman. Some Exact Solutions to a Non-linear Diffusion Problem in Population Genetics and Combustion. Journal of Theoretical Biology, 1980. 85:325-334.
- F. J. O'Brien. *Biomaterials scaffolds for tissue engineering*. Materials today, 2011. 14(3):88-95.
- R. D. O'Dea, S. L. Waters, and H. M. Byrne. A multiphase model for tissue construct growth in a perfusion bioreactor. Mathematical Medicine and Biology, 2010. 27:95127.
- C. H. Park and K. M. Woo. Fibrin-Based Biomaterial Applications in Tissue Engineering and Regenerative Medicine. Advanced Experiments in Medical Biology, 2018. 1064:253-261.
- A. Patel. Benign vs Malignant Tumors. JAMA Oncology, 2020. 6(9):1488.
- H. Petite, V. Viateau, W. Bensaïd, A. Meunier, C. de Pollak, M. Bourguignon, K. Oudina, L. Sedel, and G. Guillemin. *Tissue-engineered bone regeneration*. Nature Biotechnology, 2000. 18(9):959-963.
- G. J. Pettet, C. P. Please, M. J. Tindall, and D. L. S McElwain. *The Migration of Cells in Multicell Tumor Spheroids*. Bulletin of Mathematical Biology, 2001. 63:231–257.
- N. Plunkett and F. J. O'Brien. *Bioreactors in tissue engineering*. Technology and Health Care, 2018. 19(1): 55-69.
- F. Pourhasanzade and S. H. Sabzpoushan. A cellular automata model of chemotherapy effects of tumour growth: targeting cancer and immune cells. Mathematical and Computer Modelling of Dynamical Systems, 2019. 25(1):63-89.
- L. Preziosi and A. Tosin. Multiphase modelling of tumour growth and extracellular matrix interaction: mathematical tools and applications. Journal of Mathematical Biology, 2003. 58:625–656.
- M. R. Rad, M. Bohloli, M. A. Rahnama, A. Anbarlou, P. Nazeman, and A. Khojasteh. *Impact of Tissue Harvesting Sites on the Cellular Behaviors of Adipose-Derived Stem Cells: Implication for Bone Tissue Engineering.* Stem Cells International, 2017. ID:2156478.
- G. C. Remesan, J. A. Flegg, and H. M. Byrne. Two-phase model of compressive stress induced on a surrounding hyperelastic medium by an expanding tumour. Journal of Theoretical Biology, 2023. 86:18.
- T. G. Ruksha. *MicroRNAs' control of cancer cell dormancy*. Cell Division, 2019. 14:11.
- R.K Sachs, L. R. Hlatky, and P. Hahnfeldt. Simple ODE Models of Tumor Growth and Anti- Angiogenic or Radiation Treatment. Mathematical and Computer Modelling, 2001. 33:1297-1305.

T. Sato, H. Tao, M. Araki, H. Ueda, K. Omori, and T. Nakamura. Replacement of the Left Main Bronchus With a Tissue-Engineered Prosthesis in a Canine Model. The Annals of Thoracic Surgery, 2008. 86:422-428.

- R. Schimming and R. Schmelzeisen. *Tissue-engineered bone for maxillary sinus augmentation*. Journal of Oral and Maxillofacial surgery, 2010. 62(6):724-729.
- G. Sciumè, S. Shelton, W. G. Gray, C. T Miller, F. Hussain, M. Ferrari, P. Decuzzi, and B. A. Schrefler. *A multiphase model for three-dimensional tumor growth*. New journal of physics, 2013. 15:015005.
- S.C. Shah, V. Kayamba, R.M Peek, and D. Heimburger. Cancer Control in Lowand Middle-Income Countries: Is It Time to Consider Screening? 2019. 5:1-8.
- K. Shield, M.L Ackland, N. Ahmed N, and G.E Rice. Multicellular spheroids in ovarian cancer metastases: biology and pathology. Gynecology Oncology, 2014. 113:143–148.
- E.A Swabb, J. Wei, and P. M. Gullino. *Diffusion and convection in normal and neoplastic tissues*. Cancer Res., 1974. 34:2814–2822.
- H. Teimouri, M.P Kochugaeva, and A.B. Kolomeisky. *Elucidating the correlations between cancer initiation times and lifetime cancer risks*. Science Reports, 2019. 9:18940.
- R. H. Thomlinson and L. H. Gray. The histological structure of some human lung cancers and the possible implications for radiotherapy. British journal of cancer, 1955. 9:539–549.
- K. E. Thompson and H. M. Byrne. *Modelling the internalization of labelled cells in tumour spheroids*. Studies in Applied Mathematics, 1999. 61:601–623.
- A. Tosin and L. Preziosi. Multiphase modeling of tumor growth with matrix remodeling and fibrosis. Mathematical and Computer Modelling, 2010. 52(7):969-976.
- Charles Vacanti. The history of tissue engineering. Journal of Cellular and Molecular Medicine, 2006. 10(3): 569-576.
- C. Vaghi, A. Rodallec, R. Fanciullino, J. Ciccolini, J. P Mochel, M. Mastri, C. Poignard, J. M. J Ebos, and S. Benzekry. Population modeling of tumor growth curves and the reduced Gompertz model improve prediction of the age of experimental tumors. PLoS Computational Biology, 2020. 16(2): e1007178.
- A. Villasante and G. Vunjak-Novakovic. *Tissue-engineered models of human tumors for cancer research*. Expert Opinion on Drug Delivery, 2015. 10(3):257-268.
- A. A. Vitvitsky. Cellular automata with dynamic structure to simulate the growth of biological tissues. Numerical Analysis and Applications, 2014. 7:263–273.
- X. Wang, M. Chen, R. Wei, and Z. Wang. External Radiation versus Internal Radiation for Patients with Advanced Unresectable HCC -A SEER Based Study. J. Cancer, 2019. 10(5): 1171–1180.

J. P. Ward and J. R. King. *Mathematical modelling of avascular tumour growth*. IMA Journal of Mathematics Applied in Medicine Biology, 1997. 14:39-69.

- J. P. Ward and J. R. King. Mathematical modelling of avascular tumour growth II: Modelling growth saturation. IMA Journal of Mathematics Applied in Medicine Biology, 1999. 16:171-211.
- B. B. Youssef. A parallel cellular automata algorithm for the deterministic simulation of 3-D multicellular tissue growth. Cluster Computing, 2015. 18:1561–1579.
- W. Zakrzewski, M. Dobrzyński, M. Szymonowicz, and Z. Rybak. *Stem cells: past, present, and future.* Stem Cell Research Therapy, 2019. 10: 68.
- J. Zhao, M. Griffin, J. Cai, S. Lee, P. E. M. Butler, and D. M. Kalaskar. *Bioreactors for Tissue Engineering: An Update*. Biochemical Engineering Journal, 2016. 109:268-281.